“Università degli Studi di Napoli “Federico II”

Scuola Politecnica e delle Scienze di Base
Area Didattica di Scienze Matematiche Fisiche e Naturali

Dipartimento di Fisica “Ettore Pancini”

Laurea Magistrale in Fisica

In vitro and in silico radiobiological characterization of DNA damage induced by Boron-Neutron Capture Therapy (BNCT)

Relatori:
Prof. Lorenzo Manti
Prof.ssa Silva Bortolussi

Candidata:
Francesca Fede
Matricola N94/757

A.A. 2022/2023

"PER ASPERA AD ASTRA"

CONTENTS

Introduction 6

1. The physical and radiobiological rationale underlying Boron-Neutron Capture Therapy (BNCT) 9

1.1. The $^{10}B(n,\alpha)^{7}Li$ nuclear reaction

1.2. State of the art of BNCT

1.3. DNA Damage Response (DDR) and Ionizing Radiation-Induced Foci (IRIF)

1.3.1. Double-Strand Break (DSB) repair pathways

1.3.2. 53BP1 and γH2AX as biomarkers of DDR-related IRIF: the Foci assay

1.3.3. IRIF dynamics

1.4. Radiation-induced chromosomal aberrations

1.4.1. The multicolour Fluorescence In Situ Hybridization (mFISH) technique as a tool to unveil BNCT-associated complex DNA damage

2. Monte-Carlo simulations in radiobiology 22

2.1. Geant4-DNA

2.2. The Clustering application in Geant4-DNA

3. Materials and methods 29

3.1. Experimental setup

3.1.1. Cell culture maintenance

3.1.2. Boron compound treatment for BNCT irradiations

3.1.3. DNA damage assays

3.2. Irradiations

3.2.1. Neutron irradiation

3.2.2. X-ray irradiation

3.3. Measurement of boron uptake in cells

3.4. Measurement of radiation-induced DNA damage

3.4.1. Foci Assay

3.4.1.1. Image acquisition and processing by the Metafer software

3.4.1.2. The use of MATLAB for foci counting

3.4.2. FISH Assays
3.4.2.1. Image acquisition
3.4.2.2. Karyotyping by the software ISIS
3.5. Simulations using the Clustering application of Geant4-DNA
3.5.1. Geometry
3.5.2. Source characteristics
3.5.3. Clustering algorithm parameters and output files

4. Results and discussion 46
4.1. Optimization of MATLAB foci counting
4.2. Evaluation of DNA repair dynamics in BNCT using the Foci Assay
4.3. Evaluation of DNA damage complexity in BNCT using the FISH techniques
4.4. Results of simulations through the Geant4-DNA Clustering application

Conclusions and future prospectives 65
Appendix 1: Experimental protocols: *68*
1.1 Foci Assay protocol
1.2 mFISH protocol
1.3 Whole Chromosome Painting protocol
1.4 BPA preparation protocol
Appendix 2: Counting code 72
Appendix 3: Table of experimental results 76
Bibliography 81
Ringraziamenti 86

Introduction

Boron-Neutron Capture Therapy (BNCT) is a tumour-selective particle radiotherapy, based on the nuclear reaction known as boron-neutron capture, that is ^{10}B (n, α) ^{7}Li. It was proposed back to 1936, four years after Chadwick discovered neutrons and just after the description of the reaction of thermal neutron capture by the nucleus of the isotope 10-boron (^{10}B). It can be described as a binary treatment, based on the administration of boron carriers incorporated preferentially by tumour cells, followed by irradiation with a thermal or epithermal neutron beam. The clinical potential of BNCT strongly depends on the selective bio-distribution of boron in the tumour; today the most used carrier is the boronophenylalanine (BPA), an amino acid derivative actively incorporated by cancer cells, whose need of nutrients is increased compared to healthy cells. In fact, an ideal boron carrier should be non-toxic at therapeutic dose levels and should accumulate preferentially in tumour cells versus blood and normal tissue in order to obtain a therapeutic advantage minimizing normal-tissue radiotoxicity. The radiobiological rationale of BNCT relies on the fact that the capture reaction between a ^{10}B nucleus and a thermal neutron produces around 1-MeV, hence short range, α-particles and recoiling ^{7}Li nuclei, which have a high Linear Energy Transfer (LET). This means that the charged particles produced in the capture reaction have a higher Relative Biological Effectiveness (RBE) compared to the photons/electrons used in conventional radiotherapy. In fact, the energy deposition pattern of the reaction products will produce more complex DNA damage, which is by definition less repairable than conventional radiotherapy, approximately within the diameter of a single cancer cell (~10μm) unlike hadrontherapy where it is more difficult to conform the dose profile to irregular tumour volumes. Thus, if the surrounding healthy cells have absorbed lower boron concentration, the neutron irradiation will not cause lethal damages to them. Neutron irradiation will produce, nevertheless, a background dose due to: the low-LET gamma rays from the capture of thermal neutrons in hydrogen and from the photons present in the neutron beam; intermediate LET protons originated by the scattering of fast neutrons and by thermal neutron capture in nitrogen. As the background dose affects both normal and tumour tissue, it is of utmost importance that a sufficient tumour-to-normal tissue boron concentration ratio can be obtained to fully exploit the selective therapeutic potential of BNCT.

High-LET ionizing radiation (IR), like the alpha and lithium particles associated with BNCT, challenges the intracellular repair capacity, because it causes locally clustered DNA damage. Such clustered damage, a spatio-temporally co-localized combination of Single-Strand Breaks (SSBs), Double-Strand Breaks (DSBs) and other types of damage such as base/nucleotides lesions, very likely leads to cell death, because the ensuing repair mechanism will be overwhelmed by the damage complexity, and it might not be able to repair all the injuries. This is the radiobiological rationale by which BNCT is potentially more effective in terms of tumour control compared to conventional radiotherapy, where low-LET radiation is used. Furthermore, as BNCT involves biochemical rather than geometrical targeting, it lends itself to treat tumour near sensitive organs, such as inoperable or

radioresistant cancers, if the above-mentioned uptake selectivity requirements of the boron carrier are met.
Currently, BNCT is not a routinely implemented radiotherapy cancer treatment, one reason being that the only available neutron sources, until recently, have been research nuclear reactors. However, clinical studies for glioblastoma multiforme, melanoma, recurrent head and neck tumours, lung and liver metastases have been performed or are underway in Japan, Taiwan, Italy, Finland, USA and Argentina employing mostly nuclear reactors as the neutron source. Indeed, a boost in BNCT-related research and clinical application is occurring nowadays thanks to the development of accelerator-based neutron sources, for example low-energy proton accelerators that generate neutron beams by nuclear reactions in lithium or beryllium targets. This represents a turning point in the BNCT field because it enables in-hospital treatments, paving the way for more widespread clinical trials for different tumours and a larger number of patients.
Despite the long-standing research, very little has been investigated in vitro and in silico on the radiobiological mechanisms underlying cellular response to BNCT other than tumour cell death, such as DNA damage, whose understanding can contribute to identify markers of cellular response to BNCT and may serve to modulate signalling pathways to enhance BNCT therapeutic efficacy and reduce associated toxicity.

Therefore, the aim of this thesis work is to evaluate the DNA damage caused by BNCT by an in vitro experimental study of repair efficiency and damage complexity using epithelial mammary MCF10A cells and by a Monte Carlo simulation-based approach using the application “Clustering” of Geant4DNA, whose output is the number of DSBs, allowing to separate the various contributions of the different components of the BNCT mixed field contributing to the experimentally measured biological damage.

The work described in this thesis was carried out in collaboration with the University of Pavia. The experimental activity took place at the Radiation Biophysics Laboratory of the Physics Department "E. Pancini", University Federico II of Naples and at the Laboratory of Experimental Surgery, Department of Clinical-Surgical Sciences located in University of Pavia, Polo Cravino. Photon irradiations took place in Naples at the Radiation Biophysics Laboratory. Neutron irradiation was carried out in the thermal column of the TRIGA Mark II research reactor of the University of Pavia.

As for the experimental part of this work, three radiobiological assays were used to quantify IR-induced DNA damage: the Ionizing Radiation-Induced Foci (IRIF) Assay and two Fluorescence In Situ Hybridization (FISH)-based technique, i.e., Whole Chromosome Painting (WCP) and Multicolour(m)FISH. The former assay allows to quantify dose-dependent DSB induction and their time-dependent decline, hence it is used to determine the repair kinetics after irradiation by examining the fluorescent signals (foci) due to the co-localization of early repair events elicited by IR-induced DNA DSBs, specifically histone γH2AX phosphorylation processes and 53BP1 protein recruitment. The measurement of the frequency and dimensions of these signals at times subsequent to exposure allows to quantify the efficiency of the repair mechanisms, and therefore their impairment due to the expected clustered damage in the case of the high-LET particles generated by the neutron capture reaction. The other assays, i.e., WCP and mFISH, allow to accurately measure the induction of chromosomal aberrations (CAs), resulting from erroneous repair of IR-induced

DSBs, and in the case of mFISH, the frequency of complex chromosomal rearrangements, a well-known biomarker of exposure to high-LET radiation. All measurements post-irradiation were performed at the Radiation Biophysics Laboratory.

This work is organized into four chapters:

* Chapter 1 provides an introduction to BNCT and to the techniques used to evaluate the IR-induced DNA damage.
* Chapter 2 deals with Geant4DNA Monte Carlo simulations.
* Chapter 3 describes the materials and experimental methods adopted.
* Chapter 4 presents the obtained results and their discussion.

Finally, conclusions are discussed together with an outline of future perspectives.

1. The physical and radiobiological rationale underlying Boron-Neutron Capture Therapy (BNCT)

Boron-Neutron Capture Therapy (BNCT) is an anti-cancer radiotherapeutic method that exploits the $^{10}B(n,\alpha)^{7}Li$ reaction using boron-10 (^{10}B) carrier(s) and thermal neutron irradiation. In principle, BNCT provides an alternative and unique approach compared to photon/electron-based conventional radiotherapy by delivering highly DNA-damaging charged particles at intracellular level, almost exclusively inside the tumour. It biologically and physically targets tumours via a binary system that consists of two separate components to achieve its therapeutic effect. Such components become highly lethal to cancer cells when combined [1]. Because the range of the reaction products is only about 10 μm, which is close to the diameter of a single cell, the capture reaction triggered by thermal neutron irradiation causes significant damage only to cells that have taken up the tumour-seeking ^{10}B-compound. Moreover, the biological effectiveness at causing cell death of α-particles and ^{7}Li ions is not dependent on the oxygen concentration, hence they exhibit the same lethality in both normoxic and hypoxic environments [2]. This is important since most tumours are characterized by a physiologically high level of hypoxia, which confers them radioresistance when conventional radiotherapy is used [3]. Figure 1 shows the cellular mechanism of BNCT. Ideally, only tumour cells should incorporate the boron carrier: this can be obtained by exploiting the different metabolism between cancer and normal cells [3]. Therefore, successful BNCT is dependent on different factors, such as the absorption rate of the ^{10}B delivery agent, its pharmacokinetics, the location and depth of the lesion, as well as the availability of neutrons at appropriate energy and quantity to trigger the reaction [2]. In the next paragraphs the physics of the nuclear reaction $^{10}B(n,\alpha)^{7}Li$, the state of the art of BNCT and some radiobiological insights are presented to better understand the expected extent of radiation-induced damage to tumour cell DNA by BNCT.

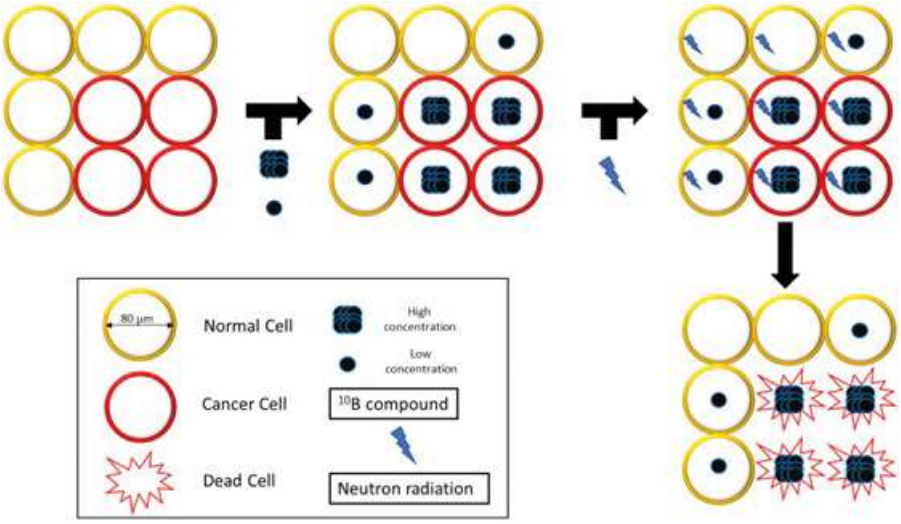

Figure 1 Cellular mechanism of BNCT [1].

1.1.The $^{10}B(n,\alpha)^{7}Li$ nuclear reaction

BNCT has been proposed as a binary form of radiation therapy exploiting the high propensity of the nuclide ^{10}B to capture thermal neutrons, which results in the prompt nuclear reaction $^{10}B(n, \alpha)^{7}Li$. ^{10}B is an excellent element for such a form of neutron capture-based therapy, as it is non–toxic, non–radioactive and fairly abundant in nature (isotopic abundance 20%). The basic nuclear reaction is shown in more detail below:

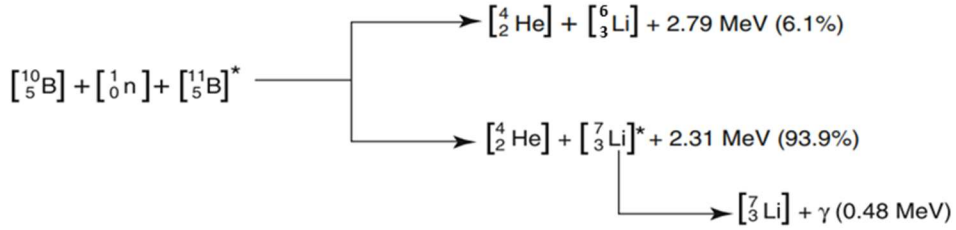

Figure 2 Details about the nuclear processes underlying BNCT [3]

The reaction cross-section at thermal neutron energies, 0.025eV, (σ = 3840 barns) is the highest among those associated with other interactions of neutrons with biologically relevant elements (hydrogen = 0.33 barns, nitrogen =1.84 barns, carbon = 0.0034 barns, oxygen = 0.00018 barns [4]). In Figure 3 is shown the neutron total cross-section for different elements that can be found in biological tissues as a function of neutron energy. The capture process leads to the production of an excited $^{11}B^{*}$ nucleus, which decays almost immediately into two densely ionising particles: a ^{7}Li ion (of energy equal to 0.8 MeV) and an α-particle (1.5 MeV). These possess a high Linear Energy Transfer or LET (for the α-particle it is approximately 150 keVμm^{-1}, for the ^{7}Li-nucleus approximately 175 keVμm^{-1}), which is radiobiologically regarded as linked to greater cell lethality than photons, as we shall see later. The path lengths of these particles are in the range of 4.5–10 μm in water or tissues, hence the energy is deposited within the cell. Theoretically, therefore, it is possible to selectively irradiate those tumour cells that have taken up a sufficient amount of ^{10}B and simultaneously spare normal cells, thanks to the selective boron absorption [3].

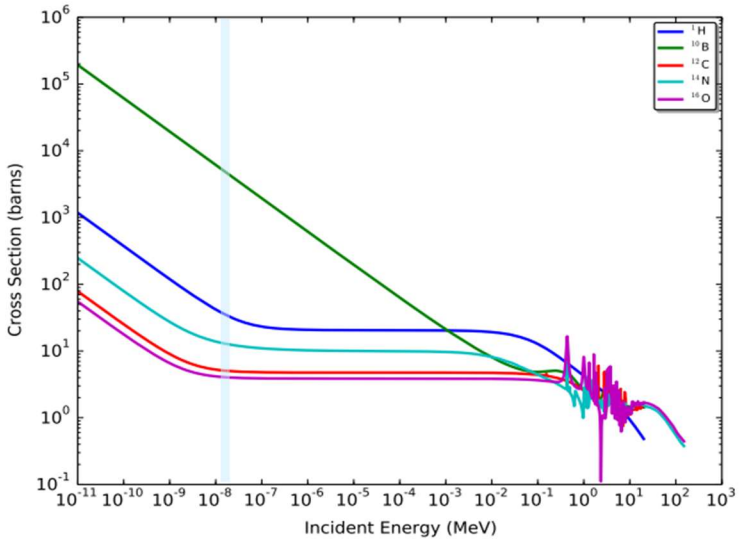

Figure 3 Neutron total cross-section for ^{1}H, ^{10}B, ^{12}C, ^{14}N, ^{16}O as a function of neutron energy [5]. The blue line approximately indicates the energy of thermal neutrons.

It is important to note that, beyond the nuclear reaction on which it is based, the BNCT entails a mixed radiation field, whose components must be taken into account in order to establish their contribution to the actual absorbed dose. Indeed, neutron irradiation will produce a background dose due to: the low-LET gamma rays from the capture of thermal neutrons by hydrogen and from the photons present in the neutron beam; intermediate-LET protons originated by the scattering of fast neutrons and by thermal neutron capture in nitrogen.

1.2. State of the art of BNCT

The earliest conceptual framework for neutron-capture therapy was first theorized in the mid-1930s by astrophysicist Gordon Locher [1]. Kruger published the first experiments on BNCT in 1940 [6]. He treated tumour fragments in vitro with boric acid and neutron irradiation. After implantation in mice, these tumours showed a lower transplantation efficiency compared to controls, which had been treated only by boric acid or thermal neutrons, respectively. Ten years after these early radiobiological experiments, the first clinical applications in humans were performed [3]. Clinical studies of BNCT for glioblastoma multiforme, melanoma, recurrent head and neck tumours, lung and liver metastases, mesothelioma, extra-mammary Paget's disease have been performed or are underway in the United States, Japan, Sweden, Italy, Finland, Argentina and Taiwan (among others) employing mostly nuclear reactors as the neutron source [7]. To date, the clinical results show a significant therapeutic effectiveness, associated with an improvement in patient quality of life and prolonged survival, although margins for improvement exist [8]. These studies altogether concurred to the notion that for a BNCT treatment to be successful, a sufficient number of ^{10}B atoms must be delivered to the tumour, which was pinpointed as at least 10^9 atoms/cell or 20–30 mg of ^{10}B per g of target mass, and a sufficient thermal neutron fluence must be absorbed in the tumour. As mentioned above, an ideal boron carrier should be non-toxic at therapeutic dose levels and should accumulate preferentially in the tumour [7]. To date, two boron compounds have been extensively used in BNCT clinical trials: mercaptoundecahydrododecaborate-^{10}B (BSH) and boronophenylalanine (BPA), whose chemical structures are shown in Figure 4.

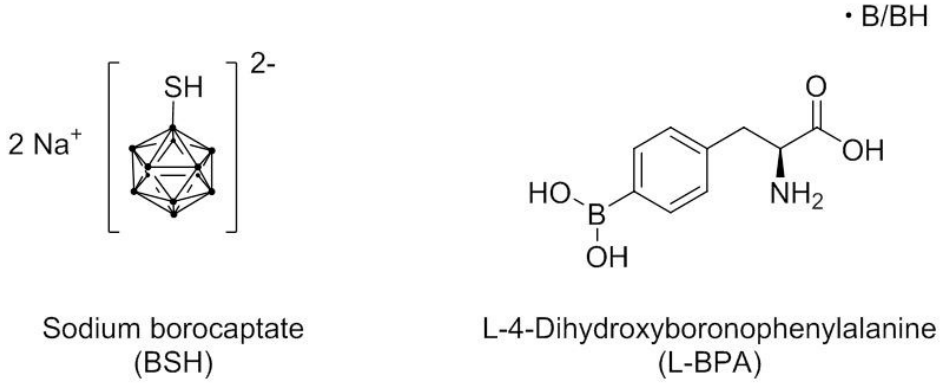

Figure 4 Chemical structures of BSH (left) and L-BPA (right).

BSH is a water-soluble diffusive drug, principally used for malignant glioma. It does not cross the Blood Brain Barrier (BBB) into normal brain but it may accumulate in brain tumours because of their disrupted BBB. However, since BSH has poor membrane

permeability, its accumulation in tumour cells is low. On the other hand, BPA has been used for several pathologies and showed better results than BSH. BPA is an amino-acid derivative actively incorporated by tumour cells by the L-type amino acid transporter 1 (LAT1), whereas a small amount is taken up by LAT2. Tumour cells overexpress LAT1 versus normal cells, but LAT2 is expressed in both. However, since LAT2 transports less BPA than LAT1, a preferential accumulation of BPA is achieved in tumour cells. Despite their clinical use, both compounds exhibit several limitations [7]. This is why novel boron delivery agents are under development such as antibodies, liposomes, nanoparticles, boron cluster agents and carrier proteins conjugated with boron compounds [7, 9]. In Figure 5 the potential of antibody conjugated with boron-enriched linkers (BELs) is briefly described [9]. These antibodies bind to receptors on cell surface and, after internalization, release the ^{10}B atom.

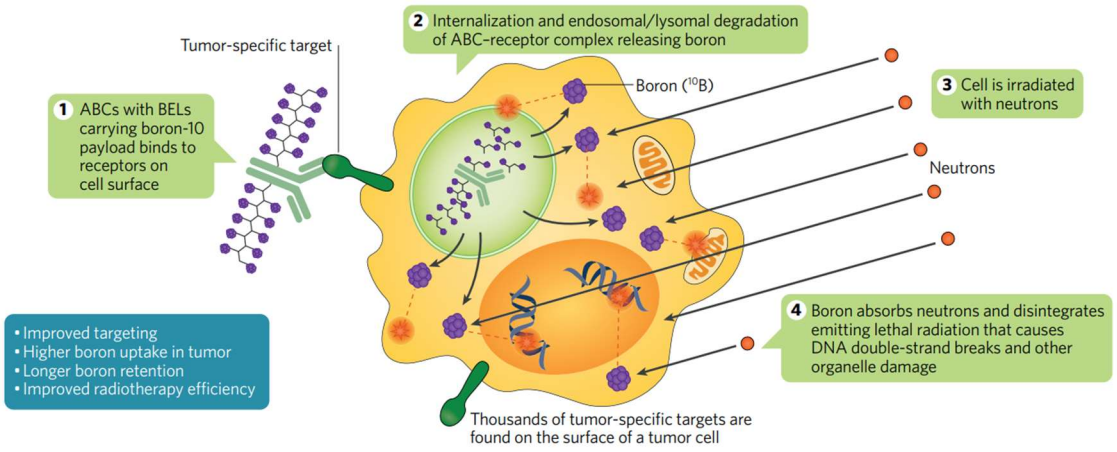

Figure 5 Antibody boron conjugated with boron-enriched linkers (BELs). Traditionally, BNCT has relied on the incorporation of boronophenylalanine in tumour cells due to their higher amino acid uptake rates compared with non-tumour cells. A novel approach relies on the use of antibodies loaded with BELs with the goal to improve targeting and increase both specificity for tumour cells and boron-loading of the cells for BNCT. ABC, antibody boron conjugate [9].

Optimising the delivery of boron compounds will improve the effectiveness of BNCT, allowing this therapy to encompass more tumour types and a larger pool of patients. Moreover, the understanding of the radiobiological mechanisms induced by BNCT will contribute to identify markers of cellular response to BNCT and may serve to modulate signalling pathways to enhance BNCT therapeutic efficacy and reduce associated toxicity [7]. Thus, BNCT radiobiological studies are needed in order to design novel, safer and more effective clinical protocols for existing or new targets of BNCT. To conclude this succinct overview of BNCT, the emerging trend is to perform radiobiological studies and clinical trials using Accelerator-Based BNCT (AB-BNCT) neutron sources (Figure 6). The knowledge gained from BNCT radiobiological studies in reactor-based neutron sources will pave the way in this new era. Accelerators are beneficial in terms of public acceptance; they involve less complex, less expensive and a more compact technology; they can be installed in hospitals because they can be marked as medical devices. AB-BNCT radiobiological studies in different models are necessary to explore potential differences and similarities between the radiobiology involved in reactor-based and AB-BNCT, the mechanisms specifically involved in the effects of AB-BNCT and strategies to enhance it [1, 7].

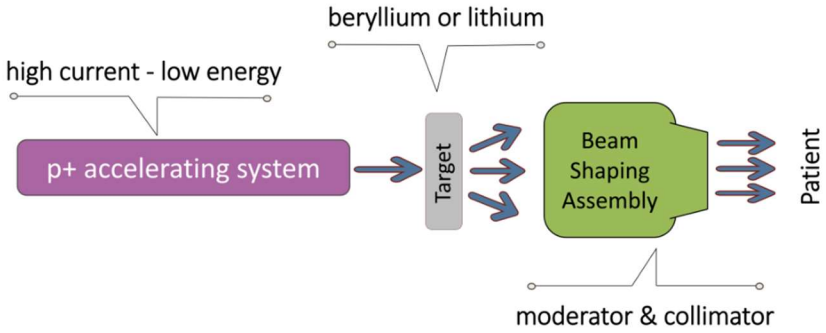

Figure 6 Diagram of the general structure of an accelerator-based BNCT facility.

1.3. DNA Damage Response (DDR) and Ionizing Radiation-Induced Foci (IRIF)

Cells cope with a tremendous amount of spontaneous DNA damage that arises from naturally occurring reactive oxygen species (ROS), reactive nitrogen and carbonyl species, lipid peroxidation products, the chemical lability of DNA, and other endogenous sources [10]. DNA damage is also caused by exogenous agents such as ultraviolet (UV) and IR. In particular, the ability of IR to cause lethal DNA damage is the justification for its use in cancer radiotherapy. In fact, the main reason why the primary cellular target of IR is DNA is the fact that the latter is present in a single copy, unlike the various organelles and other cellular biomacromolecules. Maintaining DNA integrity not only is a prerequisite for cell survival but it is also fundamental to abate the risk of radiotherapy late effects such as radiation-induced carcinogenesis. Due to the direct or indirect action of IR, different types of damage can be generated, such as (in increasing order of severity) [11]:

* damage to nucleobases in DNA;
* interruption of the sugar-phosphate bond in DNA;
* creation of ectopic DNA-DNA and DNA-protein cross-links;
* Single-Strand Break (SSB) when only one of the two strands is damaged;
* Double-Strand Break (DSB), occurring when both strands are damaged. When multiple DSBs are spatio-temporally close together, we talk about "Clustered DNA Damage" (mainly caused by high-LET radiation).

As mentioned, the therapeutic advantage of BNCT in killing cancer cells is thought to derive from the high-LET secondary particles generated from the n-^{10}B reaction, that is in their propensity to generate clustered DNA damage. This is defined as complex lesions or locally multiply damaged sites that extend for 10-20 bp (base pairs), corresponding to approximately 1-2 double helix windings. The degree of complexity of the clustered lesions is linked not only to the presence within them of permutations of all types of the damage types listed above, spatially-temporally close together, but also to a number of additional factors, such as: the degree of chromatin condensation of the gene sequence involved; the different phase of the cell cycle of the affected cell and the potential interference between multiple DNA repair pathways induced by damage reporting systems [10]. Different levels of effect can be ascribed, for the same absorbed physical dose, to different radiation qualities (a function of their LET), as in the case of the BNCT in which, in fact, there is a mixed field

[2]. In Figure 7 the relationship between DNA damage complexity and reparability, mutagenesis and cytotoxicity, is shown. The cell reacts to DSBs through a complex signalling mechanism known as DNA Damage Response (DDR), which involves the reorganization of chromatin and the promotion on the site of breakage of groups of repair-dedicated proteins [10].

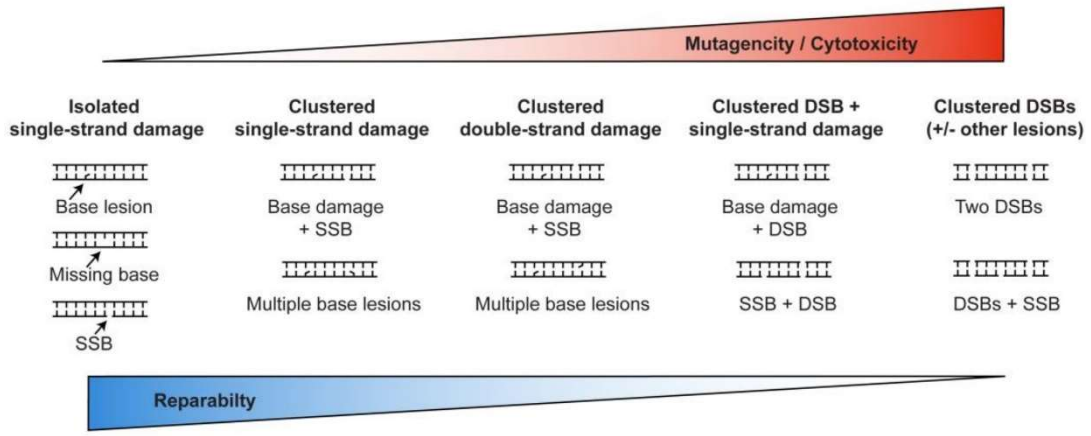

Figure 7 Relationship among DNA damage complexity, reparability, mutagenesis, and cytotoxicity. The triangles above and below indicate lesser to greater biological effects that are inversely proportional to the reparability of isolated vs. clustered DNA lesions [10].

1.3.1. Double-Strand Break (DSB) repair pathways

Cellular damage response pathways are expected to be activated even after the induction of low levels of biological damage in DNA, proteins or lipids [12]. To mitigate threats on genome integrity posed by powerful genotoxic agents like high-LET radiations, as already mentioned, cells have evolved a complex set of repair mechanisms collectively called the DNA Damage Response (DDR). DDR coordinates DNA repair, DNA replication, and cell-cycle checkpoint pathways and determines cell fate, via processes including apoptosis and senescence [11]. Various DNA repair mechanisms are engaged for the processing of DNA damaged sites, especially as regards the repair of DNA DSBs, the most cytotoxic lesion if un/mis-repaired. The main pathways responsible for the repair of DSBs are the Homologous Recombination (HR), the classical Non-Homologous End Joining (c-NHEJ) and the backup Non-Homologous End-Joining (B-NHEJ or alt-NHEJ). In Figure 8 some details are shown about the different proteins involved in such processes.
In all phases of the cell cycle, DSBs can be repaired via NHEJ, which involves the direct ligation of DSB ends, but without restoring the original sequence, thereby resulting in a loss of genetic information. The first proteins to accumulate at the sites of DSBs are the sensor complexes of Ku70/Ku80. DNA-PKcs[1] interacts with several "end processing proteins", proteins that process the end of the breaks, to clean-up "dirty" ends, and once processed, the ends are ligated, restoring the DNA strand integrity[13]. On the other hand, HR promotes, in principle, complete repair by copying the lost information on the damaged strands from an intact homologous DNA template, preferentially the sister chromatid when available, and therefore it acts in S/G2 [14]. HR restores both integrity and correct sequence; however, if faulty, it is the main cause for reciprocal translocations, one of the possible chromosome aberration rearrangements (see below). Finally, B-NHEJ is activated when both c-NHER

[1] DNA-PK complex catalytic subunit (DNA-PKcs) is a protein belonging to the family of phosphatidylinositol-3-kinase related kinases and is a key enzyme in the repair of DSBs.

and HR are not available or suppressed. It benefits from short (2 to 20 bp) stretches of microhomology that are exposed following limited processing of DSB ends [15]. B-NHEJ operates with slower kinetics and lower efficiency than c-NHEJ and consequently is more error-prone. Thus, deletions and other modifications at the break junction are larger than after c-NHEJ. Indeed, B-NHEJ is considered a dominant source of structural chromosomal abnormalities [15]. To provide damaged cells sufficient time to repair, DNA DSB repair systems initiate signal-transduction pathways to activate G1/S, intra-S, and G2/M cell-cycle checkpoints. In the presence of irreparable damage, checkpoint signalling can also induce apoptosis, a form of genetically controlled cell death, also known as Programmed Cell Death (PCD) [14].

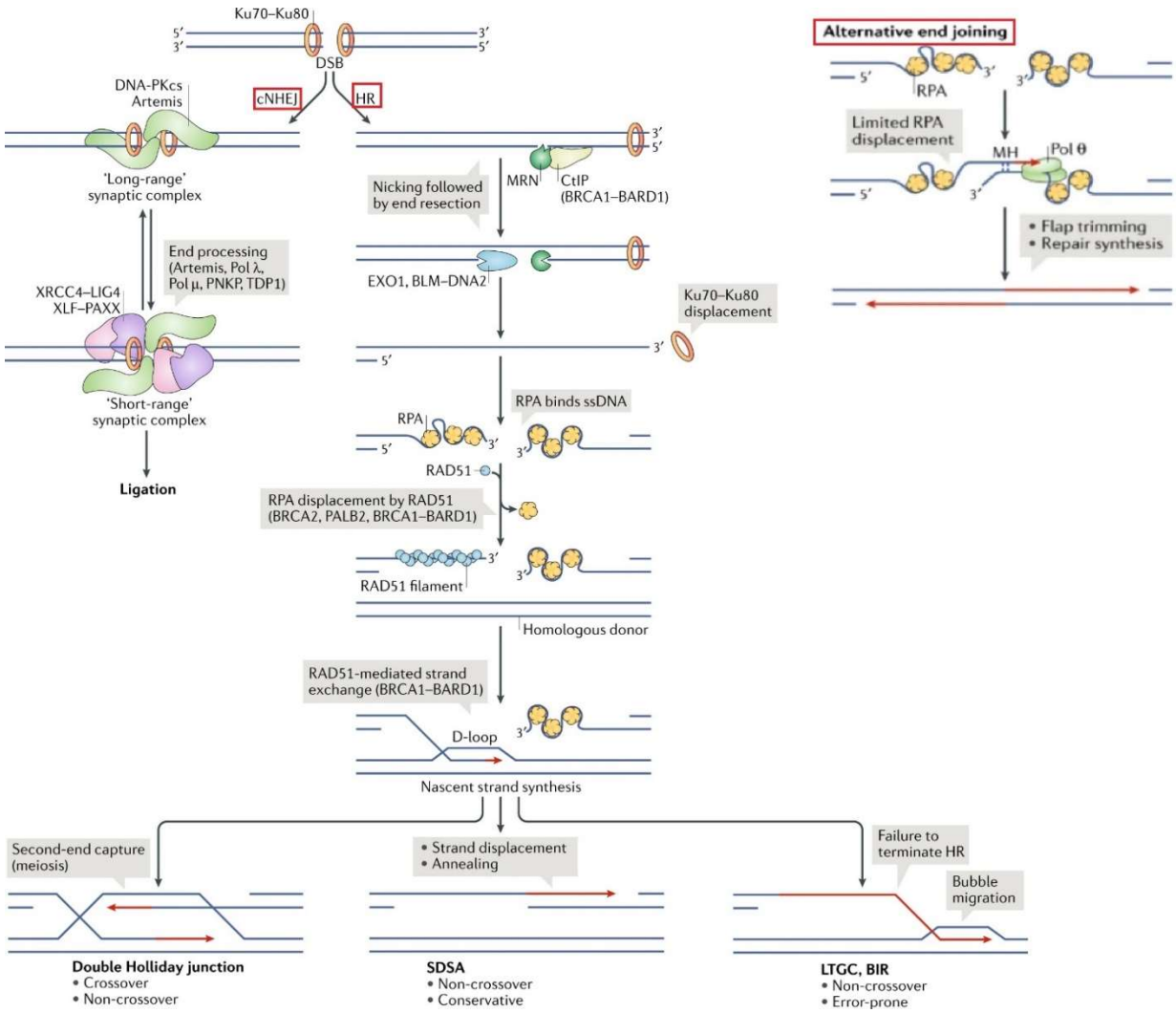

Figure 8 The binding of the Ku70–Ku80 heterodimer to DNA ends schedules repair of DNA DSBs by cNHEJ. DNA end ligation and processing by cNHEJ enzymes are restricted to the short-range complex. The default engagement of cNHEJ can be disrupted by DNA end resection, which facilitates repair by HR. Resection is enabled by the endonuclease activity of the MRE11–RAD50–NBS1 (MRN) complex. The replication protein A (RPA) complex avidly binds to DNA and must be displaced by recombination 'mediators' to allow the formation of a RAD51 nucleoprotein filament. Breast cancer type 2 susceptibility protein (BRCA2) is the major recombination mediator in mammalian cells, likely acting in concert with partners and localizers of BRCA2. In meiotic cells, formation of a double Holliday junction intermediate can lead to crossing over. Alternative end joining (B-NHEJ) re-joins DNA ends without use of cNHEJ proteins. B-NHEJ involves limited displacement of RPA, which reveals microhomology (MH) between strands and facilitates repair. [16]

The choice of the repair pathway for DNA DSBs primarily depends on radiation quality (Figure 9), but there are still some doubts. In the case of DSB repair of high-LET induced lesions, the literature supports the notion that NHEJ processes are fundamentally poor at, or possibly even "inhibitory" to, the resolution of highly clustered DSBs in a timely manner [13, 15]. In particular, Chu-Yu et al. found that BNCT resulted in delayed HR and inhibited NHEJ), suggesting that probably the major role in DNA DSB repair at early stages is played by B-NHEJ [17]. The induction of DNA lesions of diverse and varying levels of complexity is expected to trigger simultaneously different DNA repair pathways [18]. One well-supported hypothesis is that this temporal simultaneous activation of different repair pathways, like NHEJ for DSBs as well as base excision repair (BER) for non-DSB lesions, signifies a "stress factor" to genomic region or DNA repair centre[19]. Inter-lesion spacing is an important factor in the generation of novel DSBs from the repair of non-DSB clustered damage, where distances of 3–8 nucleotides are sufficient to avoid interference of the repair machinery at these clustered damage sites depending on the type of lesion [13]. Thus, mutations in clustered lesions may arise directly, due to inaccurate repair, or indirectly, because persistent damage clusters intercepted by replication forks are more likely to cause replicative stress-induced DSBs [20].
It is evident that large gaps of knowledge exist in the field that must be filled by future research. To date, the repair of mixed radiation-induced complex DNA damage is still poorly understood [21].

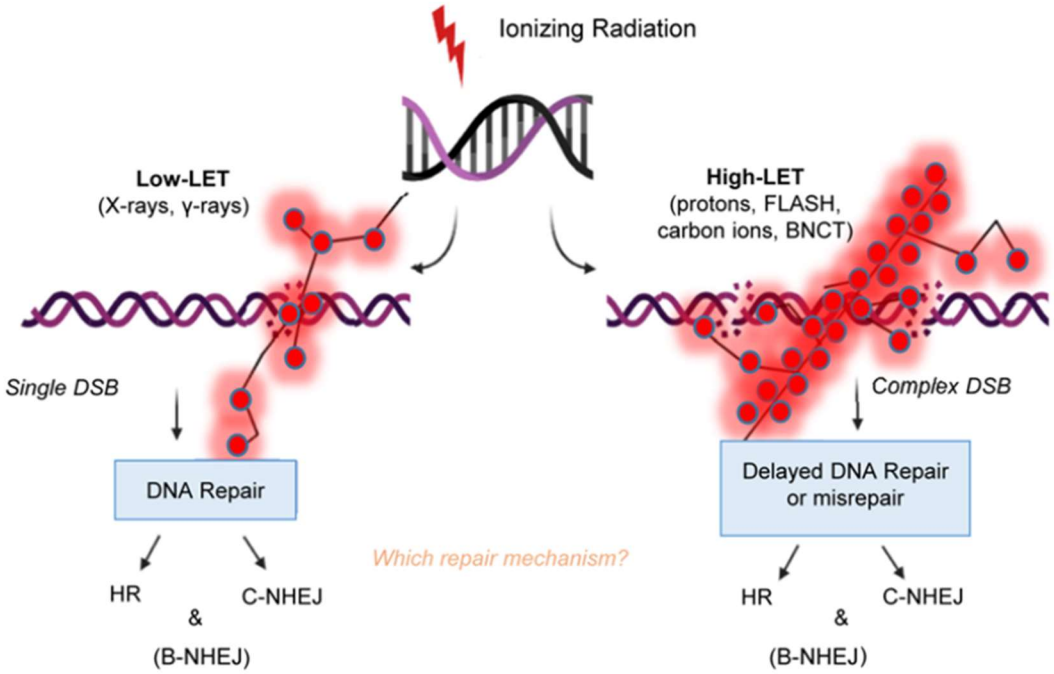

Figure 9 . DSB repair pathways after low- (left) and high (right)-LET radiation [12].

1.3.2. 53BP1 and γH2AX as biomarkers of DDR-related IRIF: the Foci assay

The phosphorylation of H2AX on Ser 139, named γH2AX, is an early response to the generation of DNA DSBs and extends along megabase-long domains, from both sites of the lesion, supporting amplification of signal transduction pathways [14]. After the damage has been caused, the cell triggers a cascade signalling mechanism, beginning with the

phosphorylation of the histone γH2AX mediated by the MRN complex of ATM (a phosphatidylinositol protein 3-kinase encoded by the Ataxia-Telangiectasia Mutated or ATM gene), followed by the recruitment of MDC1 (Mediator of DNA damage checkpoint 1) and the activation of RNF8-RNF168 chromatin-ubiquitin dependent complex [22]. γH2AX forms large, bright, and discrete foci with a random distribution throughout the nucleus but not within the nucleoli area[14]. An important regulator of DDR is the p53-binding protein 1 (53BP1), a 1972-long polypeptide chain, which serves as a binding partner for the p53 tumour suppressor and contains multiple interaction interfaces (molecular scaffold) for various DSB-responsive proteins [22]. 53BP1 accumulates on damaged chromatin to interface between methylated histone residues and proteins that belong to the signal-transduction pathways, mediating cell-cycle arrest or apoptosis [14]. In the G1 phase of cell cycle, 53BP1 exists in a diffuse nuclear pattern as well as in large nuclear “dots” under microscope inspection. During DNA replication, in the S-phase, 53BP1 can be found in a discrete, punctuate pattern. The nuclear distribution pattern of 53BP1 in G2 cells appears in two forms, one similar to that in S-phase but with fewer foci and one that exhibited few, if any, large dots [14]. 53BP1 plays a key role in the choice by the cell of the most appropriate repair pathway: NHEJ, dominant during the G1 phase of the cell cycle, in the absence of a homologous duplicate that can act as a template for DNA; HR, which allows the reconstruction of the damaged double helix segment thanks to the availability of the sister chromatid during the late S phase and the G2 phase [11].
The importance of γH2AX and 53BP1 in DDR pathways means that these can act, at the cellular level, as biological markers of DSB sites also known as "Ionizing Radiation-Induced Foci" or IRIF. Foci facilitate repair and amplification of the checkpoint signal by orchestrating ordered recruitment, assembly, and activation of further repair and signalling proteins [14]. Thus, after irradiation, DSB sites can be visualized as IRIF, using immunocytochemistry methods, based on molecular hybridization, combined with fluorescence microscopy by using fluorochromes conjugated to proteins of interest that selectively bind those proteins involved in DDR [14]. This makes the foci visible as discrete fluorescent spots within the cell nucleus. The demonstration of precise γH2AX localization to the sites of DNA DSBs was achieved by means of a laser scissors experiment, where DSBs were introduced through a pulsed laser microbeam driven along a predetermined course. On the other hand, the notion that 53BP1 marks the sites of DNA DSBs has been documented by colocalization experiments of 53BP1 with γH2AX and other repair factors known to form DDR complex [14].
One of the main techniques used to assess DSB damage is the so-called foci assay, which typically uses colocalization of γH2AX and 53BP1, purposely marked with specific antibodies. The appropriateness of using γH2AX alone as an IRIF marker has often been debated due to difficulties in reaching a clear consensus on what should be considered as DSBs foci, even within the same laboratory. A pilot experiment based on the exchange between laboratories of slides with cells suitably treated with fluorophores the foci of γH2AX foci revealed significant differences both in the quality of the staining of the samples and in the results of the counts [23]. In addition, there exists a biological complication as sometimes there is not a direct, one-to-one correlation between the number of γH2AX-positive foci and the number of DSBs induced by IR, due to phosphorylation of H2AX linked to changes in chromatin structure in processes of oscillation of the DNA/chromatin domains. Moreover, the number of γH2AX foci also depends on culture conditions, cell-cycle phase and senescence [24]. This has helped refine the use of 53BP1 in combination with γH2AX as a more consistent molecular marker for IRIF count and it has been used in this work.

1.3.3. IRIF dynamics

Currently, it is becoming clear that DSB-associated foci are dynamic chromatin structures juxtaposed to the lesion, where repair, signal transduction, chromatin, and structural proteins are bound onto the DNA. Many repair and signalling factors are known to translocate to such foci in a time-dependent manner. These factors are afterward released from the focus to perform functions in the nucleoplasm or cytoplasm. γH2AX focus formation pattern after low-LET radiation typically follows a fast kinetics: foci appear as small and numerous dots within 1–3 min, become fewer in number but larger and better detected at 15 min, stay steady in size and number between 15 and 60 min, decrease in number at 180 min, and eventually almost disappear at 24–48 h [14]. On the other hand, 53BP1 foci form within minutes of irradiation. 53BP1 foci colocalize with γH2AX [14]. The number of 53BP1 foci increases linearly over time, reaching a maximum at about 15–30 min, and then steadily decreases to baseline levels usually within the next 16 h. Depending on the complexity and location, DSBs are subject to a variable kinetic repair mechanism. Most IR-induced DSBs are subject to rapid repair as these, especially in the case of low doses and/or low LET radiation, are individually spaced (simple DSBs). Post-irradiation repair cytokinetic mechanisms studies using X-rays show that the number of foci per cell in the hours immediately following irradiation decreases significantly within 24 hours, demonstrating the effectiveness of the repair mechanisms provided by the cellular DDR. From the measurements made on the size of the spots it is observed instead that the average area of the foci tends to increase post-irradiation: this promotes the idea that the repair rate of DSB depends on the complexity of the damage and that the permanence of foci after a “long” interval from irradiation is an indication that the cell cannot repair lesions more complex in nature (Figure 10) [25].

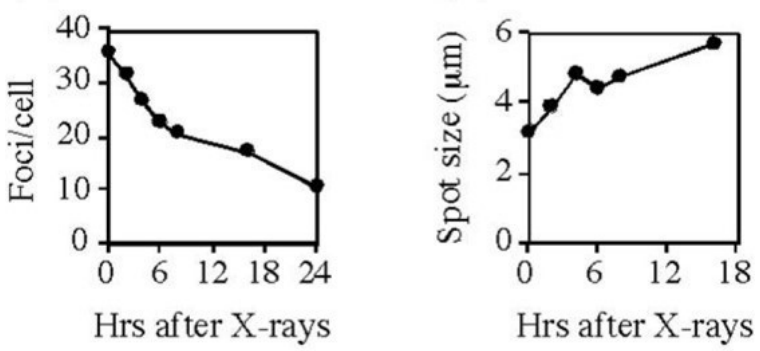

Figure 10 Repair kinetics by cellular DDR following X-ray exposure: on the left, the number of foci per cell as a function of time after irradiation; on the right, the average size of fluorescent spots, as a function of time elapsed from exposure to IR [25].

In fact, complex DSBs (clustered damage) will require more time to repair, and larger foci are formed. In studies with high-LET radiation, IRIF usually appeared with dose-dependent delay and disappeared with slower kinetics as compared to simple DSBs[26].
A limitation to the detection of IRIF by colocalization techniques is related to 53BP1 relocations at the DSB focus. The different localization kinetics of γH2AX and 53BP1 is due to the increased phosphorylation of histone H2AX even outside DSB sites after exposure to IR: the γH2AX foci may still persist after the DSB has been repaired, due to the gradual dephosphorylation or degradation of the histone. It is unknown how this process is

orchestrated in time and space and if it is sensitive to changes in other factors. Moreover, as mentioned before, the presence of γH2AX foci alone may not necessarily indicate the presence of a physical DSB at the time of analysis [26]. It is also important to note that DDR proteins are often thought to diffuse in a passive energy-independent manner by scanning the nuclear volume for high-affinity binding sites. On the other hand, 53BP1 foci do not form at low temperature or in ATM-depleted cells [26]. These data provide evidence for energy-dependent active transport of DSB repair proteins [26].

1.4. Radiation-induced chromosomal aberrations

The last paragraphs have focused on: the types of radiation-induced damage to the DNA, the early events after the lesions and their repair mechanisms. Here, we focus on the consequences of an erroneous repair of the DSBs, which can result in rearrangements and structural changes in DNA (structural chromosome aberrations, CAs) such as deletions, translocations and dicentrics. CAs may lead to the activation of oncogenes and/or the loss of tumour suppressors, which in turn favours the initiation of malignant transformation. Complex-type CAs, involving more chromosomes, arise following high-LET radiation already at low doses, as also said later. Although each CA-containing damaged cell may present a unique rearrangement, it is expected that the qualitative "form" of the observed rearrangement will reflect the initial spectrum of the DSB damage induced, which strongly depends on the energy deposition pattern [27]. Structural chromosomal rearrangements reflect both the amount and the pattern of energy deposition events by IR on the (sub)micrometric scale. Therefore, their frequency correlates with overall radiation-induced DNA damage, and an increased proportion of complex aberration types reflects exposure to higher radiation LET. IR-induced rearrangements are the result of DSB misrepair and become visible and measurable at mitosis [28]. However, Premature Chromosome Condensation (PCC) techniques allow the scoring of CAs also in cells from G1 and G2 phases [29].
Historically, different configurations have been studied regarding the types of CAs leading to their classifications [30]. The simplest one derives from the interaction between two chromosomes each with a single break and are divided into:

* Translocations (Figure 11, left), where an acentric fragment of a chromosome recombines with the centric fragment of the other.
* Dicentric (Figure 11, right), when the centric parts are joined together.

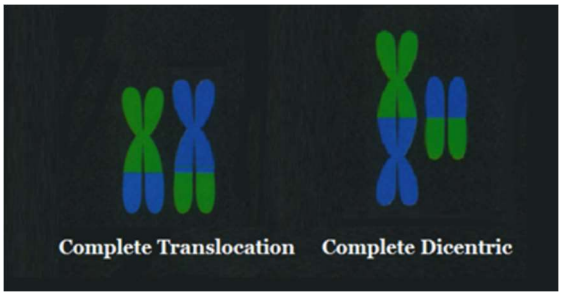

Figure 11 On the left an example of a complete translocation; on the right, an example of a complete dicentric [30].

Translocations are also defined as complete if the centric and acentric fragments of the chromosomes involved in the exchange recombine with each other (as in Figure 11, left). The

definition of completeness also applies in cases where the centric fragments of the two chromosomes are joined, forming a dicentric, and the acentric ones too (as in Figure 11, right) [28]. On the other hand, complex exchanges require the interaction of three or more chromosomal breaks with the possible involvement of multiple chromosomes. A rule of thumb to classify exchanges between chromosomes is the so-called CAB (Chromosome, Arm, Break) criterion. The basic complex-type aberration is defined as an exchange with a CAB equal at least to 2, 2, 3: this is originated by two chromosomes and three breaks involving two arms. Complex exchanges are also often accompanied by a loss of information related to the genetic material involved in the damage [30]. Examples of this type of aberrations can be observed in Figure 12. Such CAs are universally considered a biomarker of high-LET exposure [30].

Figure 12 A complex aberration 4/4/4 according to the CAB classification [30].

In the context of complex CAs there are:

* Insertions, when a fragment of a chromosome is inserted into another chromosome.
* Rings, which originate by a breakage on each arm of the same chromosome and the reunification of the two ends.

The listed aberrations are also associated with deletions and fragments. The former are originated by the loss of information linked to a portion of a chromosome, while fragments may be centric or acentric parts of chromosomes involved in complex exchanges or exist independently as portions of chromosomes not completely recombined.

1.4.1. The multicolour Fluorescence In Situ Hybridization (mFISH) technique as a tool to unveil BNCT-associated complex DNA damage

The increased biological efficacy of high-LET IR is reflected by a large increase in cell killing that has been explained as deriving from an increase in the yield of “clustered” DSBs [31]. DSB-repair pathways are different in terms of properties and fidelities: this indicates that they cannot be considered as equivalent alternative of DSB-repair; consequently, the repair mechanism is chosen to accommodate necessities, for example to consider the increased complexity of high-LET IR damage. Indeed, DSBs induced by high(er)-LET IR have different processing requirements than those induced by low-LET IR, including increased engagement of HR. Thus, the most consequential effect of high-LET IR and the type of DSBs it induces, is to shunt them from c-NHEJ to resection-dependent processing by HR and B-NHEJ. Notably, despite increased engagement of HR on complex DSBs, more than 75% of

them are still processed by other repair pathways. Since c-NHEJ fails to engage on complex DSBs, it follows that the remaining 75% are processed, for example, by B-NHEJ [31].
Clusters of DSBs can result in complex exchanges, which require the interaction of multiple chromosomes and involve the presence of a high number of breaks, because of a misrepair from B-NHEJ pathway [31].
Therefore, an increase in the ionization density corresponds to an increase, in proportion, of complex exchanges, which, in the case of BNCT, would indicate the likelihood that damage is caused by the α-particles and/or lithium ions generated by the capture reaction. The radiation track structure does determine the "forms", as well as the total yield, of aberration induced, supporting the view that spatial proximity between induced DSB influences the chance of their interaction [27].

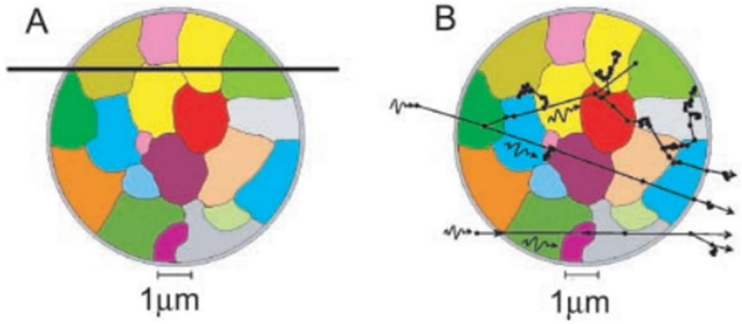

Figure 13 Transverse section, at maximum diameter, of a modeled peripheral blood lymphocytes cell nucleus showing individual chromosome domains being crossed by an α - particle (A) and electron tracks from two X-ray interactions (B) [27]. The spatial proximity, characteristic of high-LET radiation, between induced DSB by the α-particle can cause complex exchanges with high probability.

The full spectrum of cytogenetic complexity of the aberrations cannot be revealed by standard Fluorescence In Situ Hybridization (FISH) techniques, such as Whole Chromosome Painting (WCP) of specific chromosomes (chromosomes 1 and 2 are the usual choice because of their size), because the number of "painted" chromosomes is limited. The development of multicolor(m)-FISH has enabled the discrimination of the whole karyotype by means of the combinatorial labelling of individual chromosomes with spectrally distinct fluorophores. With the exception of interchanges between homologues, mFISH allows all of the chromosomes participating in each aberration to be detected, and the level of complexity encompassing aberrant chromosomes to be determined. The damage induced by the traversal of a α-particle is expected to result in the formation of numerous "hidden" intrachromosome rearrangements [27], hence also mFISH could underestimate the yield of exchanges, yet to a little extent.

2. Monte-Carlo simulations in radiobiology

The advancement of multidisciplinary research fields, such as radiobiology, radiation protection and medical physics, dealing with IR-induced biological damage, requires a clear mechanistic understanding of how cellular damage is produced by IR. Generally, the characterization of such mechanisms is performed using radiobiological assays and techniques, often exploiting molecular-biology-based methodologies and indeed much has been unveiled thus far on the relationship between, for example, energy deposition patterns by radiations of varying quality and the severity of the resulting DNA lesions. However, also computational simulations have increasingly become an important tool for the prediction of biological effects on a nanoscale level, which is very hard to achieve with classic radiobiological assays. Furthermore, theoretical modelling of a wide spectrum of biological effects, ranging from DNA breakage to cellular survival has significantly aided the planning of experiments and interpretations of their results [32]. The Monte-Carlo (MC) method is a computational technique that simulates realistic phenomena by random sampling of the space of possible events. Such an approach has applications in different fields like environmental sciences, semiconductor devices simulation, financial market, radiobiology and medical physics; in fact, some radiotherapy treatment planning codes make use of it [33]. Significant progress has been achieved during the last decades in the development of accurate computational tools capable of simulating mechanistically the passage of radiation through matter exploiting the MC method [34]. It is well known that this method requires a large amount of computing power [34], but it provides a high accuracy. In Figure 14 the potentialities of MC algorithms are pointed out compared to analytic algorithms in terms of time to resolve a problem versus its complexity.

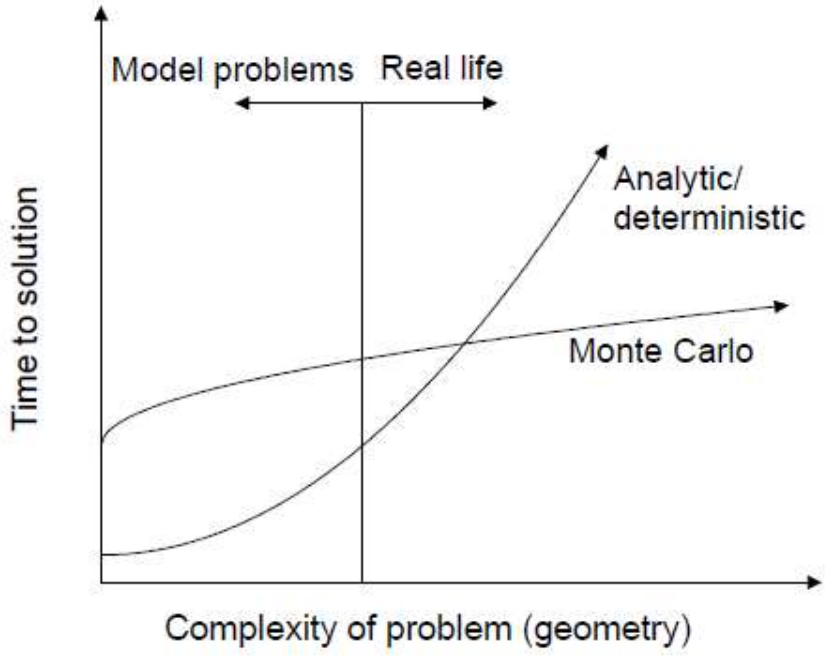

Figure 14 Comparison between MC and analytic/deterministic algorithms in terms of time to reach a solution vs. the complexity of a problem. From this graph it is evident that when complexity increases MC algorithms are faster [35].

In order to precisely simulate the radiation-matter interactions, Monte-Carlo Track Structure (MCTS) codes can be employed to provide accurate simulation of radiation transport and radiation chemistry, towards the in silico simulation of early biological damage [32, 36]. Several simulation platforms have been developed so far and are still being extended today by various groups: in 2019 thirty-two MCTS simulation codes existed, including the state-of-the-art PARTRAC and KURBUC codes, which are able to simulate direct and non-direct damage to DNA, including biological repair [37]: for example, PARTRAC is able to evaluate CAs simulating spatial distribution and complexity of DNA breakage, fragment diffusive motion and enzymatic process of NHEJ repair pathway [38]. Unfortunately, the majority of such codes are not open source, preventing their large-scale adoption and adaptability to various needs. The Geant4 MC simulation toolkit is an object-oriented and open source set of libraries, which is able to simulate particle physical interactions with matter using a rich variety of electromagnetic, hadronic and optical physics models [39]. Since 2007, Geant4 (release 9.1) is the only open access general-purpose radiation transport MC code offering, through its Geant4-DNA low-energy extension, track-structure capabilities in liquid water down to the eV energy range [40].

2.1. Geant4-DNA

Geant4-DNA is being developed by the "Geant4-DNA" Collaboration, which was officially created in 2008 [34]. Its aim is to develop an experimentally validated simulation platform for the modelling of IR-induced DNA damage, with the help of modern computing tools and techniques [41]. This is an ambitious work of highly interdisciplinary nature, encompassing several research fields and gathering experts from elementary particle physics, chemistry, biophysics, molecular and cellular biology, as well as IT scientists [41]. As mentioned above, Geant4-DNA is entirely included in Geant4 and can be used to simulate step by step physical interactions of particles, such as electrons, protons, neutral hydrogen, alpha particles including their charged states, and a few ions (lithium, beryllium, boron, carbon, nitrogen, oxygen, silicon, iron) down to very low energies (~10 eV) in liquid water and DNA constituents (Adenine, Thymine, Guanine, Cytosine, and backbone), thanks to a variety of physics models [37]. Figure 15 illustrates the verbosity of simulation in terms of very low-energy interaction at the nanometer scale of Geant4-DNA, compared to Geant4 standard physics. Liquid water has been historically the medium of choice in track-structure codes because of its abundance in cells (70–80% by weight) and specifically because of its role as a source of IR-generated reactive free radicals [37]. Geant4-DNA possesses a set of applications recreating different radiobiological phenomena that can be divided into four categories [42]: Physics, which includes "Clustering" to calculate the energy deposition with a dedicated clustering algorithm to assess DNA strand breaks in a simple liquid water geometry and "Dnaphysics" to extract physical information at the step[2] level; Chemistry, which comprises various examples to compute radiochemical yields; Geometry, which contains advanced applications to simulate complex geometry (realistic cellular structures, neurons…); Biological damage, which contains the latest releases, such as "MolecularDNA",

[2] In Geant4, the word "step" indicates an arbitrary virtual length along particle track, inside which the algorithm condenses all the interaction that occur for a single particle and returns the values of the simulation before and after the step. Geant4-DNA is able to simulate interaction using nanometer steps.

to simulate early direct and indirect DNA damage in absolutely realistic cell nucleus (still under revision [43]).

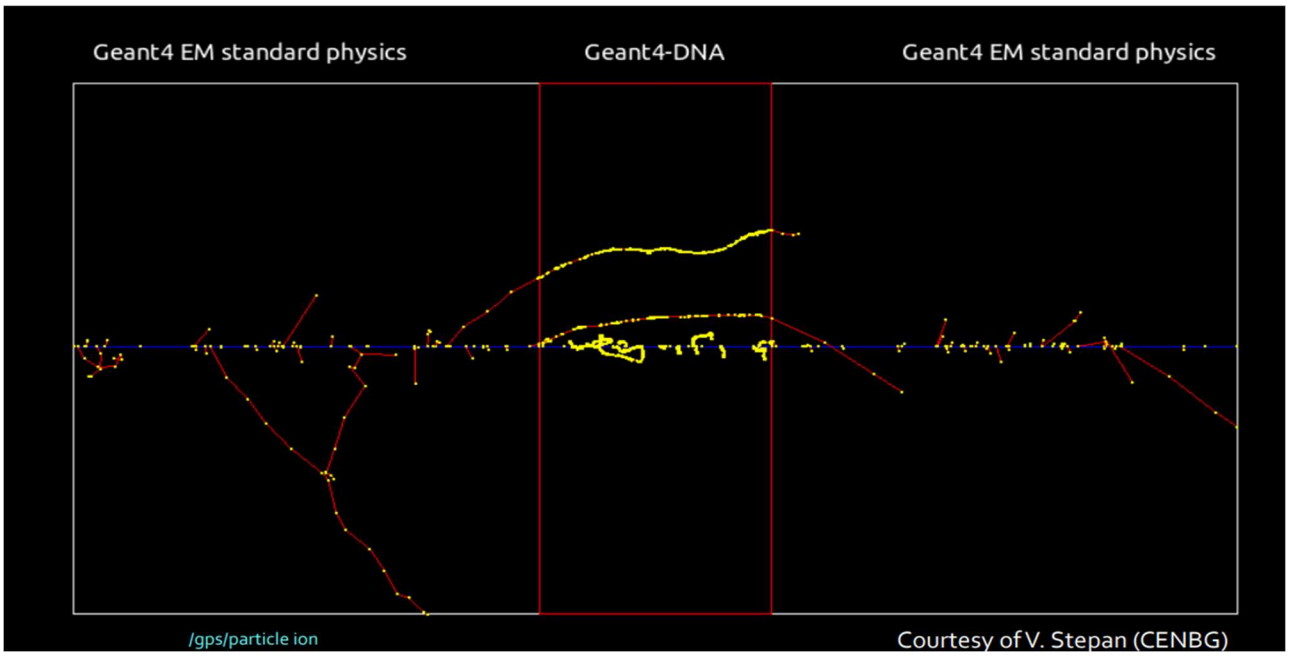

Figure 15 Comparison between Geant4 and Geant4-DNA physical interactions in microdosimetry applications [39].

Some of these applications, in particular in the Chemistry category and in the latest releases, also enable simulation of the physico-chemical and chemical stages[3] of water radiolysis in the irradiated medium up to 1 μs after irradiation, and benefits from the Geant4 ability to model geometries of various biological targets at the micrometer and nanometer scale [36]. Thus, there are two methods used to simulate DNA damage [44]: the first method is to estimate potential DSBs by superimposing DNA geometry to the radiation track structure, like in MolecularDNA application; the other is to use clustering algorithms based on probabilistic models to estimate DSB yield, as in the Clustering application. The first method is more direct, but it is also a time-demanding procedure. The second method leads to estimate with reasonable accuracy the yield of DNA DSBs and reduces the computational time. In conclusion, using the Geant4-DNA applications, DNA damage yields can be calculated and compared to values from literature to evaluate their accuracy and, eventually, validate them [12]. For instance, the MolecularDNA application was extended to allow the simulation of initial DNA damage in an *Escherichia coli* (E. coli) cell using a combination of straight and turned DNA segments that were joined together to mimic a fractal pattern[40]. The simulated results were validated against experimental data for plasmid DNA that had

[3] Exposure to IR produces effects over the cell at different stages, which in Geant4-DNA are categorized as: physical, physico-chemical, chemical and biological. The physical stage mainly consists of the deposition of energy to matter. This phase ends about 10^{-15} seconds after irradiation. After the physical stage, the physico-chemical stage begins and free radicals are created, extending in time to 10^{-12} s. The chemical phase follows and, as the name indicates, it is when the chemical reactions and dielectric relaxations occur and lasts until 10^{-3} seconds past exposure. During this phase, DNA damage begins to form (*fixation*). The biological phase occurs within longer time scales like minutes and it may last weeks or years (as is in the case of IR-induced cancers).

been irradiated by both electrons (10 keV) and protons (90–249 MeV). The geometrical model was further improved in the study of Sakata et al. [36] to build a human cell nucleus that was composed of fractally distributed chromatin fibres and to include biological repair models. They introduced a semi-empirical model to predict the foci accumulation yield with time, up to 25 h after irradiation: the repair model computes the yields of accumulated repair proteins and describes the decrease of DSB level due to the action of repair pathways employing a differential equation, hence DSBs kinetics can be calculated using the number of complex DSB and of simple DSB as input. The damage parameters were re-adjusted within a reasonable range to achieve agreement with experimental data for proton irradiation in a human cell [36].
The next paragraph describes an overview of the Clustering application as used in this work.

2.2. The Clustering application in Geant4-DNA

The clustering application of Geant4-DNA simulates particle tracks in liquid water and allows the assessment of DNA damage by their energy depositions [45]. The application name derives from the use of a specific clustering algorithm in order to classify the (severity of) DNA lesions. Clustering algorithms are a class of algorithms widely used for data mining in several domains, especially in those where the results consist of large databases. Given a dataset, they can reveal the points or objects belonging to the same group, meant as objects that have the similar characteristics or points that are spatially close to each other, and show the links between them [46]. In this thesis it was used the provided Geant4-DNA application derived from an adaptation of the "Density-Based Spatial Clustering of Applications with Noise" (DBSCAN) algorithm to early-stage DNA damage clustering calculations, as performed by Francis et al. in 2010 [46]. DBSCAN is a density-based clustering algorithm[4] designed to discover clusters of arbitrary shapes. Figure 16 shows a flowchart of the program used for damage clustering.

[4] In density-based clustering algorithms, clusters are identified as areas of higher density than the rest of the dataset: given a set of points in some space, the algorithm groups together points that are closely packed together (points with many neighbours), marking as outliers points that lie alone in low-density regions (whose nearest neighbours are too far away) [68].

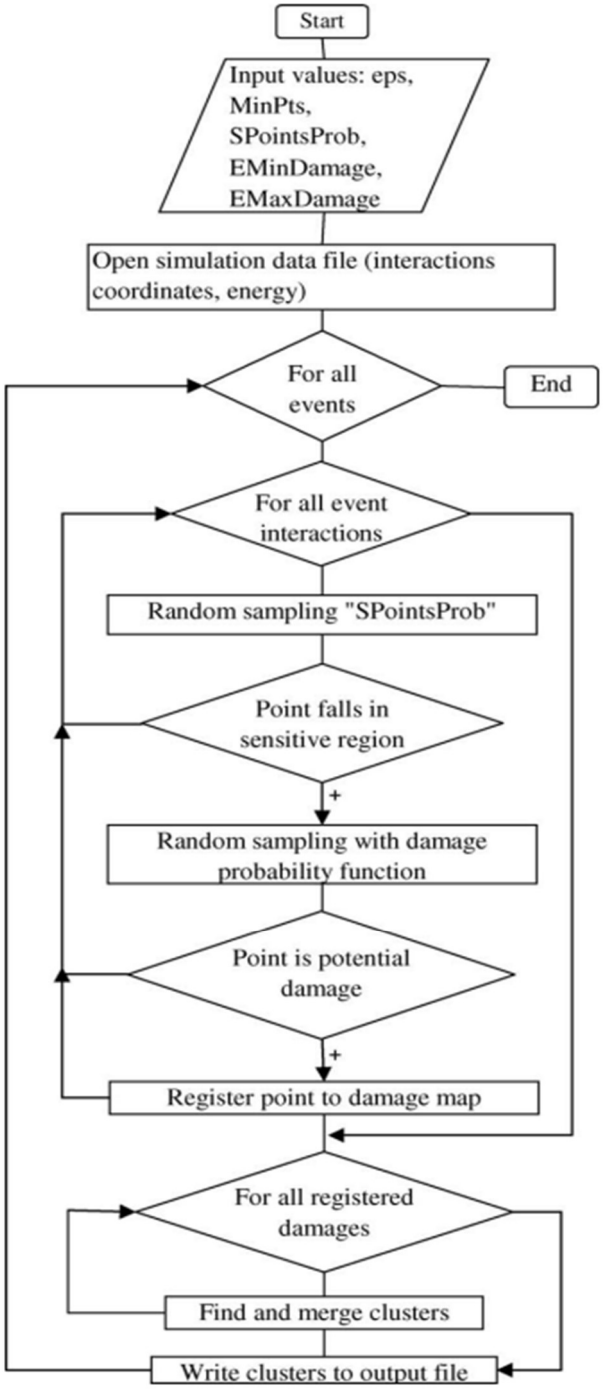

Figure 16 Flowchart of the program used for damage clustering where *eps* is the cluster reachability radius, *MinPts* the minimum number of points required to form a cluster, *SPointsProb* the probability that a point falls in a sensitive area; *EMinDamage* and *EMaxDamage* are the energy limits corresponding, respectively, to probabilities 0 and 1 for the damage induction function, which is linear.

The input parameters given by the user are: neighbourhood radius of a point (eps), the probability that a point falls in a sensitive area (SPointsProb) where it can directly or indirectly[5] reach the DNA, minimum points per cluster (MinPts) and the energy constraints

[5] Indirect damage is caused by free radicals from water radiolysis produced in the vicinity of a DNA region.

(EMinDamage and EMaxDamage) for which the damage induction function varies linearly between 0 and 1.
For every event and for every interaction, a random sampling is done using SpointsProb and a linear damage induction function. If the interaction falls in the sensitive area and passes the damage induction sampling, it is considered as a SSB positioned randomly on one of the two DNA strands. Actually, the damage induction caused by relatively small energy deposits, that is the energy lost by the particle whose track is being followed, (<5eV) is still an open question, since theoretically these energy deposits do not correspond to ionising collisions but only to different excitation modes [46]. Hence, so far there is no clear evidence of the effect of such low-energy deposits on DNA strands. For this reason, the algorithm takes zero as damage probability for energies below 5 eV increasing linearly up to 37.5 eV. After the formation of the SSBs, the DBSCAN algorithm runs over all the points testing the distances between each pair of SSBs. For every SSB, if the number of its neighbouring damages, located within the radius eps, exceeds the MinPts value, there is the formation of a cluster and the location of the cluster is its centre. Two parameters are needed by the algorithm at this stage: MinPts, which is equal to 2 (actually, we can have DSBs with a minimum of 2 points and the maximum radius to form a cluster), and radius eps. In radiobiology two SSBs are regarded as a DSB if they are separated by less than 10 base pairs, the corresponding distance being estimated to be ~3.2 nm [46], thus radius eps is usually set to 3.2 nm. The points that do not belong to any of the formed clusters are considered as simple SSBs. Clusters containing two or more SSBs where at least one SSB is located on an opposite strand are considered as DSBs. Neighbouring clusters can merge together and are considered as one single cluster if the centre points are within the maximum limit distance (i.e., 3.2 nm). This clustering algorithm was adapted for Geant4-DNA application from Y. Perrot, H. Payno (Laboratoire de Physique Corpusculaire de Clermont-Ferrand, CNRS/IN2P3 - Clermont University, France). To this purpose, specific classes were added to default Geant4 classes in this application: ClusteringAlgo, ClusteringAlgoMessenger, ClusterSBPoints, CommandLineParser, RunInitObserver, SBPoint. More details about all the classes can be found in the next chapter. The geometry set-up was the same proposed by Francis et al.[46], which consists in a World volume containing a Target box made of liquid water of 1µm x 1µm x 0.5 µm. In Figure 17 it is shown the default simulation aspect for Geant4-DNA clustering application. The general output results consist of a clusters_output.root file, containing for each event:

* the number of SSBs (SSB);
* the number of complex SSBs (SSBcomplex);
* the number of DSBs (DSB);
* the cluster size distribution;
* the absorbed dose in the Target.

A part of this thesis work is the DNA damage modelling caused by BNCT using the Clustering application, appropriately adapted to simulate BNCT mixed field. A detailed description of the geometry and the source used can be found in the next chapter.

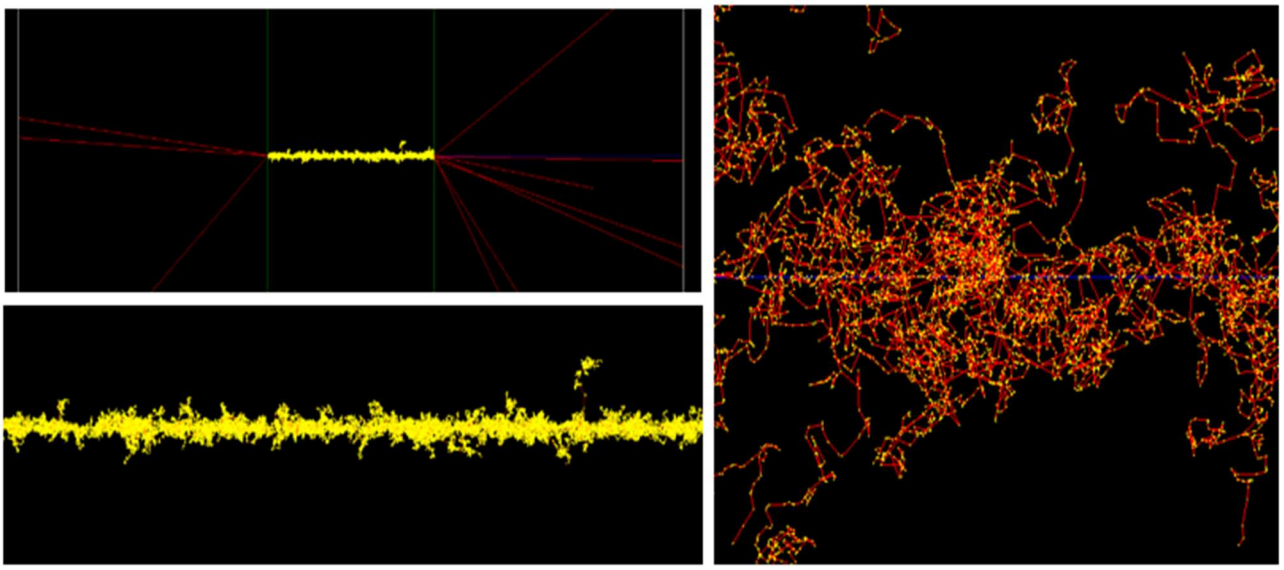

Figure 17 Default simulation aspect for Geant4-DNA clustering application shooting one alpha-particle. The pictures on the right and the one at bottom on the left are obtained by zooming in the energy deposition track showing the level of detail of the simulation.

3. Materials and methods

In this chapter, the cell culture maintenance, the boron treatment, the irradiation setup, the used assays and the simulation parameters are illustrated.

3.1. Experimental setup

The experimental activity of the work described in this thesis took place at the Radiation Biophysics Laboratory of the Physics Department "E. Pancini", University Federico II of Naples and at the Laboratory of Experimental Surgery, Department of Clinical-Surgical Sciences, Polo Cravino, University of Pavia, and aimed at evaluating the DNA damage caused by BNCT by an in vitro study of repair efficiency kinetics and chromosomal aberration (CA) induction.

3.1.1. Cell culture maintenance

Human epithelial mammary MCF10A cells were used. This is a non-tumorigenic breast epithelial cell line, frequently used in DNA damage studies because of its relatively stable genome. It was kindly provided by Dr. P. Chaudhary, School of Medicine, Dentistry and Biomedical Sciences, Queen's University Belfast, UK [47]. The cells required two DMEM/F12-based media[48]: one for optimal growth, containing 5% horse serum, Endothelial Growth Factor or EGF (20 ng/ml), hydrocortisone (0.5 mg/ml), insulin (10mg/ml) and cholera toxin (100 ng/ml); the other one was used during routine subcultivation and is devoid of all supplements but serum enriched (20% horse serum) to quench the action of trypsin during cell resuspension and counting dilutions. Penicillin/streptomycin was added to both media (1%). The cells were grown in standard tissue culture flasks kept in a humidified atmosphere of 5% CO_2 in air at 37°C.

3.1.2. Boron compound treatment for BNCT irradiations

Before neutron irradiation the cells were treated for 4 hours with BPA previously weighed out and thoroughly dissolved in the appropriate volume of cell growth culture medium (more information in Appendix 1). The treatment concentration was 80 μg of ^{10}B per ml of culture medium (that is, 80 parts per million, ppm), which corresponds to approximately 1.67 mg/ml of BPA [49]. Subsequently, the BPA-containing medium was removed before irradiation and, after three washes with PBS[6], was replaced with medium devoid of BPA.

3.1.3. DNA damage assays

The three radiobiological assays used to quantify radiation-induced DNA damage are: the Ionizing Radiation-Induced Foci (IRIF) Assay, the Whole Chromosome Painting of chromosomes 1 and 2 (WCP) and the Multicolour Fluorescence In Situ Hybridization (mFISH) technique, performed at the Radiation Biophysics Laboratory, Physics Department, University of Naples Federico II. Detailed protocols can be found in Appendix

[6] Phosphate Buffered Saline solution.

1. The same setup was adopted for all performed experiments: two experiments of neutron irradiation in Pavia and two of photon irradiation at University Federico II (one for FISH assays and one for Foci Assay). Cells were seeded 24h before each irradiation on coverslips placed in a multiwell plate for Foci Assay (Figure 18) or about 48 h before exposure in T25 flasks for FISH assays (Figure 19) at appropriate densities. Control cells were also subjected to the same process and timing, except, of course, for radiation. For FISH assays chromosomes were harvested around 36h after irradiation, whereas to study DDR dynamics cell fixation for Foci Assay was performed at several time points (30', 2h, 3h, 5h, 24h).

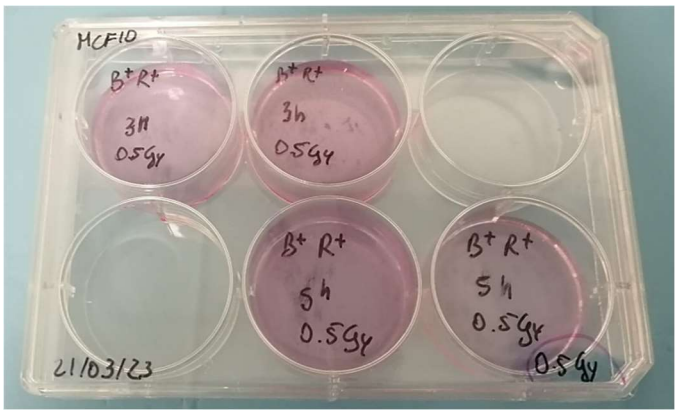

Figure 18 The cells for Foci assay were seeded on coverslips placed in a multiwell. In the picture are shown four samples at 0.5Gy (BNCT nominal dose) fixed at 3h post irradiation (top) and after 5h from irradiation (bottom).

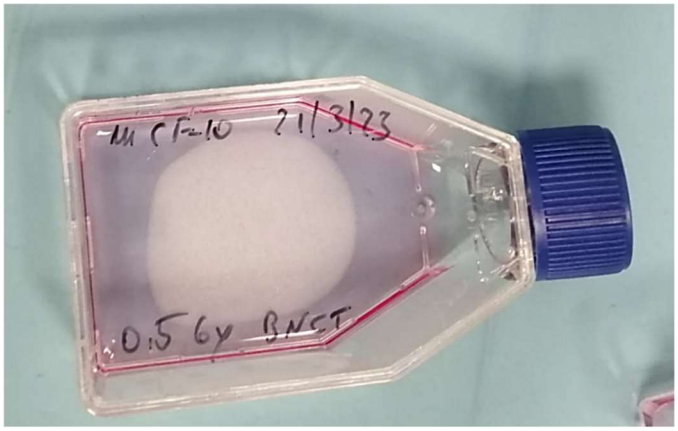

Figure 19 Picture of a T25 flask with MCF10A cells irradiated at 0.5Gy (BNCT nominal dose).

3.2. Irradiations

Neutron irradiation for BNCT was performed using the thermal column of the Pavia University TRIGA Mark reactor. Photon irradiations took place in Naples at the Radiation Biophysics Laboratory of the Physics Department, University Federico II by means of a high-voltage radiogen tube.

3.2.1. Neutron irradiation

The cellular samples were irradiated at the TRIGA Mark II research reactor (University of Pavia, Figure 20). An irradiation facility was constructed inside the thermal column of the

reactor to produce a sufficient thermal neutron flux with low epithermal and fast neutron components, and low gamma dose [50]. Cells were irradiated in a position of the facility where the thermal neutron flux is about 8 x 10^7 cm^{-2} s^{-1} at 1kW. It is important to note that the flux scales linearly with the power.

Figure 20 TRIGA MARK II research reactor, University of Pavia.

MCF-10 cells were irradiated with nominal doses of 0.5 and 2 Gy, exposing the multiwell plates or T25 flasks to 5kW and 20kW neutrons for 10 min, respectively. Nominal doses were estimated assuming 30 ppm of boron in cells and using the reaction rate previously determined by MCNP simulations as reported in in Table 1. Information about geometrical parameters of MCF10A cells, also used in simulations at [51]. Thus, the final dose is calculated as the sum of the product of reaction rate factor and irradiation time, reactor power and only for Boron component ppm of ^{10}B [52].

Table 1 Reactions rates to evaluate absorbed dose in cells calculated by simulations. Each reactions rate was established normalizing for the time, the power of reactor and the weight of cells.

Reactions rate (s^{-1} g^{-1} normalized for 1kW)	
Boron component per ppm of ^{10}B	1.56E+04
Nitrogen component (600 keV protons)	1.22E+05
Scattering component (variable energy protons)	1.79E+08
Gamma component (2.2 MeV photons)	1.35E+06

3.2.2.X-ray irradiation

The X-ray irradiation was carried out using a STABILIPAN 2 (Siemens) radiogen machine consisting of a Thomson X-ray tube (TR 300F), operating at 250 kV_p with a 1-mm Cu filter, available at the Radiation Biophysics Laboratory. The dose rate was approximately 1.37 Gy min^{-1} (previously determined with an Accu-Pro Radcal® ionization chamber).

3.3. Measurement of boron uptake in cells

The methods used by the BNCT group at Physics Department of Pavia University for measurement of actual boron intracellular uptake is neutron autoradiography[7] using Solid-State Nuclear Track Detectors (SSNTDs), that is allyl diglycol carbonate($C_{12}H_{18}O_7$), known commonly as CR39 (Columbia Resin [53]). This method allows obtaining images of boron distributions in cells and quantifying its concentration [50]. Boron concentration was measured for each experiment in samples treated the same day and undergoing the same procedure as the ones irradiated for radiobiological assays. Generally, boron naturally present in cells is also measured; in fact, control samples are usually prepared, and included in the dose calculation for the beam-only component. The cellular pellet[8] was gently deposited on Mylar films and let dry out for at least 48h (Figure 21). Control samples are routinely prepared to evaluate possible contamination.

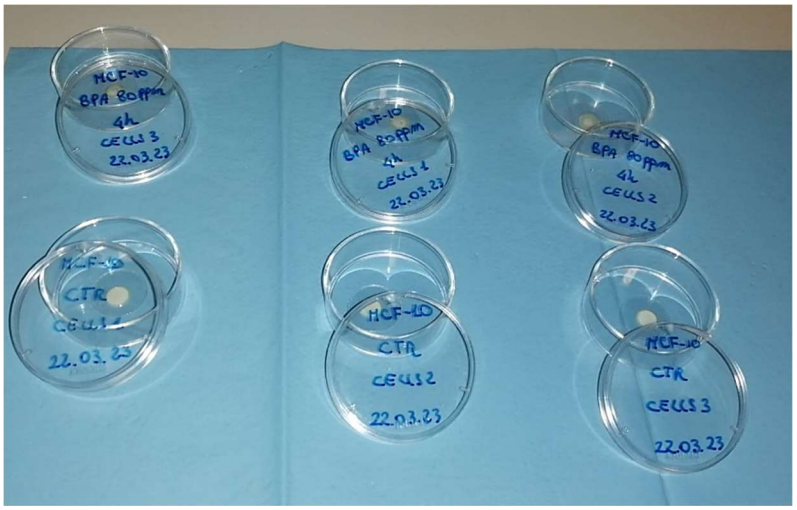

Figure 21 Petri dishes containing Mylar films on which MCF10A cells were grown, prepared for the evaluation of boron incorporation. At the top there are three samples treated with BPA and at the bottom the same number of control samples (not treated with BPA).

The films on CR39 were irradiated at the TRIGA reactor at 20kW for 30', in a position of the facility where the thermal neutron flux is 8 x 10^6 cm^{-2} s^{-1} at 1kW.
The charged particles originated from neutron capture in boron and nitrogen present in the samples produced latent tracks in the CR39 detectors. After irradiation, the CR39 were subjected to chemically etching in a PEW409 (KOH +C_2H_5OH + H_2O) basic solution for 10 min at a temperature of 70°C. This procedure increases the diameter of the latent tracks, which become visible under microscope observation. For these experiments a Leica stereomicroscope, provided with an integrated camera connected to a PC, was used. The images were acquired and analysed with Image Pro Plus 7.0.8. Once the acquisition process is concluded, Image Pro Plus allows performing some operations on the picture (Figure 22). Thus, images were processed and a dedicated C++ software was used to count the tracks in

[7] Neutron autoradiography is a nuclear analysis technique that can be used to measure the boron concentration in biological samples. It is based on the detection of tracks left by alpha particles and ^{7}Li ions on CR39 detectors, following neutron irradiation in the presence of ^{10}B. The chemical damage produced by the particles on these polymers is of the order of nanometers and become visible after chemical etching. Once etched, the track can be in fact visualized and counted using an optical microscope and suitable software.
[8] Cellular pellet: a mass of cells obtained by centrifugation of a cell culture.
[9] PEW40 is formed by 15% of KOH, 40% of C2HeO and 45% of pure water, where the percentage represents the mass per cent.

each image. Using a previously obtained calibration curve, expressed as density of tracks [tracks/mm^2] versus boron concentration in ppm, it was possible to trace back the boron concentration in the cellular pellet [50].

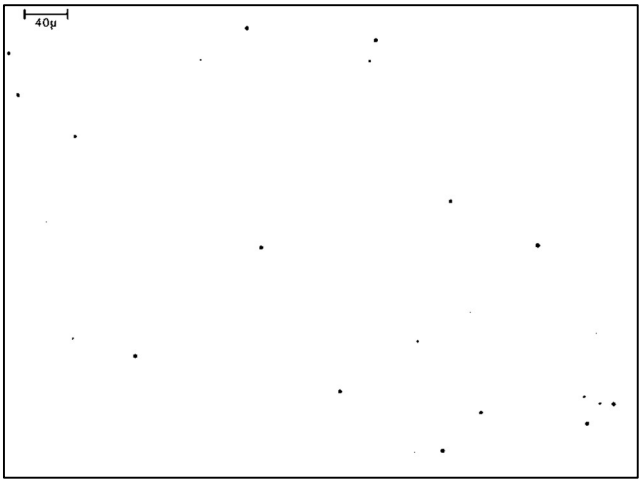

Figure 22 Filtered picture to count tracks on CR39.

3.4. Measurement of radiation-induced DNA damage

In the next paragraphs, the experimental methods employed in the three biological assays performed in this thesis to assess radiation-induced DNA damage are illustrated.

3.4.1. Foci Assay

As previously mentioned, the Foci Assay allows determining the repair kinetics after irradiation by co-localization of fluorescence intensity signals (foci) related to early repair events elicited by radiation-induced DNA breakage, specifically histone γH2AX phosphorylation and 53BP1 protein recruitment. After irradiation cells were fixed with 4% paraformaldehyde for 15 minutes at specific time points, then they were immunolabelled with suitable fluorophores, specific for γH2AX and 53BP1 proteins, while DAPI (4',6-diamidin-2-phenyl a fluorescent organic dye that strongly binds DNA regions rich in A-T sequences) was used for counterstaining the nuclear region in which radiation-induced foci are located. A detailed protocol can be found in Appendix 1. The timepoints chosen to study BNCT repair kinetics were 0.5h, 2h, 3h, 5h and 24h after irradiation; for X-ray experiments 0.5h and 24h time points sufficed because the repair kinetics after low-LET radiation is already well characterized (Figure 10). It is important to note that as neutron irradiation lasted 10 minutes, the first time point is calculated starting from the beginning of irradiation. Also, because of the experimental handling of the samples at the reactor and the distance between the latter and the cell culture laboratory, only after 2 hours cells were placed back in incubator. Given that X-ray irradiation lasted few minutes and the radiogen machine was very close to the Radiation Biophysics cell culture laboratory, the samples returned to physiological conditions (37°C and 5% CO_2) in a shorter time.
Slide analysis was carried out at the Radiation Biophysics Laboratory at University of Naples Federico II, using a fluorescence microscope (Imager 1, Zeiss, Germany) connected to a computer equipped with the Metafer software (Metasystem, Germany) for automated image acquisition; suitable filters allow to excite and observe the light emitted by the three types of

fluorophores used, visible in the frequencies of blue (DAPI), red (γH2AX) and green (53BP1) light, respectively. In line with the literature, foci exhibited variable sizes, at times merging into co-localized fluorescent spots (Figure 23).

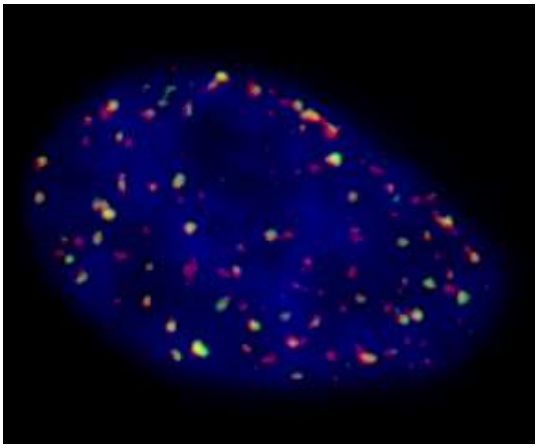

Figure 23 Example of the final image returned by Metafer software for a cell irradiated at 2Gy and fixed at 5 hours; nucleus appears in blue, γH2AX foci in red and 53BP1 foci in green.

For the statistical analysis, the average number of foci per cell, in each experiment, was calculated for each sample as the ratio between the sum of the number n of foci counted and the number N of cells in the sample:

Equation 1

$$f = Average\ number\ of\ foci\ per\ cell = \frac{n}{N}$$

The errors are calculated assuming a binomial distribution:

$$\sigma_{average\ numer\ of\ foci\ per\ cell} = \sqrt{\frac{f * |f-1|}{N}}$$

The estimation of the average size of the foci was made, for each sample scanned at the microscope, using MATLAB algorithm, through the ratio between the total area given by the sum of the areas of the foci measured in pixels, and the total number n of the foci counted, that is:

Equation 2

$$\boldsymbol{A = Average\ area\ of\ foci\ per\ cell = \frac{Total\ area}{n}}$$

And the corresponding errors were obtained as:

$$\sigma_{average\ area\ of\ foci\ per\ cell} = \sqrt{\frac{A * |A-1|}{N}}$$

The final results are a weighted average between the two experiments, both for the number of foci and the area:

Equation 3

$$F = \frac{\sum w_i * f}{\sum w_i}$$

where:

$$wi = \frac{1}{\sigma_i^2}$$

And the error is:

$$\sigma_F = \sqrt{\frac{1}{\sum w_i}}$$

3.4.1.1. Image acquisition and processing by the Metafer software

The Metafer software allows automating different procedures in the field of image analysis related to cytogenetic preparations, since it can be adapted to the type of operation by optimizing an appropriate classifier, that is a set of parameters that the software uses to analyse the captured images. In this thesis, a previously optimized classifier for the detection of colocalized foci was used. The image acquisition of the nuclear foci takes place in two distinct phases: firstly, the slide is scanned with a low-magnification (10x) objective using only the DAPI emission filter (blue), which allows to identify the region of interest on the slide that is the foci-containing nuclei; the second stage consists of a high-magnification scan with a 63x oil-immersion objective of different focal planes, in order to acquire signals from the foci present in each individual previously detected nucleus in RGB (red, green, blue) channels. Final images (Figure 19) are obtained as reconstructed stacks of 10 focal plane spaced by steps of 0.75 μm. At the end of the scan, Metafer creates a gallery for the images of the single nuclei acquired, an example of which is presented in Figure 24. The software is able to detect foci in cell nuclei, count them, and collect data on their frequency; however, it provides information only about individual and colocalized foci counts, without giving information about their size. To obtain this information another algorithm implemented in MATLAB was used (see Appendix 2 for details).

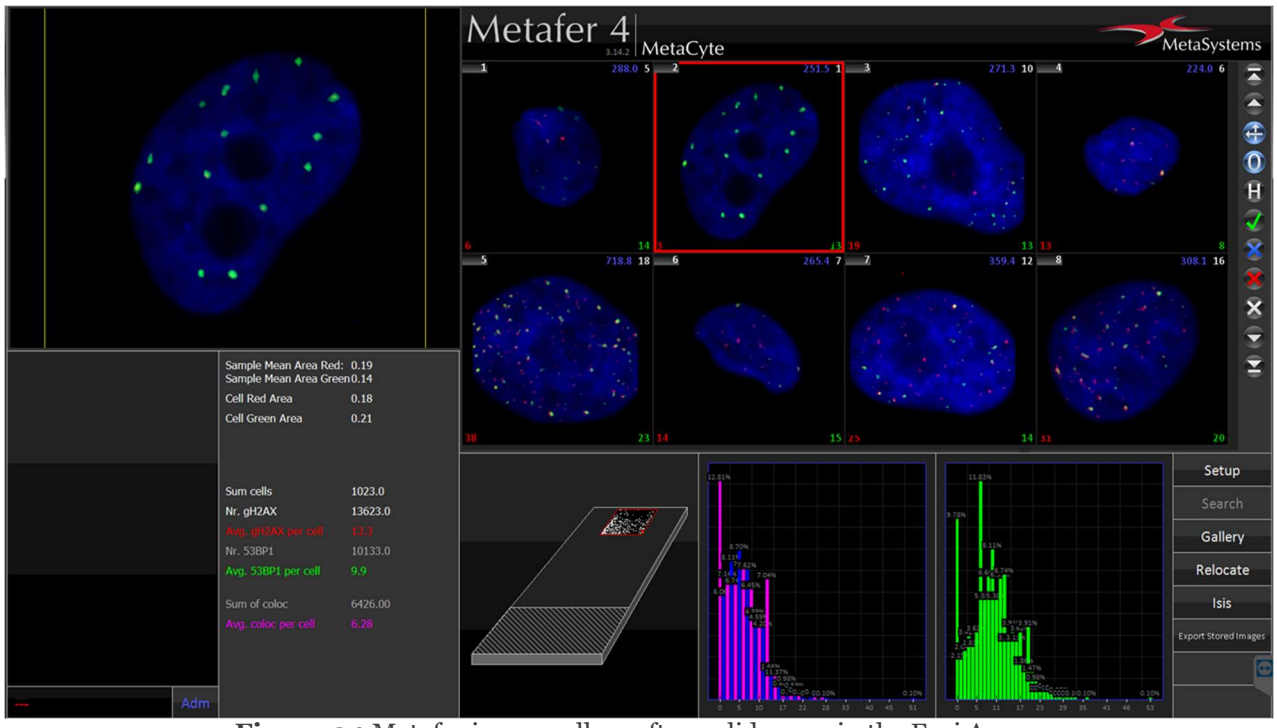

Figure 24 Metafer image gallery after a slide scan in the Foci Assay.

3.4.1.2.The use of MATLAB for foci counting

MATLAB (an abbreviation of "MATrix LABoratory") is a proprietary multi-paradigm programming language and numeric computing environment developed by MathWorks. MATLAB allows matrix manipulations, plotting of functions and data, implementation of algorithms, creation of user interfaces, and interfacing with programs written in other languages. Although MATLAB is intended primarily for numeric computing, optional toolboxes can be uploaded to add specific functionalities, like functions for image processing. MATLAB's Image Processing Toolbox (MIPT) allows the visualization, modification, analysis and processing of the most common image formats (in this case, .TIFF). For this thesis' aim, the images of the cells were exported from the Metafer gallery and analysed with an implemented MATLAB algorithm (see Appendix 2). The algorithm can automatically count the foci, either single-protein foci or colocalized foci, and provides an estimation of the average area of the spots (in terms of number of pixels). Indeed, the determination of what is considered or not as a focus during manual counting is still left to the judgment of the scorer, whereas an automatic software guarantees a greater objectivity of the analysis.
As previously mentioned, colocalization between the two signals is believed to reinforce the hypothesis that the labelled foci correspond to genuine radiation-induced DSBs rather than the result of metabolic processes[14]. Manual counting was performed for each slide by independent scoring of 50 cells by two different operators (100 cells/total slide) using Metafer images. The first step of the algorithm consists in opening the RGB image previously acquired with the Metafer software (Figure 23) and separate the three-color channels (nucleus in blue thanks to the counterdye DAPI, γH2AX foci in red and 53BP1 foci in green) obtaining three images in grayscale as shown in in Figure 25.

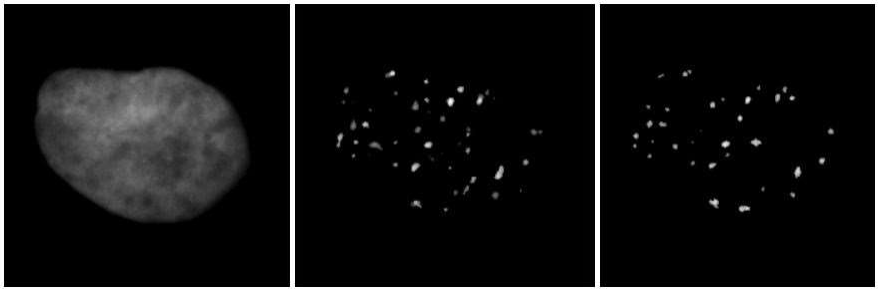

Figure 25 Grayscale images obtained from splitting Metafer images using MATLAB algorithm. Nucleus on left, γH2AX foci in the center and 53BP1 foci on right.

On each channel (R-G-B) is applied a median filter. The images are then binarized using an adaptive threshold in the various areas of the image and filled "holes" within the circular regions. Hence, the regions of interest will have a pixel value set to 1 and the rest to zero. In addition, pixels of too low intensity compared to others are set to zero by choosing the threshold parameters (Table 3). With some segmentation tools it is possible to count the simply connected regions in the images (nucleus and foci relative to the two markers) and eventually to separate two contiguous nuclei with the command "watershed". The binary image of the nucleus is then multiplied by those in the red and green channel obtaining in output two images (one from the red channel, and one from the green channel) containing in white (pixel value 1) only the foci inside the nucleus. Possible spurious signals external to the nucleus appearing in the red or green channels are set to zero by the operation of multiplication. To count colocalized signals, red and green masks are multiplied to get an image with only the colocalized foci in white (Figure 26). At this point, objects are counted for each cell and the output consists of the average number of foci per cell and the average spot areas.

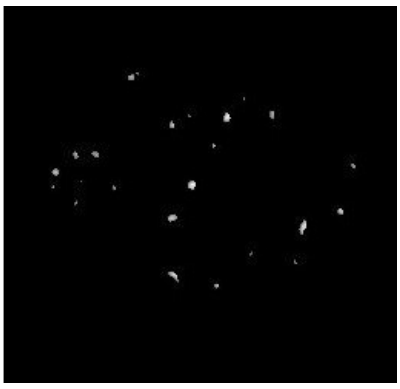

Figure 26 Processed image output on which the simply connected regions (foci) are counted.

The algorithm was first tested on some trial sample in order to increase the agreement between manual and MATLAB counting; the parameters that can be modified to this purpose are:

* Parameter_WS that allows to divide two contiguous nuclei;
* Parameter_pixel deletes object smaller than the parameter itself;
* Perc_soglia_intensità is the percentage of the maximum pixel value image, in terms of intensity, that represents the threshold on intensity to distinguish foci or nucleus to noise.

The results of the optimization can be found in chapter 4.

3.4.2. FISH Assays

Detection of structural CAs was carried out by Fluorescence In Situ Hybridization (FISH) techniques: Whole Chromosome Painting (WCP) and multicolor (m)-FISH. The choice to use non-cancer human mammary epithelial MCF-10A cells was done in order to avoid the confoundingly high baseline CA frequency from genomically unstable cancer cells. For WCP, two pairs of homologous chromosomes were labelled with probes (MetaSystems, Germany) directed to chromosomes 1 and 2 emitting in the green (chromosome #1, XCP-1 FITC conjugated probe) or red (chromosome # 2, XCP-2 orange) spectrum under UV light. In this case, the labelling scheme is very simple: green for chromosomes 1 and red for chromosomes 2. m-FISH is a 24-color karyotyping technique that allows to accurately measure the induction of chromosomal arrangements, resulting from erroneous repair of IR-induced DSBs. In particular, it is possible to accurately quantify complex exchanges, a known biomarker of clustered damage that, in this case, is caused by the high-LET particles generated by the neutron capture reaction. Firstly, the techniques consist of labelling the chromosomes, only 1 and 2 for WCP and all chromosomes for mFISH, harvested according to the procedure described in Appendix 1, with a finite number of spectrally distinct fluorophores, in a combinatorial fashion for mFISH [54]. The 24 X-Cyte (Metasystems) kit was used for mFISH and consists of a cocktail of five fluorophores (CyTM5, DEAC, FITC, Spectrum OrangeTM, Texas Red), where each of them uses a nucleotide sequence complementary to a specific DNA portion, such that each chromosome is uniquely labelled entirely down its whole length with one, two, or three different fluorophores. In Figure 27 the labelling scheme is shown for all the chromosomes.

Figure 27 Metasystems mFISH labelling scheme [55].

MCF-10A cells were treated at 36 h post irradiation by chemical induction of Premature Chromosome Condensation[10] (PCC). PCC was obtained following 30-min incubation in calyculin A. After aging of slides and XCP or 24XCyte probe cocktail denaturation, hybridization was performed using the programmable HyBrite chamber system. After post-hybridization washes, chromosomes were counterstained by DAPI. The detailed protocols can be found in Appendix 1. The second step is the microscopic visualization and digital acquisition of each fluorophore to classify each chromosome in accordance with the labelling scheme. The third step involves the detailed analysis of these digitally acquired and processed images, directly for WCP and using ISIS software for mFISH that allows the reconstruction of karyotype to resolve structural aberrations. The last two steps will be illustrated in more detail in the next paragraphs.
All types of structural aberrations were scored separately and categorized in simple exchanges (i.e. translocations and dicentrics), either visibly structurally complete or incomplete, acentric excess fragments and complex exchanges, these being assessed as the result of an exchange involving not less than three breaks in at least two chromosomes (that is, the above-mentioned CAB criterion) [27]. When more than one option to achieve completeness was possible, the rearrangement that produced the minimum CAB was used.
For the purpose of this study, the frequency of all chromosome exchanges was calculated as the ratio between all exchange-type aberrations "n" (simple plus complex, both reciprocal and nonreciprocal) and the number of cells scored "N" (at least 100 cells for mFISH and 400 for WCP) as in Equation 4:

Equation 4

$$f = Average\ number\ of\ aberration = \frac{n}{N}$$

The errors were calculated assuming binomial distribution:

$$\sigma_{average\ numer\ of\ aberration\ per\ cell} = \sqrt{\frac{f * |f - 1|}{N}}$$

The same formulas were used to calculate the frequency of complex aberrations alone, the frequency of rings and the number of chromosomes and breaks involved in complex exchanges per total number of scored cells in order to unveil the degree of complexity in the chromosomal rearrangements as in [47].

3.4.2.1.Image acquisition

Image acquisition was carried out at the Radiation Biophysics at University of Naples Federico II with a fluorescence microscope (Imager 1, Zeiss, Germany) connected to a computer equipped with the Metafer software (MetaSystem, Germany) and six different fluorescence filters. The acquisition of the images takes place in two distinct phases. A first

[10] Premature Chromosome Condensation (PCC) is a technique that causes the induction of chromosome condensation in cells that are not in metaphase, like in G1 and in G2 phases but not in S phase, in order to increase the number of cells that can be analysed. In fact, if only cells properly in metaphase are analysed, these would constitute a small sample because the metaphase lasts about 1-2 h on a cycle of about 24h. Moreover, in the case of high-LET exposure, cell-cycle checkpoints would block heavily damaged cells, thus analysis of mitotic chromosomes would likely cause an underestimation of IR-induced damage. PCC is carried out using a substance called calyculin A.

automatic search of the slide is carried out using a low-magnification (10x) objective to locate the PCC positions across a selected area of the slide. After such automatic search, the PCC are manually selected to discard those that do not meet scoring quality criteria (e.g., poor hybridization signal, fuzziness, aneuploidy, etc.) (Figure 28).

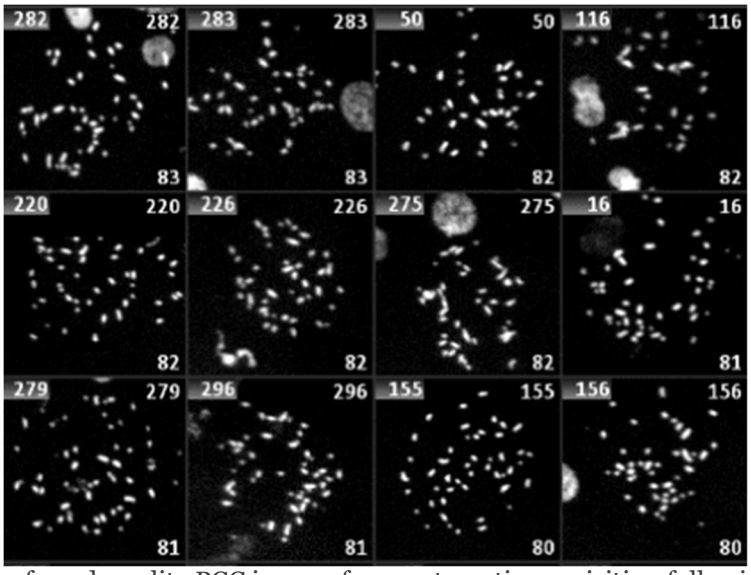

Figure 28 Example of good-quality PCC images from automatic acquisition following manual selection.

The second, much longer phase uses a 63X oil immersion objective for mFISH and a 40X oil immersion objective for WCP: the acquisition starts from the memorized position of the individual PCC and the software captures grey scale images of each fluorochrome by automatically changing the six filters (or only two for WCP) corresponding to each fluorochrome. The acquired images of the individual fluorescence channel are then processed according to a well-defined classifier and combined to produce a single "pseudo-colored" image of the chromosomes, as in Figure 29. Then, mFISH images will have to be analysed using the “ISIS” software for karyotype reconstruction, while WCP images can be stored and analysed directly. mFISH was expected to allow a better evaluation of the yield of complex chromosomal rearrangements.

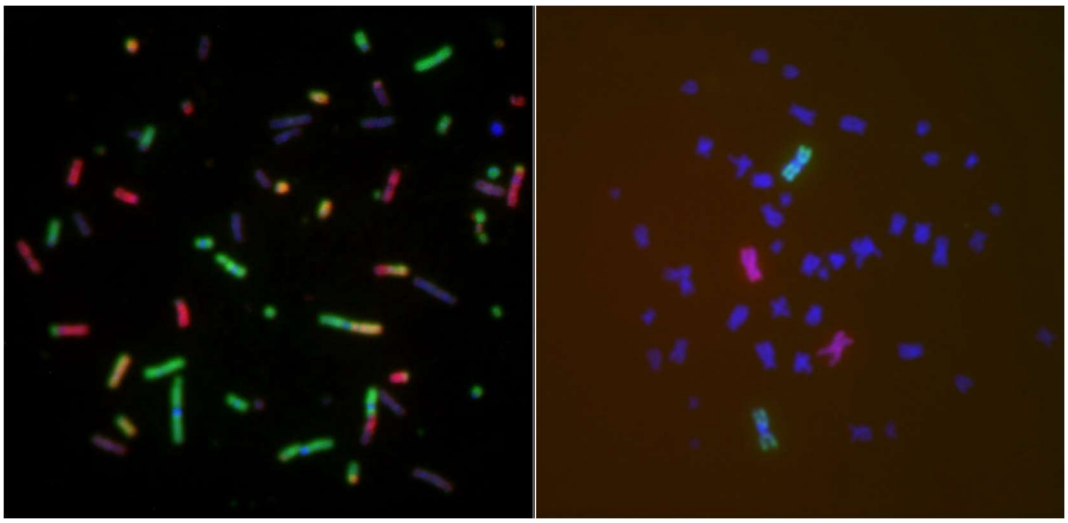

Figure 29 Example of “pseudo-colored” image of a single metaphase for mFISH assay (left) and for WCP assay (right).

3.4.2.2. Karyotyping by the software ISIS

The reconstruction of the karyotype was carried out manually with the aid of a program part of the Metafer suite, named ISIS. By analysing the colour ratios of all pixels, ISIS unambiguously assigns any region of the image to the respective chromosome class and each chromosome class will be displayed in a unique colour. Hence, ISIS makes possible to visualize and to discern CAs based on the images, taking into account size and shape of the chromosomes. The pseudo-coloured images available are processed through a series of tools that improve the image quality: selection of the metaphase elements to be analysed and precise separation of overlapped elements (Figure 30), background correction, reduction of background noise using specific threshold and optimal overlap of the captures of individual filters.

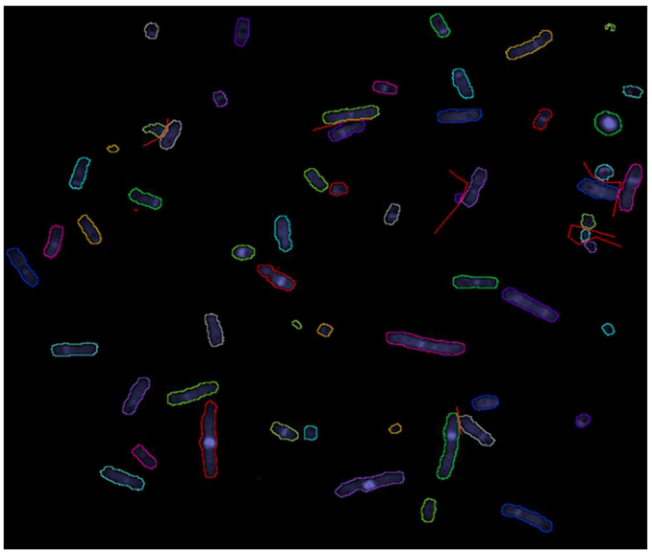

Figure 30 Example of image during post-processing operations: phase of separation of overlapped chromosomes visualizing only DAPI staining.

Chromosome classification is either done based on DAPI staining or by using the fluorochrome combinations. No centromere probe was used but centromeres were clearly distinguishable as bright bands under DAPI illumination. In order to facilitate the analysis, mFISH chromosomes can be displayed in three different pseudo-colour display modes: maximum saturation (solid colour, Figure 31), DAPI image overlaid with the pseudo-colour, and standard pseudo-colour image like in Figure 29.

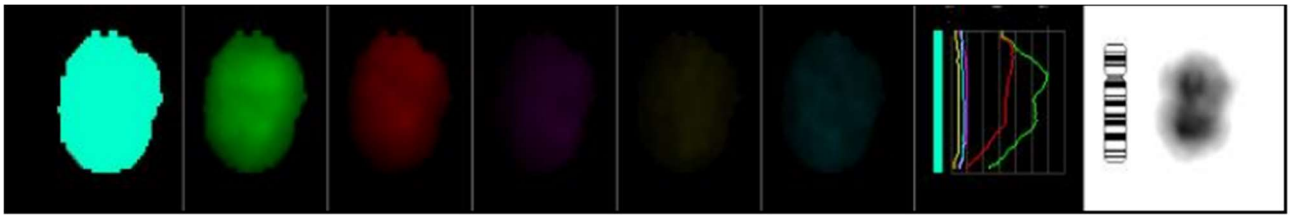

Figure 31 Image of Single-Color Gallery on chromosome 12, marked by red and green fluorochromes.

A great advantage in the reconstruction of the karyotype through ISIS is the possibility of observing the intensity of the signal of each fluorochrome over the entire length of the chromosome thanks to Single-Color Gallery. The Single-Color Gallery is a separate window in which all five colour channels are displayed for a selected chromosome (Figure 31). This

simplifies the recognition of complex aberrations. More details are provided in the Appendix.

3.5. Simulations using the Clustering application of Geant4-DNA

In silico simulations to estimate BNCT DNA damage were performed using the Clustering application of Geant4-DNA. The application can be downloaded from the online repository of GEANT4 under the path "extended/medical/dna" under the application name "Clustering". Like every Geant4 application, the application is written in C++ programming language and it is composed of the "main.cc file", the source files (*.cc) included in "src" folder, the header files[11] (*.hh) located in "include" folder, the output sheet recognizable because of the .out extension and, eventually, some macro files[12]. The source files of the application are:

- "DetectorCostruction", in which the geometry defining volumes and materials is specified;
- "PrimaryGeneratorAction" and "PrimaryGenerator" that allows defining particle source, to explicitly indicate the number particles and their characteristics, such as energy, momentum, space position and initial direction (more details in next paragraph);
- "PhysicsList", in which is specified the reference mathematical model of interaction with matter, in this case "G4EmDNAPhysics_Option2";
- "ActionInitialization", in which the user actions are set;
- "SteppingAction", in which energy deposits in the target are registered;
- "EventAction", which initializes and analyses every event;
- "RunAction", in which output histograms are filled;
- "ClusteringAlgo", which contains the core clustering algorithm as described in chapter 2;
- "ClusteringAlgoMessenger", which defines all graphical interface commands to tune the clustering algorithm;
- "ClusterSBPoints", which identifies a cluster of strand break points;
- "CommandLineParser", where a parser[13] for command line control is defined;
- "RunInitObserver", which allows initializations at new run;
- "SBPoint, which defines a class for point of energy deposition.

Preliminary simulations were run to verify the geometry using the graphical visualization with the "./clustering -gui" command. The workstation used is a server Intel(R) Xeon(R) with two CPU E5-2680 v3 @2.50 GHz of twelve physical core, twenty-four in hyper thread (a total of forty-eight). Then, forty-nine simulations, twelve for each component of the BNCT mixed field as reported in Table 2 plus a simulation of all the components together assuming a dose of 0.5Gy, were performed in batch mode using the macro file "run.in". The number of runs (at least 1,000,000 for gamma simulations and 10,000 for all the others) was specified in the macro with the command "./clustering -mac run.in". The results presented

[11] A header file contains the definitions of functions that can be included or imported using a preprocessor directive "#include". This preprocessor directive tells the compiler that the header file needs to be processed prior to the compilation. Every source file is associated to its header file.
[12] A macro is an action or a set of actions that can be used to automate tasks.
[13] The term parser is used in the analysis of computer languages, referring to the syntactic analysis of the input code into its component parts in order to facilitate the writing of compilers and interpreters.

in the next chapter are a weighted average of output values of single simulation as in Equation 3 and the Complexity Factor (CF), in order to evaluate the complexity of damage simulated for each component, is defined as in Equation 5 with its error (obtained by propagation of errors):

Equation 5

$$CF = Complexity\ Factor = \frac{DSB + SSBcomplex}{SSB}$$

$$\sigma_{CF} = \sqrt{\frac{\sigma_{DSB}^2 + \sigma_{SSBcomplex}^2}{SSB^2} + \frac{(SSBcomplex + DSB)^2 * \sigma_{SSB}^2}{SSB^4}}$$

It is important to note that only the statistical uncertainties were considered, while model-associated uncertainties were not considered.

3.5.1. Geometry

The MCF10A cell line presents a cell and nucleus volume size in the ranges of 678-1317 μm^3 and 360-653 μm^3 [56], respectively. Consequently, the geometry of the simulation has been implemented as follows:

* a spherical world simulating the cell with a radius of 6200 nm (value corresponding to the radius of the middle value for the volume range);
* a 3274 nm radius sphere simulating the nucleus (value corresponding to the radius of the middle value for the volume range).

The sensitive volume, the area in which interaction are registered, is the sole nucleus.

3.5.2. Source characteristics

The source of the simulations is not the neutron field because of the insufficient accuracy of Geant4 to simulate thermal neutron interaction, hence the source consists of each component of the BNCT radiation: the number of shot particles for each component was chosen from the reactions rate reported in Table 1 and normalized for one cell to obtain nominal doses of 0.5Gy. It is important to note that this number of particles represents the average number of particles generated in one cell.

Table 2 Average number of particles to shoot into the cell to obtain nominal doses of 0.5Gy and 2Gy. Only the lowest dose was simulated with Clustering application.

	0.5Gy	*2Gy*
Irradiation time (s)	600	600
Reactor power (kW)	5	20
Cell weight (g)	2.06E-09	2.06E-09
Ppm ^{10}B	30	30
Resulting average number of boron reactions	3	12
Resulting average number of nitrogen capture protons	1	3
Resulting average number of scattering protons	1106	4425
Resulting average number of gammas	8	33

The "PrimaryGeneratorAction" file was divided into two different files: "PrimaryGenerator_XXX" and "PrimaryGeneratorAction", where the "XXX" represent one of the components of BNCT mixed field (protons with 600 keV energy, scattering protons, gammas and capture reactions). In each "PrimaryGenerator_XXX", the type of particles, the direction and the position randomly chosen for each particle and the energy, established from theory, were set. For the boron-neutron capture reaction, alpha-particles and lithium ions were simulated back-to-back, as shown in Figure 32, and lithium energy was chosen according to the emission probability as in Figure 2. Instead, the energy of scattering protons was established according to the spectrum of neutrons causing scattering as calculated in [57]. In "PrimaryGeneratorAction" the number of particles to shoot in each run was set: it is possible to shoot one BNCT mixed field component at time or all the components together.

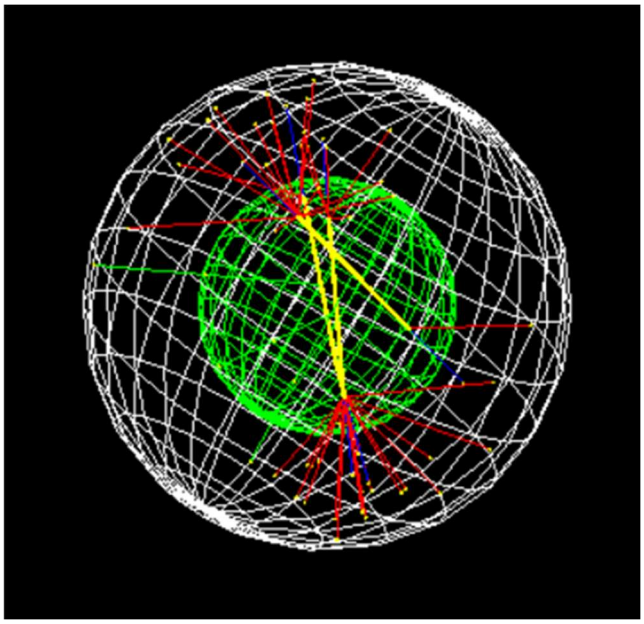

Figure 32 Geometry simulated in the Clustering application representing in white a MCF10A cell and in green its nucleus. The straight green lines are simulated gammas from lithium decay, not to be confused with those which delimit the nucleus of the cell. The yellow lines indicate alpha-particles and lithium ions diffusing back-to-back from the capture reaction and this is the only contribution of the source showed in the picture. The red lines represent electron and blue lines protons generated in the interaction processes.

3.5.3. Clustering algorithm parameters and output files

The previously described Clustering algorithm was applied with eps = 3.2 nm, representing more or less a 10 DNA base pairs distance, MinPts = 2 since at least 2 SSBs are needed to form a DSB, EMinDamage = 5 eV and EMaxDamage = 37.5 eV and SPointsProb = 0.2.
Results of each simulation comprise three different types of DNA damage: SSBs, complex SSBs and DSBs. The results were written in a root file called clusters_output.root, in which are stored the five histograms of the output quantities provided by the application (previously mentioned in chapter 2) and the mean for each histogram.

4. Results and discussion

BNCT provides an alternative approach compared to photon/electron-based conventional radiotherapy by delivering highly DNA-damaging charged particles at the intracellular level, almost exclusively inside the tumour. In the next paragraphs, the results obtained in this thesis work, both for the radiobiological assays and the Geant4-DNA simulations, are shown and discussed. More details about all the data are reported in Appendix 3.

4.1. Optimization of MATLAB foci counting

In general, the use of automatic counting systems is supposed to provide a more objective analysis, overcoming the dependence of the scoring on the observer. In addition, they could result in a significant reduction of the overall time. These systems often need to be optimized to ensure that manual and automatic counting are in good agreement. In this work, the main goal of the use of MATLAB algorithm in the scoring of radiation-induced foci was to validate the agreement between manual and MATLAB counting, used on the same sample as acquired through the Metafer software. The latter has shown a poor reliability on the counting when compared to manual scoring and would require further optimization, which is beyond the scopes of this thesis. Therefore, in this work Metafer has been used only to acquire the images as previously specified. To obtain a good agreement between manual counting and MATLAB counting algorithm, an optimization of the parameters had been carried out before BNCT experiments, using a total of 18 samples irradiated with X-rays (XR) at different doses or control samples and fixed at 0.5 or 24 hours. The best parameters are reported in Table 3.

Table 3 Optimized parameters for MATLAB classifier.

MATLAB Classifier (parameters used in the script)
parameter_pixel = 5;
perc_soglia_intensita = 0.5; threshold intensity foci
perc_soglia_intensita_blue = 0.14; threshold intensity dapi
parameter_WS_blue = 1000; size of watershed on blue channel
perc_soglia_intensita_0Gy =0.2
Threshold a 0Gy = 30*0.2

Note that for control slides the threshold parameters are different as not to overestimate the number of foci counted from captured images because Metafer automatically increases exposure time if it does not detect a high signal, which unfortunately increases the background noise. To avoid this problem, the threshold used in control samples is 0.2*30 where 30 is the mean value of foci intensity on 2-Gy samples. The overall results of optimization can be found in Figure 33. The average number of foci per cell, both for manual and automated counts, has been calculated as in Equation 1 with its error. As evident from the graph, manual and MATLAB counting are comparable within error for

all samples, hence this has allowed to use the MATLAB algorithm for the next analysis, for which at least 150 cells were used for each sample.

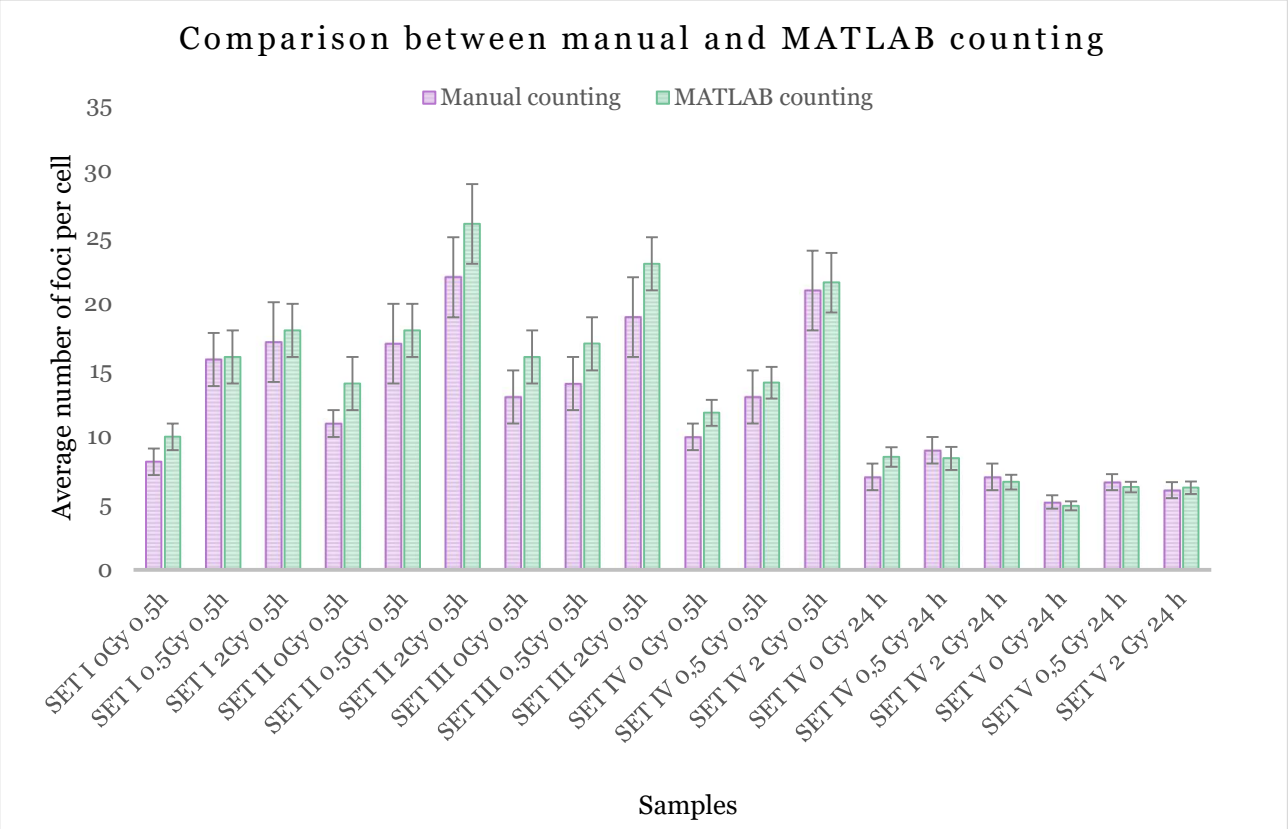

Figure 33 Results of the optimization of MATLAB parameter to obtain a good agreement between manual and MATLAB counting of colocalized foci.

As said, although Metafer offers the possibility to count foci, its classifier setup needs to be improved to achieve a good agreement in terms of counting with manual scoring. Indeed, for demonstrative purposes, in Figure 34 are shown the differences between MATLAB and Metafer counting on the same sample subjected to BNCT, using optimized parameters for MATLAB algorithm.

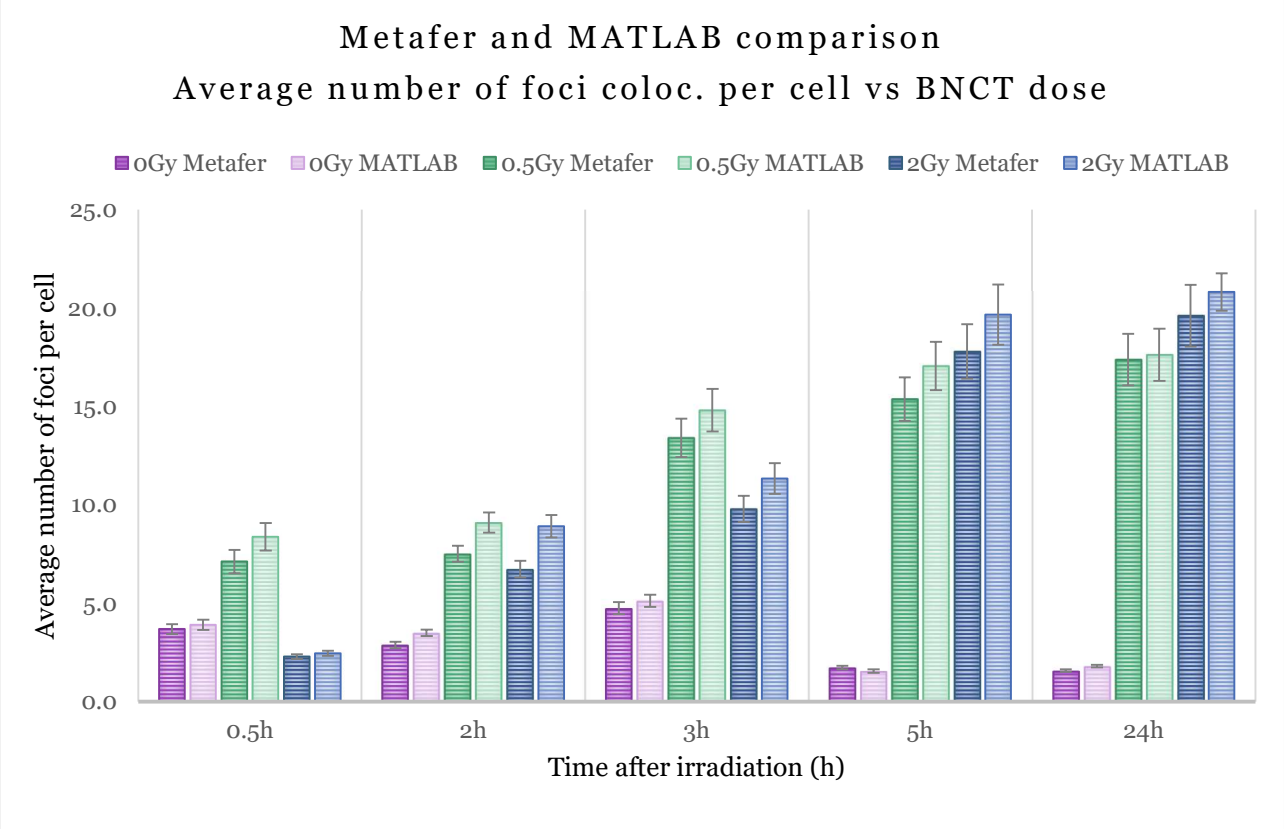

Figure 34 Comparison between Metafer and MATLAB counting of colocalized foci in samples subjected to different BNCT nominal doses fixed at different timepoints (see legend).

For control samples there is generally a good agreement (except for the 2-h timepoint), but for higher doses Metafer tends to underestimate the number of foci, in particular for 0.5Gy samples for 0.5 and 2h timepoints and for 2Gy fixed at 2h and 3h after irradiation. This is in agreement with Metafer counting and manual counting (data not shown). Moreover, a second reason to use MATLAB is that it allows also to measure the area of foci in order to evaluate DNA repair kinetics. In the next paragraph, results are presented obtained from optimized MATLAB algorithm as used to count the number of foci and the area of foci in irradiated (BNCT and XR) samples.

4.2. Evaluation of DNA repair dynamics in BNCT using the Foci Assay

In order to detect the expression of proteins involved in DNA damage repair and to highlight putative differences between BNCT treatment and XR irradiation, the Foci Assay was performed in MCF-10A cells. In particular, the use of two markers of repair proteins, one for γH2AX and one for 53BP1, allows pinpointing the colocalization of the two proteins that is considered robust evidence of a DSB repair site, thus avoiding false positives [23]. Whereas γH2AX foci describe the shape and size of a chromatin locus with damaged DNA, 53BP1 foci provide information on the formation of foci during the recruitment of proteins for repair [58] and it is not only involved in NHEJ but also acts as a stabilizing factor during HR [59]. The timepoints of analysis (0.5h, 24h for all samples plus 2h, 3h, 5h only for BNCT samples) were chosen to examine the activation or downregulation of the DNA Damage Response (DDR): as many data exists in the literature for photons in contrast with a paucity of information on BNCT, for these samples it was decided to evaluate the repair dynamics over

time. Usually the foci number, where a focus corresponds to a site of DNA repair with at least one DSB, reaches a peak of activity at 30 min post exposure and their number gradually declines over the course of 24 hours because of repair (Figure 10) [25]. Conversely, the average dimension of foci is known to increase with time showing the cell strategy on repair: simple damage is repaired first and quickly, while complex damage is repaired with a slower kinetics, leaving a significant level of unrepaired, residual damage [25]. It is important to remember that for BNCT a significant level of clustered damage is expected due to very high-LET alpha-particles and lithium ions. In Figure 35 are shown the average number of foci colocalized per cell as a function of dose at different time points.

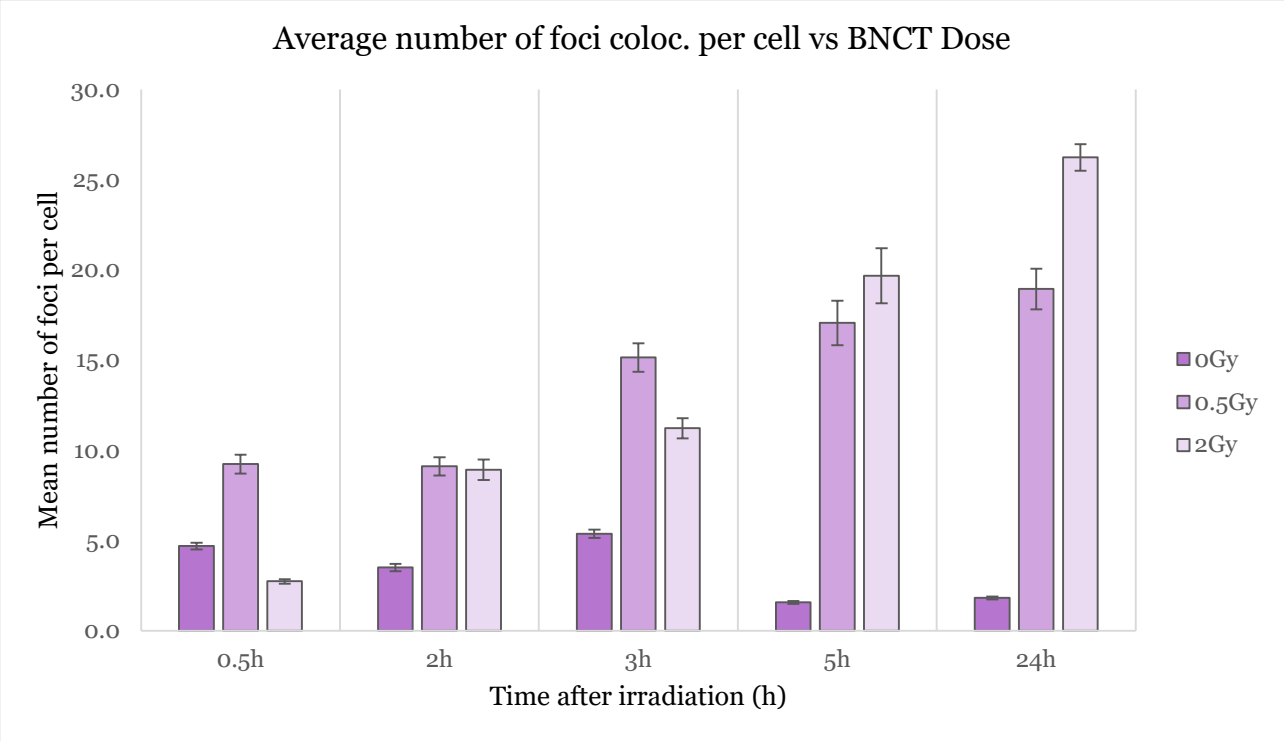

Figure 35 Average number of foci colocalized per cell vs BNCT nominal dose at different timepoints.

A few considerations can be made. First, as expected, the number of foci, hence of DNA damage, is always greater in the irradiated samples at all time points, with the exception of the first time assayed after irradiation for the nominal BNCT dose of 2Gy. This may be due to both the stress induced in unirradiated cells by transportation and non-physiological conditions at the site of irradiation; in fact, after a few hours, control samples exhibit a much decreased "stress-induced" foci frequency as they were returned to the incubator.
The kinetics of foci colocalized starting from 0.5h to 24h after irradiation is very different from the one in Figure 10, which refers to XR irradiation, because the number of foci increases with time and up to a couple of hours after irradiation a higher number of foci was detected in 0.5Gy samples compared to the higher 2-Gy dose. This potentially controversial result can be explained by arguing that it reflects a genuine biological mechanism and/or the intrinsic limits in the resolving foci clustering caused by the optical resolution of the used microscope. In fact, these reasons may not be mutually exclusive.

As regards the former hypothesis, in some studies with high-LET radiation, i.e., of the same quality as the particles produced in BNCT, foci usually appeared with a dose-dependent delay [26]. This can explain why comparing the number of foci for the two BNCT doses, the lower dose presents a higher number of foci until 5h after irradiation. The situation is completely different 24h after irradiation where the number of foci at 2Gy is much higher than 0.5Gy. Cells treated with α-particles show slow DSB repair and differences in 53BP1 accumulation and focus growth: the number of foci doubled after 2 h per nucleus and remained stable up to 17h [60], thus the presence of lithium can add to the damage and probably cause more delay. Moreover, increased mobility of chromatin surrounding DNA damage sites has been reported and was suggested to affect DNA repair [60]. Several mechanisms of chromatin remodelling operate to provide access for the repair proteins to the DSB and the adjacent DNA [59]. Chromatin fragmentation occurring in response to high-LET irradiation and chromatin decondensation that occurs during DSB repair (in response to both high-LET and low-LET irradiation) locally mobilize damaged chromatin to some extent, generating additional complex DNA lesions [61] that inhibit the action of NHEJ. This mechanism in turn delays the recruitment/mobilization of repair proteins, thereby causing an apparent increment with time in the number of detected foci. During such chromatin remodelling, 53BP1 could be thus displaced from the primary damaged site resulting in a decrease of colocalized foci at first [58].

As regards the limits incurred by the optical resolution with which the foci images could be acquired, current investigations using super-resolution light or electron microscopy revealed that γH2AX foci may be composed of several sub-units either called sub-foci or clusters [58]. The individual γH2AX clusters as determined according to fixed parameters of super-resolution localization microscopy do not always co-localize with corresponding clusters of 53BP1 [58]. This may explain the data at 30 min post-irradiation, for example, as the expected great amount of clustered damage may result in a sort of “saturation” effect, with many foci being conglomerated and being undercounted. Thus, to better evaluate the number of foci, more advanced techniques than the one presented in this work may be needed, especially in the case of BNCT-associated highly clustered foci.

On the other hand, the average area of foci tends to increase with time, in keeping with literature data for XR, alpha-particles and nitrogen ions [25, 60, 61] (Figure 36). Notably, a study using Hi-C (high-throughput chromosome conformation capture) revealed that multiple DSBs undergo clustering when repair is delayed, supporting the idea that the average area of foci increases with time [62]. Surprisingly, however, the average area at 0.5Gy is higher than the one at 2Gy. Once again, this can be caused by the acquisition system due to the distance of the focal planes in the stack of acquired images and also because the capture reactions produce particles isotropically distributed in space; consequently, the 3D structure of cells studied only in x-y planes can lead to an underestimation of the real size [61]. Moreover, a focus will probably contain more than one DSB due to the high level of clusterization, but to resolve such a focus a microscopy with nanometric resolution is needed, since the diameter of DNA double helix is around 2 nm [63].

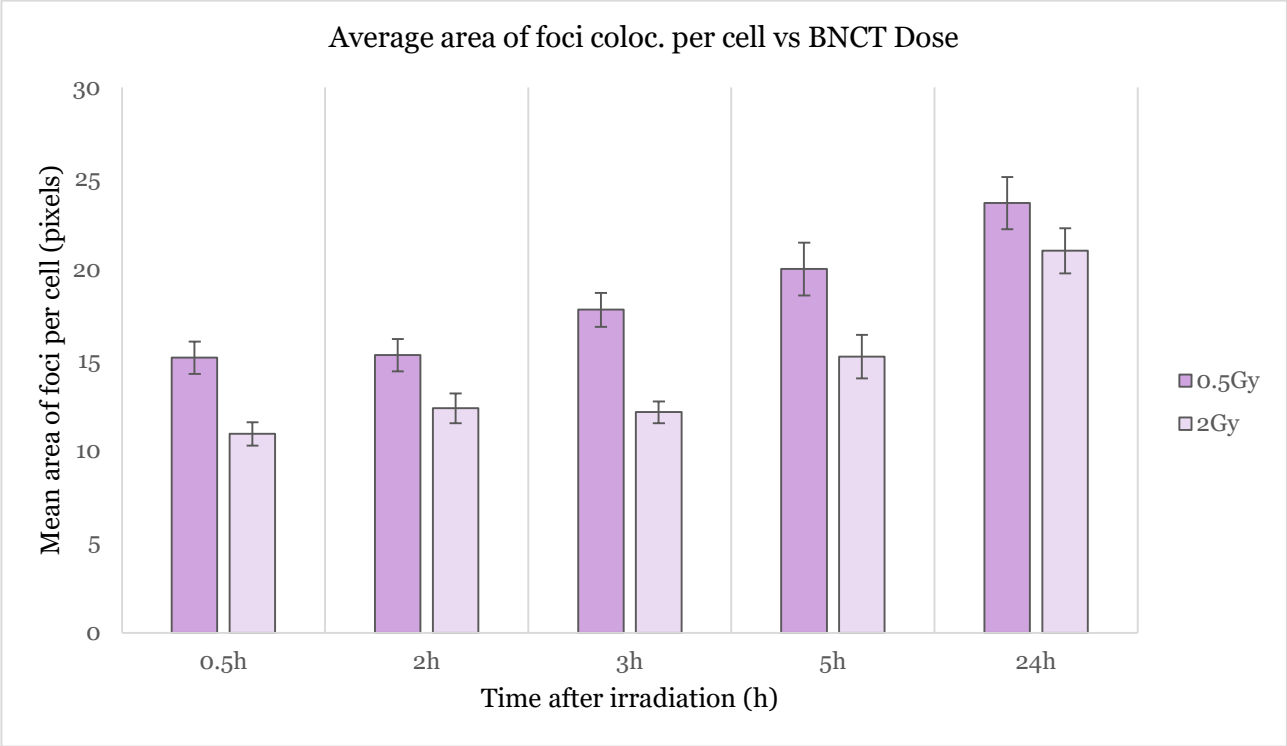

Figure 36 Average area of foci colocalized per cell vs BNCT nominal dose at different timepoints.

The hypothesis of chromatin remodelling to explain the increase with time in the number of foci after BNCT is supported by the results shown in Figures 37 and 38: it seems that the maximum number of single-protein foci is reached between 5h and 24h after irradiation while the maximum of colocalization is obtained at 24h, referring to Figure 35. Thus, it appears that the protein may take time to reach the foci and the process of re-localization has to be taken into account. This could be further investigated using live imaging Single Molecule Localization microscopy, as in [58]. Interestingly, Figure 37 shows that the number of 53BP1 foci for 2Gy at 0.5h after irradiation is comparable to the control: this depletion is suggested to be caused by an abundance of DSBs, causing insufficient 53BP1 binding [60]. The recruitment of 53BP1 is efficient up to 20–40 DSBs simultaneously induced: low α-particle doses could reach these numbers due to closely interspaced DSBs as a result of the condensed energy deposition pattern of high-LET radiation [60], hence even low BNCT doses are very likely to exceed this level of damage.
In addition, the average number of single protein foci is higher than the colocalized number under the same condition, which confirms that the use of colocalization assay avoids signals from foci not caused by radiation damage [61].

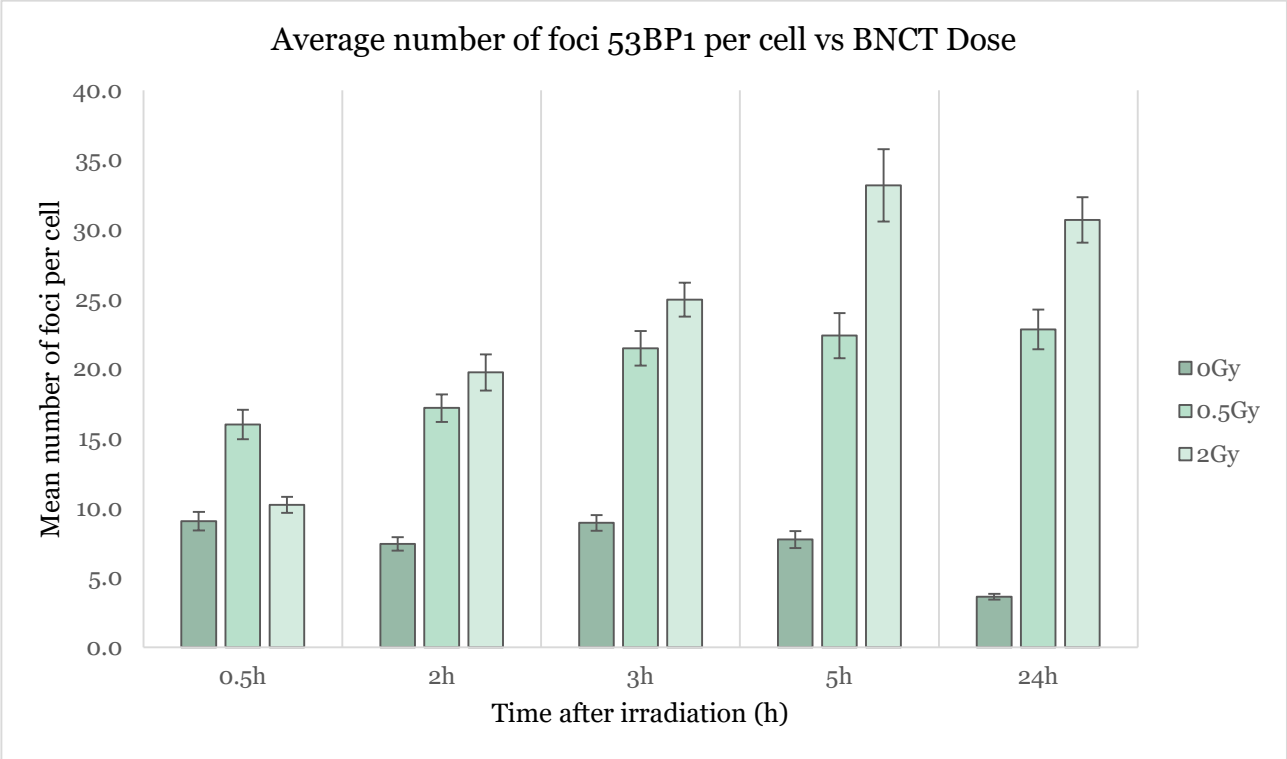

Figure 37 Average number of foci 53BP1 per cell vs BNCT nominal doses at different timepoints.

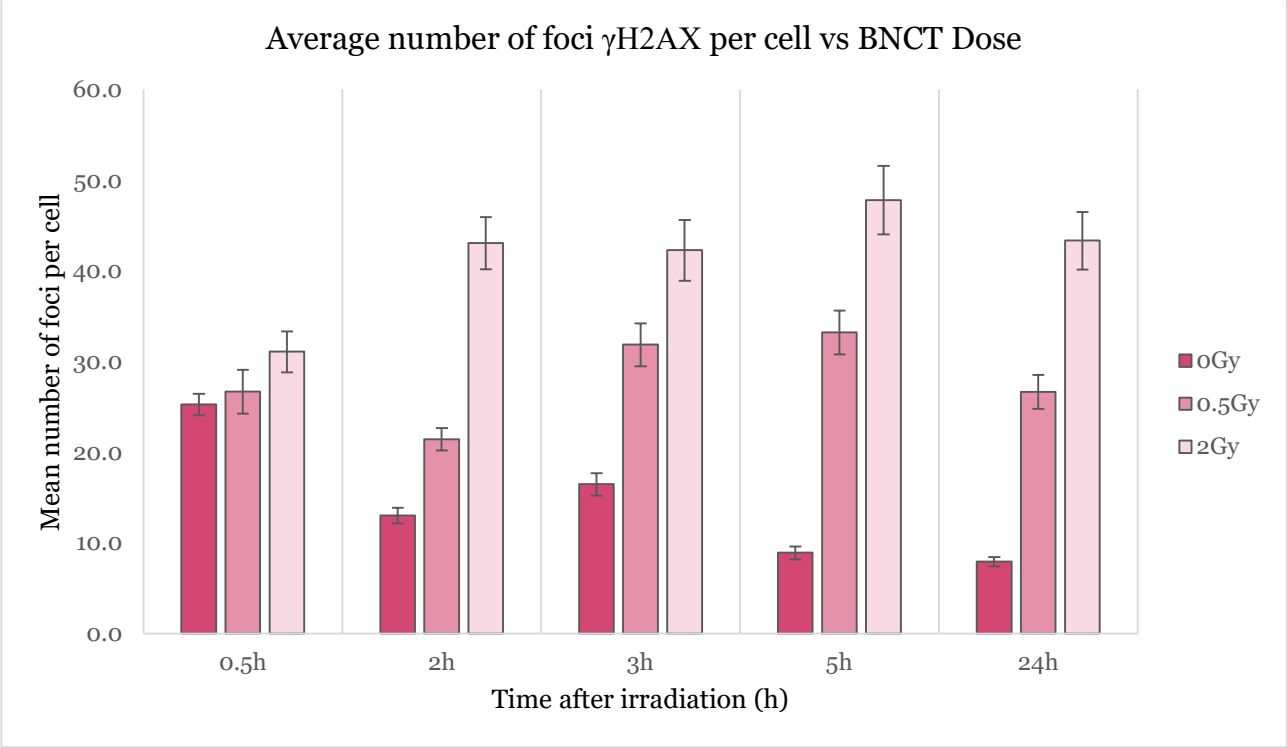

Figure 38 Average number of foci γH2AX per cell vs BNCT nominal doses at different timepoints.

The results displayed in Figures 39 and 40 confirm what has been said so far on the different dynamics of foci caused by different types of radiation, in this case XR and BNCT. At 0.5h after irradiation, it is clear that the number of BNCT foci for both dose values is not representative of all the damage induced. Furthermore, BNCT control seems to be more

stressed in terms of number of foci that XR ones, probably due to irradiation condition as previously mentioned. Then again, the data at 24h after irradiation are consistent with the slower kinetic of BNCT foci compared to the one caused by low-LET radiation [26], such as XR, due to the higher complexity and the suppression of NHEJ in clustered DSBs [59]. Actually, if for XR irradiation the number of foci returns to control levels (Figure 40) indicating the complete resolution of the damages, in the case of the BNCT the average number of foci is definitely higher than the control, 19±1 and 26.2±0.7 for 0.5 Gy and 2Gy respectively. The slow processing of non-DSB clustered lesions may also contribute to the delayed repair of BNCT-induced damage [60]. Indeed, it is worth recalling that BNCT produces a mixed-field rather than a purely high-LET radiation field. Hence, it is possible that the simpler DSBs induced by the low-LET component of such BNCT-associated field can divert the repair machinery for their prompt repair, giving complex DSBs less priority [59]. Moreover, closely interspaced DSBs may cause hyper-resection, causing a lack of repair in the G1 phase with no HR factors available, leading to persistent DSBs [60].

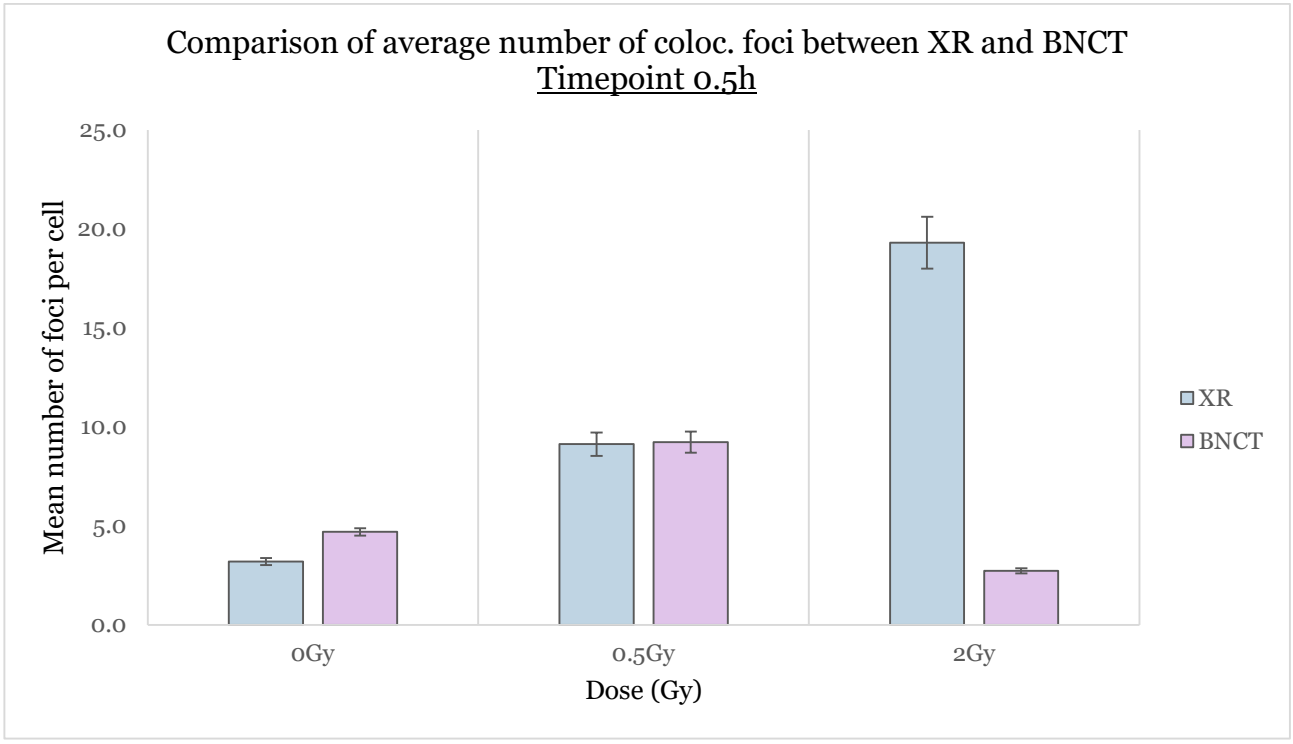

Figure 39 Comparison between the average number of colocalized foci caused by BNCT and XR at different doses 0.5h after irradiation.

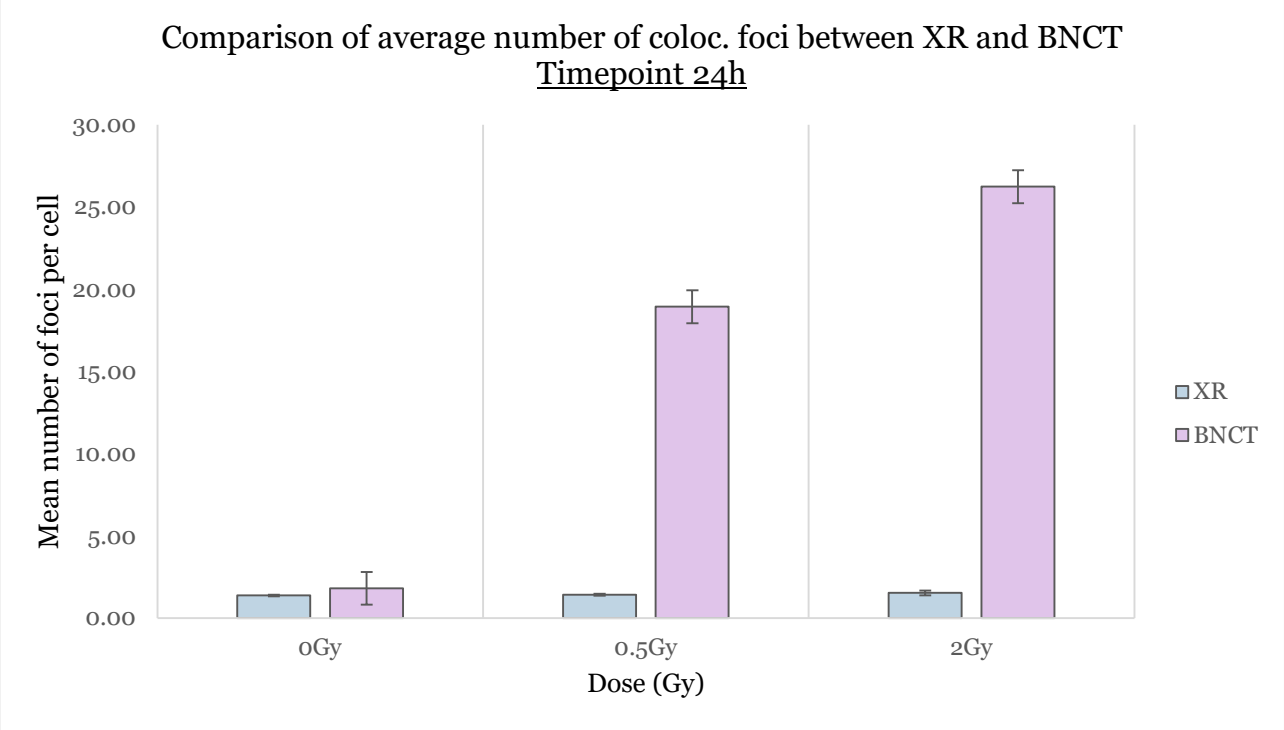

Figure 40 Comparison between the average number of colocalized foci caused by BNCT and XR at different doses 24h after irradiation.

To conclude, the lack of a disappearance of BNCT foci, actually thereof increase at 24 h post exposure, may indicate a much more complex damage compared to XR irradiation. From literature is known that B-NHEJ is thought to engage when HR or c-NHEJ are inactive or fail, hence termed "backup", mainly due to the presence of complex DSBs [31]. B-NHEJ can join unrelated DNA-ends and is therefore considered a dominant source of Chromosomal Aberrations (CAs). Since c-NHEJ fails to engage on complex DSBs, it follows that the remaining 75% are processed by B-NHEJ or other less appropriate mechanisms [31]. Clearly, the majority of complex DSBs are repaired under these conditions by highly error-prone repair pathways leading to a high number of CAs, whose results are shown in the next paragraph.

4.3. Evaluation of DNA damage complexity in BNCT using the FISH techniques

Structural chromosomal rearrangements reflect both the amount and the pattern of energy deposition events by ionizing radiation on the nanometric scale [47]. Therefore, their frequency is correlated with overall radiation-induced DNA damage and an increased proportion of complex aberration types reflects exposure to higher LET radiation. Human mammary epithelial MCF-10A cells were used to assess DNA damage after BNCT treatment in terms of CAs using WCP and mFISH techniques. The choice of non-cancer cells avoids the confoundingly high baseline CA frequency from genomically unstable cancer cells. First, as expected, aberration occurrence increases with dose for both types of irradiations (XR and BNCT) as revealed by both techniques. A comparison between WCP and mFISH techniques is carried out in Figure 41. The appropriateness of mFISH to detect high LET radiation-associated chromosome damage has been long supported [30].

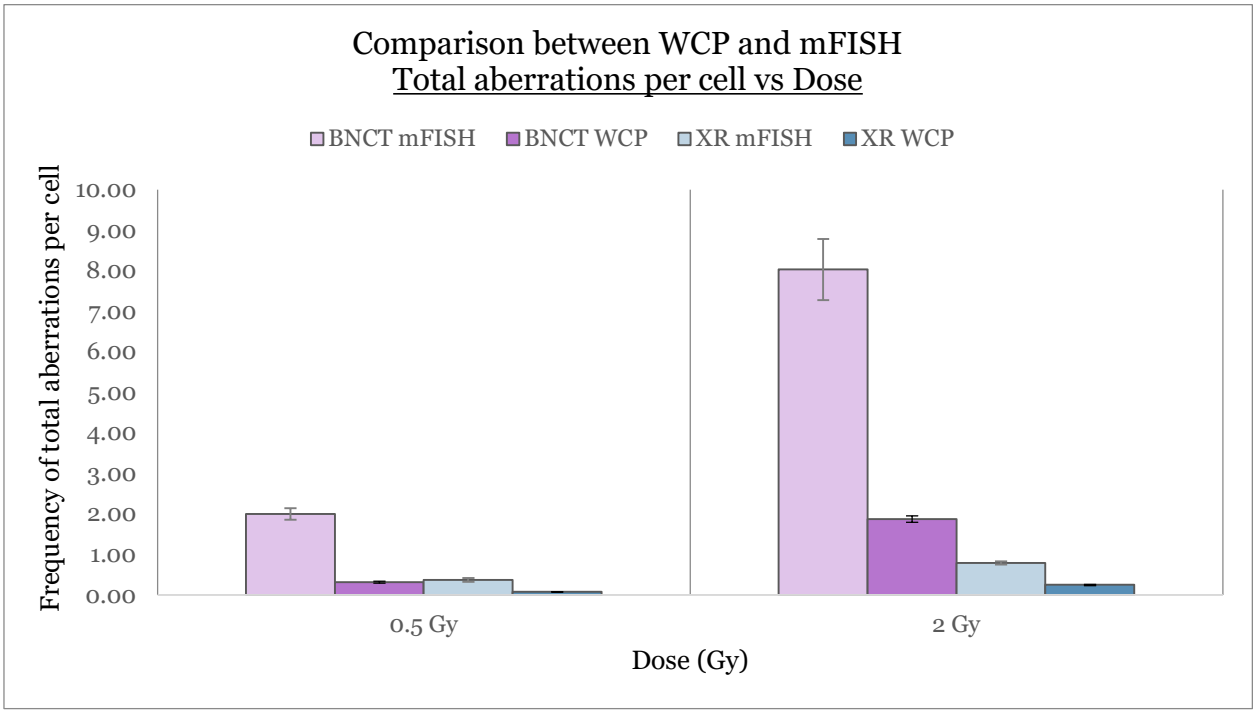

Figure 41 Comparison between the frequency of total aberrations per cell obtained using WCP and mFISH for the two doses used.

Histograms clearly show the superiority of mFISH technique versus conventional WCP in the assessment of CAs due to the more accurate chromosome scoring that allows identifying any structural exchange involving the whole karyotype (Figure 42). WCP offers the advantage of a rapid assessment of DNA damage as it paints only some pairs of homolog chromosomes (in this case, chromosomes 1 and 2); on the other hand, this obviously leads to an underestimation of CA frequency: mFISH frequency is three to six time-fold higher than the one obtained from WCP (Figure 41). The major limitation of WCP emerges when analyzing samples irradiated with high-LET radiation.

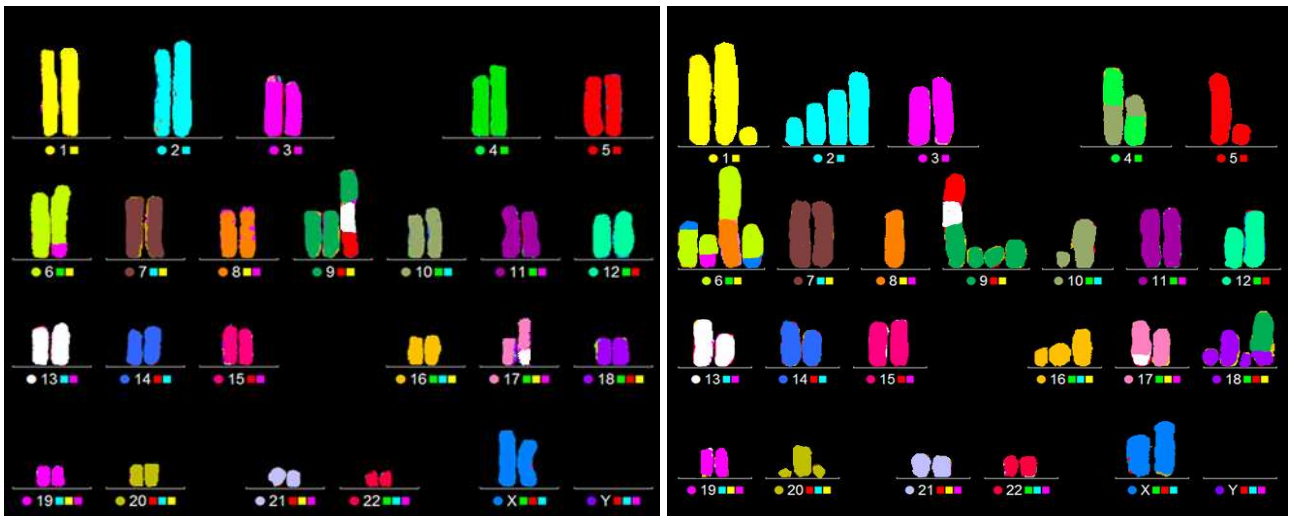

Figure 42 Reconstructed karyotypes by mFISH: on the left a control karyotype, on the right a 2Gy nominal dose BNCT karyotype. The control cells already have some stable aberrations, which are present in every cell and are excluded from the scoring. The irradiated cell shows an aberrated karyotype, for example there is a complex aberration involving the chromosomes 6, 3 and 8.

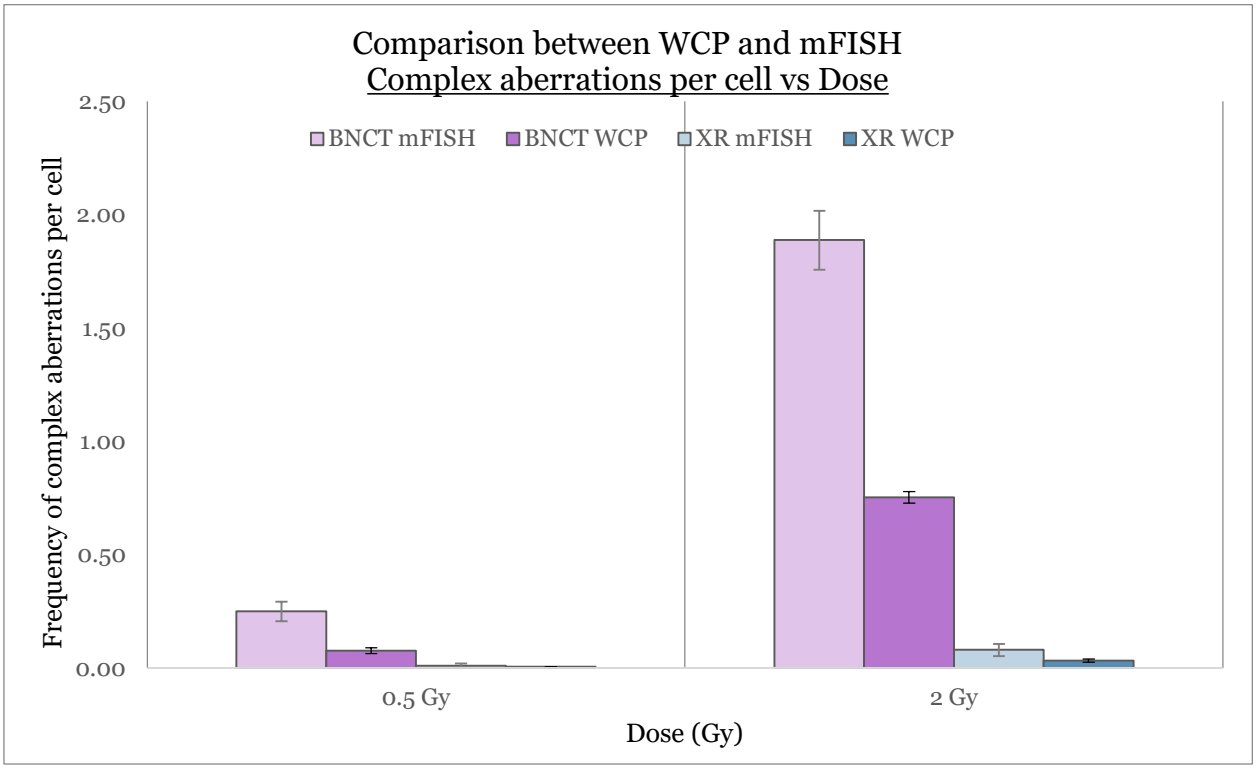

Figure 43 Comparison between the frequency of complex aberrations obtained using WCP and mFISH.

Indeed, this aspect can be appreciated in the comparison between complex aberrations revealed by the two techniques (Figure 43). For a complex aberration to be detectable by two-colour WCP, it is necessary that the rearrangement involves at least one chromosome painted with at least two breaks and one unspecifically painted or two chromosomes painted with different colour and another unspecifically painted one. The probability that this happens is very low, hence WCP gives a strong underestimation of complex exchanges compared to mFISH [64]. This is not very relevant in the case of XR irradiation, where the percentage of complex aberration becomes significant at quite high dose values, but it is essential in the case of BNCT treatment, or other high-LET irradiations. While WCP complex frequencies for XR are around a half of the ones obtained with mFISH, the underestimation for BNCT treatment is around 3-fold. Moreover, for mFISH the possibility to visualize all the chromosome allows counting breaks and number of chromosomes involved with high precision. Nonetheless, WCP is still widely used because of the lower costs: the five probes required for mFISH are more expensive compared to the two employed in FISH and karyotype reconstruction is very time consuming.

The most important result is that a significant increase in the overall yield of mFISH-painted CAs as well as of complex-type CAs was measured following BNCT irradiation compared with XR (Figures 44 and 46). As said at the end of the previous paragraph, the former can be considered a marker of B-NHEJ mechanism of repair, which is particularly error-prone in the presence of more damage per dose. More specifically, XR irradiations, at both doses, yield a frequency of total aberrations below 1, whereas BNCT irradiations caused the frequency to be way higher, respectively 2.0±0.1 and 8.0±0.8 for 0.5 Gy and 2 Gy, respectively.

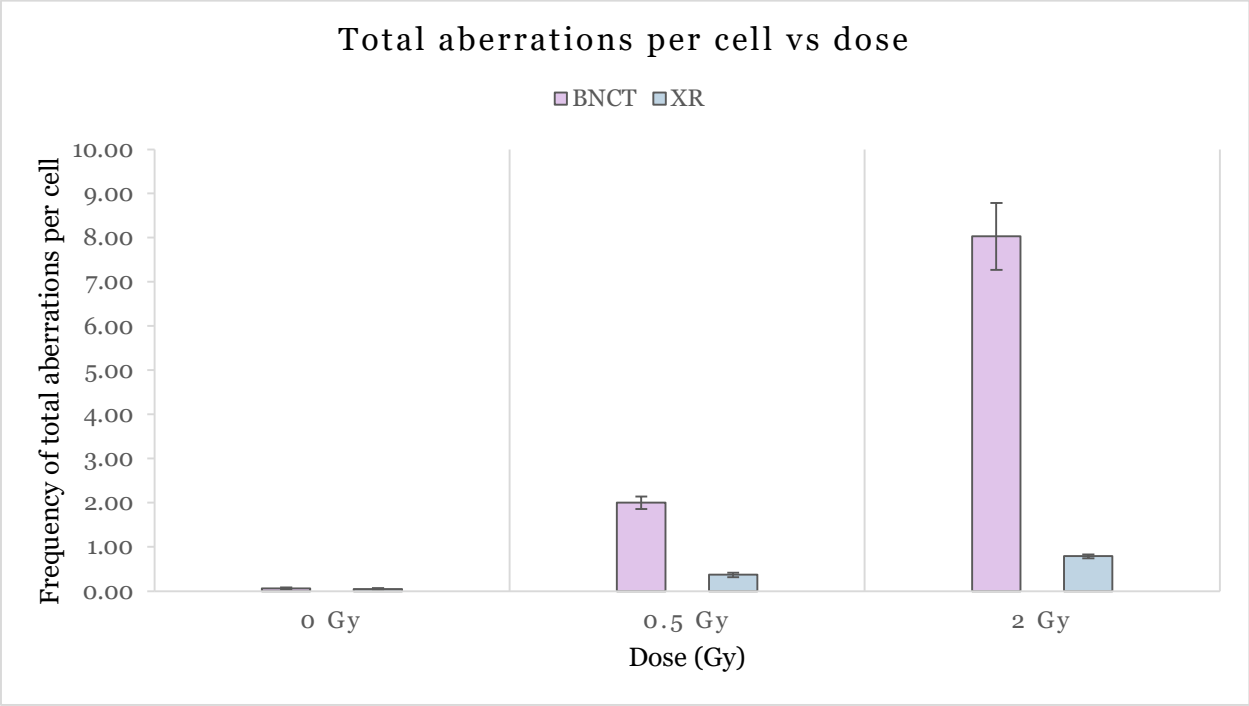

Figure 44 Frequency of total number of aberrations per cell vs dose comparing BNCT and XR results.

Additionally, the greater proportion of complex-type aberrations found (Figure 46), including rings, strongly supports the role of the $^{10}B(n,\alpha)^{7}Li$ reaction. Ring chromosomes, as in Figure 45, arise following breakage and rejoining in both chromosome arms, so this event has higher probability to happen in the case of high LET [30]. Indeed, only BNCT samples have a frequency of rings different from control, 0.02±0.01 and 0.20±0.04 for 0.5Gy and 2Gy doses respectively. Figure 45 shows also an example of dicentric and translocation.

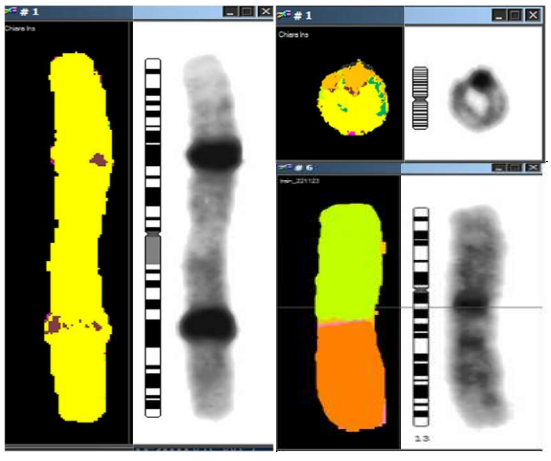

Figure 45 Example of dicentric aberration (left, chromosome 1), ring aberration (top right, chromosome 1, translocation aberration (bottom right, chromosomes 6 and 8).

No evidence of an increase in overall CA frequency nor of complex-type CAs was observed in MCF-10A cells between control samples treated or not with BPA.

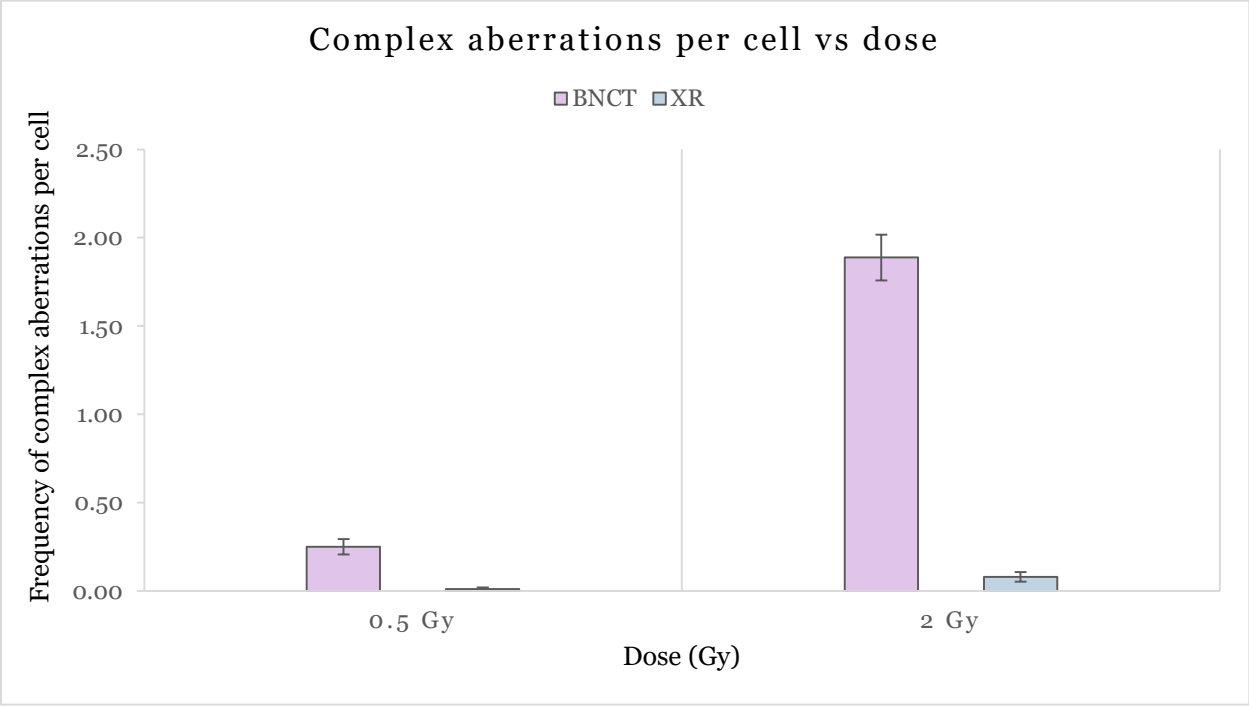

Figure 46 Frequency of complex number of aberrations per cell vs dose comparing BNCT and XR results.

As mentioned, the radiobiological rationale underlying BNCT is related to the highly spatio-temporally clustered nature of the lesions, created at the DNA level by the densely ionizing particles from boron capture, which will compromise cellular repair proficiency [31]. Moreover, compared to sparsely ionizing radiation, more chromosomal domains will be likely to be traversed by a single α -particle or lithium ion [47] track, which will in turn cause multiple DNA breakage sites. This will manifest itself as an increase in the overall complexity of the chromosomal rearrangements arising from misrepair of damage. In order to evaluate the complexity of DNA damage, the number of chromosomes and breaks involved in complex aberrations were scored separately. Figures 47 and 48 show the higher degree of complexity that accompanied the complex exchanges found in the BNCT-exposed samples: while for XR irradiation very few chromosomes were involved with a number of breaks compatible to control for 0.5 Gy and equal to 0.24±0.04 for 2Gy, in the case of BNCT the frequencies of chromosomes per complex exchange per cell are 0.66±0.05 and 5.9±0.5 and the frequencies of breaks per complex exchange per cell are 0.84±0.04 and 7.9±0.7 respectively for 0.5 Gy and 2 Gy. Such values again confirm the effect of high-LET radiation.

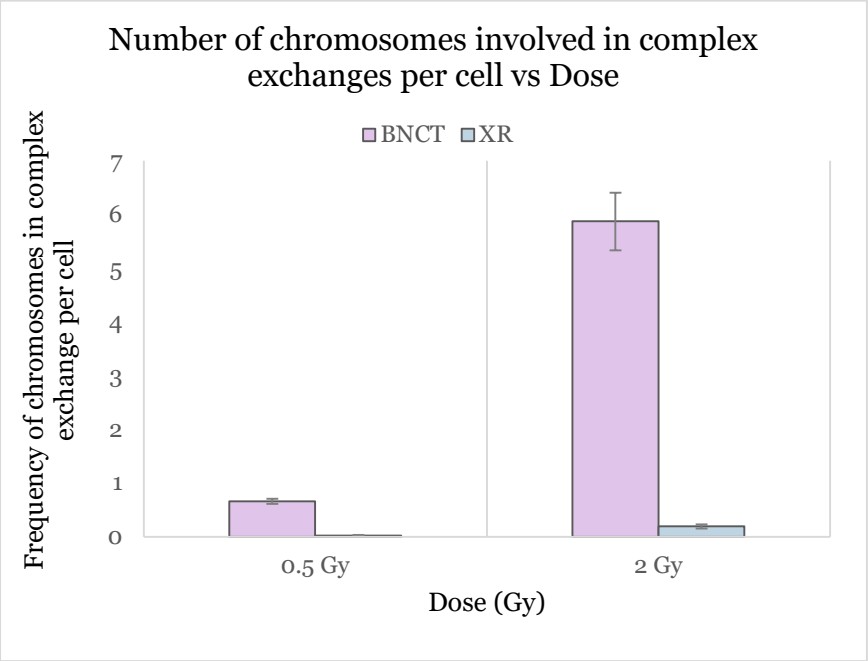

Figure 47 Frequency of the number of chromosomes involved in complex exchanges per cell vs dose comparing BNCT treatment and XR.

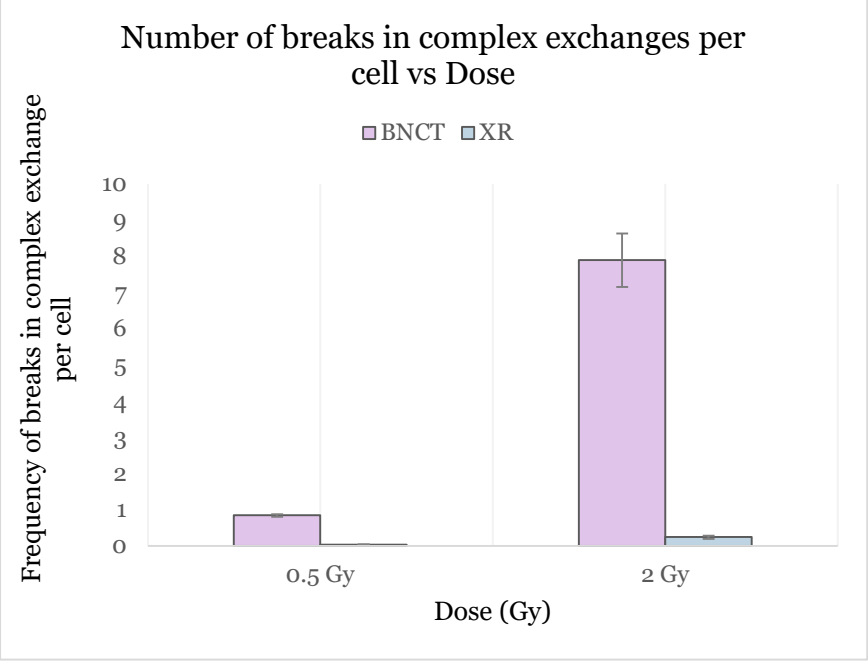

Figure 48 Frequency of the number of breaks forming complex exchanges per cell vs dose comparing BNCT treatment and XR.

These results confirm the high effectiveness of BNCT treatment in terms of DNA damage compared to conventional treatment. A high degree of complexity, in addition to the increase in the frequency of aberrations, represents a considerable difficulty for the cells to repair the damage, thus this will probably cause an enhancement of cancer cell killing [31]. In literature, compared with extensive results on the induction of CAs in human cells by hadrons and neutrons at mean energies of 20 keV, relatively little information has been

published on the effects of BNCT at the DNA level (for neutrons of around 0.025 eV) [47, 65]. Schmid et al. studied the frequency of dicentric and ring on mitotic[14] cells using Giemsa staining[15] irradiated with neutrons in presence of BPA at different doses, including 0.5 Gy and 2 Gy. There are some discrepancies on the amount of damage probably due to the different methodology: the reported frequency of aberrations is lower compared with the mFISH data shown here, because mFISH allows a higher degree of accuracy. Moreover, the use of calyculin A-induced Premature Chromosome Condensation (PCC) is strongly recommended for the study of high-LET radiation CAs because complex and clustered damage, peculiarly caused by such radiation, slows down cell cycle at cellular checkpoints to give time DNA mechanisms to repair damage [66]. Thus, limiting the analysis to mitotic chromosomes would result in significant underestimation of overall damage as those cells with the higher burden of damage will be less likely to reach mitosis.

4.4. Results of simulations through the Geant4-DNA Clustering application

In order to complement the experimental work, Monte Carlo simulations were performed, allowing a deeper insight into how the physical interactions are connected to biological damage. Indeed, theoretical predictions of biological damage are helpful for planning experiments and for interpretations of the results. To reach a spatial resolution at the DNA level, it is necessary to adopt a more detailed description of particle transport. This is achieved by simulating all elastic and inelastic collisions one-by-one, until all particles slow down to thermalization energies, in practice, the ionizing threshold of the medium (which is in around 10 eV for tissue-like materials) [67]. The toolkit used is the extension at low energy of Geant4 called Geant4-DNA, to date the only open-source available for biological damage simulations. The application used is the Clustering application that allows simulating some types of biological damage on specified geometry: SSBs, SSBcomplex and DSB. It is important to remember that a DSB is defined as a cluster of at least two breaks on different DNA strands, this definition being more similar to what is observed in terms of foci if the analysis is not carried out with super resolution microscopy. The simulation used a density-based clustering algorithm to associate physical energy deposition to biological damage with a certain probability, avoiding the complexity of superimposing energy depositions on very accurate geometry of DNA. Moreover, the output comprises the average cluster dimension, in terms of number of points (breakage of DNA) that form the cluster. This is an indicator of energy pattern deposition of the type of radiation. In addition, the Complexity Factor (CF), introduced in the previous chapter, was implemented as it represents the fraction of complex DNA damage simulated, comprising DSBs and SSBcomplex, over simple damage, represented by SSBs. This factor is useful to evaluate which component of BNCT mixed field (boron capture particles, low-LET gamma rays from the capture of thermal neutrons by hydrogen and from the photons present in the neutron beam, intermediate-LET protons

[14] In cell biology, mitosis is a part of the cell cycle in which replicated chromosomes are separated into two new nuclei.

[15] In cytogenetics, Giemsa staining is used to visualize chromosomal banding; in particular, it allows to visualize the chromosomes in blue color thus highlighting structural chromosomal aberrations as ring, dicentric and fragments.

originated by the scattering of fast neutrons and by thermal neutron capture in nitrogen) causes more complex DNA damage.

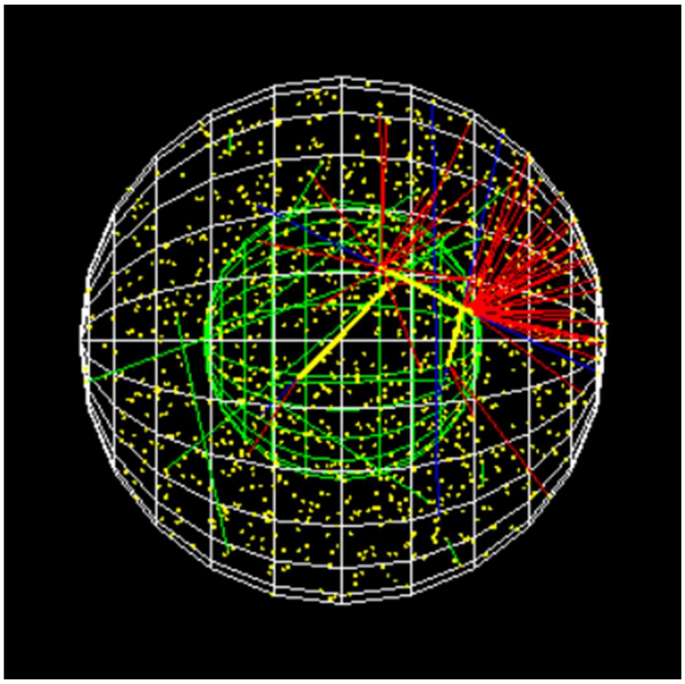

Figure 49 Graphical interface of simulated MCF10 cells irradiated with 0.5Gy of BNCT nominal dose. The cell is represented in white, the nucleus with curved green lines, the gammas with straight green lines, protons, alpha-particles and lithium ions in yellow. Red and blue lines represent electron and protons generated by other interactions.

The geometry used simulates a MCF10 cell and the source of radiation is composed by different particles in random positions shot at random directions (see previous chapter). In Figure 49 shows the graphical interface of a run simulating 0.5Gy of BNCT dose. The first simulations divided BNCT mixed field into four components, as mentioned above. The number of particles shot is chosen for simplicity to simulate the lowest dose used in this work, i.e., 0.5Gy. Figure 50 shows the results of these simulations.

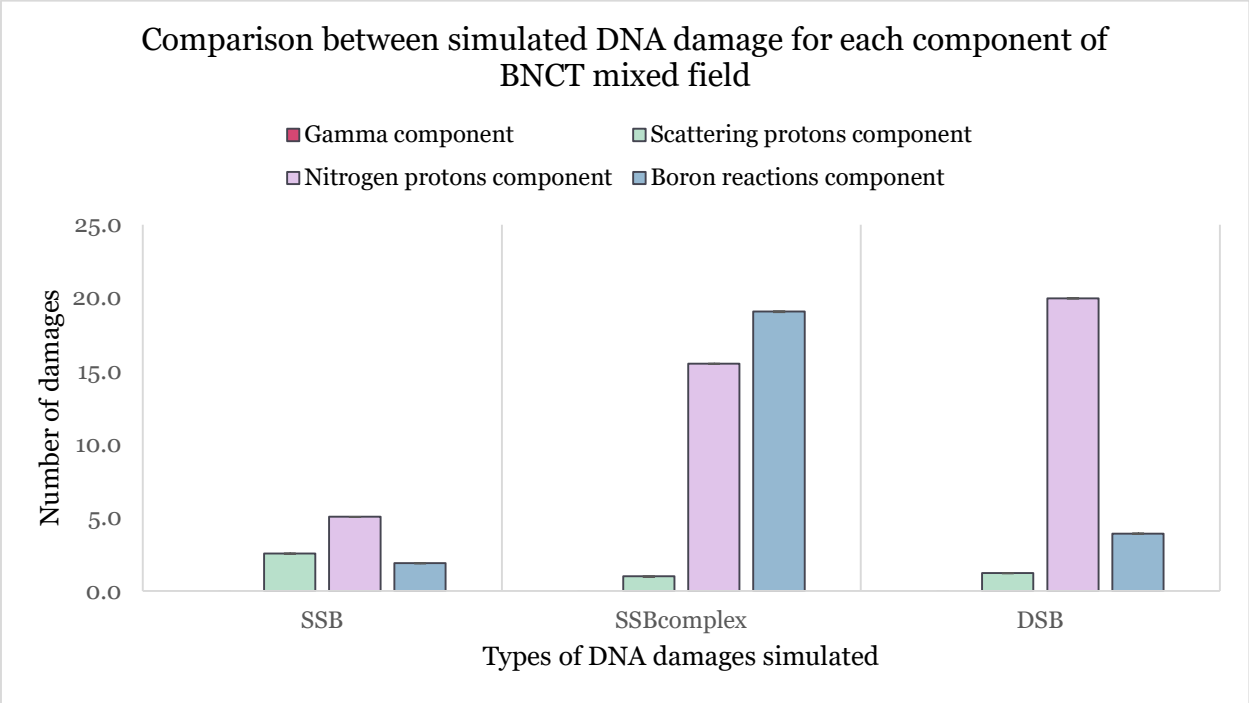

Figure 50 Comparison between the simulated number of DNA damage types caused by each component of BNCT mixed field using 0.5Gy of BNCT nominal dose. The types of DNA damages simulated are SSBs, SSBcomplex and DSBs.

As evident, the contribution of the gamma component is negligible compared to the others, not only for complex damages but also for the simplest ones, which is the reason why, for the gamma component, the number of runs has been brought to 1,000,000 to increase the statistical robustness of the simulation. Scattering protons are the most numerous component of the mixed field but the damage they yield is lower compared to the other components, particularly in terms of number of breaks and of complexity, except for gammas. The average number of SSB produced is around two-fold higher that of SSBcomplex and DSB. Nitrogen-capture protons and boron-capture particles are the most damaging elements, as expected. The number of SSBs caused by protons from nitrogen capture is more than twice that produced by boron capture; on the other hand, there are similar value of SSBcomplex, a little higher in the case of boron capture particles. The DSB number is higher for the nitrogen component: it exceeds by a 4-fold factor those caused by the boron component. A possible explanation for this can be found in the size of the clusters. Referring to the Table 4, while boron component clusters have an average size exceeding 2, all the others are near 1, which means that s mostly generate “single” DSBs, a damage simpler to repair. Moreover, in the case of boron component the maximum cluster size is 18, three times the maximum size of protons from nitrogen capture. As expected, boron captures generate particles capable of inducing way more complex damage: looking at the Complexity Factor, this is 1.7 times higher than the one of protons from nitrogen capture, 14 times the one of scattering protons (even though there are only 3 reactions versus a thousand of protons) and 110 times the one of gamma component.

Table 4 Mean cluster size and Complexity Factor of each component of BNCT mixed field simulating 0.5Gy BNCT nominal dose.

Component	*Mean cluster size*	*σ*	*Complexity Factor*	*σ*
Gammas	1.0541	0.0001	0.11	0.02
Scattering protons	1.172	0.001	0.866	0.002
Protons from nitrogen capture	1.295	0.001	7.02	0.01
Boron reactions	2.371	0.004	12.15	0.03

These results confirm the expected view of the energy deposition pattern underpinning the radiobiological rationale behind the BNCT.
Last but not least, simulations of all the components together may help to interpret biological results. Table 5 shows the comparison between the number of DSB simulated and the number of DSB as measured by the Foci Assay and the mFISH technique. About the Foci Assay, as mentioned before, the results at 0.5h after irradiation cannot be considered reliable since the number of observed foci tends to increase with time, thus the values in the table are the average number of colocalized foci at the last studied time point, that is 24h after irradiation. For mFISH, the DSBs are calculated from the number of double helix breaks from which the aberration arose: the breaks in complex aberrations were scored independently; instead, each translocation or dicentric or ring was assumed to result from two breaks by definition, lastly each fragment was counted as the result of one break.

Table 5 Comparison for 0.5Gy of BNCT nominal dose of the number of DSB inferred from simulations and biological assays: Foci Assay and mFISH technique.

Dose (Gy)	*Simulated DSB*	*Foci Assay DSB*	*mFISH technique DSB*
0.5	22.9 ± 0.2	19 ± 1	4.0 ± 0.3

It is clear that a portion of the induced damages was repaired but such repair was not necessarily accurate: the foci data represent “residual”, or better to say, unresolved DSB after 24h while aberration data are the result of misrepaired damage after 36h while the simulations refer to early damage (30 min). Actually, if we assume that simulations return a good estimation of early DNA damage, from mFISH-based calculation of DSB, it is possible to estimate the percentage of damage that the cells misrepaired. This can be determined dividing the mFISH value for DSBs by the simulated one: the result is (17± 1) % for 0.5Gy of BNCT treatment. Although such a result may misleadingly suggest that only a relatively small proportion of BNCT-associated damage was misrepaired, but it is important to remember the experimental results presented in the previous paragraph, which showed how such misrepaired damage was dominated by complex damage vs. simple damage in BNCT compared to photons.
On the other hand, simulated and Foci experimental data do not seem to agree because the simulated data referred to immediately induced damage and experimental ones after 24h but showing an increasing trend with time, thus one may expect that the simulation should have yielded a much lower value. Instead, a discrepancy was found equal to 3.9± 1.2. A possible explanation for such divergence includes: the lack of reliable foci data at 0.5h after irradiation; the underestimation of foci count due to the limited resolution of microscope;

the simplicity of the Clustering application compared to the newest releases, such as the MolecularDNA application. Nevertheless, from the above considerations it is possible to conclude that the results obtained with the Geant4-DNA study give a reasonable, first-order approximate value of the DSBs produced by BNCT in cells, and they present a good correlation with the foci experimentally counted.

Conclusions and future perspectives

This work represents an *in vitro* and *in silico* radiobiological study of the effects of Boron-Neutron Capture Therapy (BNCT) at the DNA level. Despite the long-standing research, very little has been investigated on the radiobiological mechanisms underlying cellular response to BNCT other than tumour cell death [2].
The cells used were human epithelial mammary cells (MCF10A). This is a non-tumorigenic breast epithelial cell line, frequently used in DNA damage studies because of its relatively stable genome to avoid the confoundingly high damage baseline of cancer cells. Before each neutron irradiation the cells were treated with BPA for 4 hours (80 μg of ^{10}B per ml of culture medium). BNCT irradiations were performed in Pavia at Triga Mark II research reactor (University of Pavia) and X-rays irradiations at the Physics Department "Ettore Pancini" of University of Study "Federico II" in Naples. The experimental activity took place at the Radiation Biophysics Laboratory of the Physics Department "E. Pancini", University Federico II of Naples and at the Laboratory of Experimental Surgery, Department of Clinical-Surgical Sciences, Polo Cravino, University of Pavia.
The three radiobiological assays performed are: Foci Assay, Whole Chromosome Painting (WCP) of chromosomes 1 and 2 and multicolour Fluorescence In Situ Hybridization (mFISH) technique.
By means of the Foci Assay it is possible to evaluate the repair kinetics after irradiation. The co-localization of fluorescence intensity signals (foci) related to early repair events elicited by radiation-induced DNA breakage, specifically histone γH2AX phosphorylation processes and 53BP1 protein recruitment, are a well-established method to avoid signal from foci not induced by radiation. The effectiveness of repair mechanism can be assessed from the frequency and the dimensions of foci at times subsequent to exposure to radiation. The assay can exploit the relative possible impairment of DNA Damage Response (DDR) due to the expected clustered damage in the case of the high-LET particles generated by the neutron-capture reactions [10]. To assess the number of foci and their area, a MATLAB software was written and optimized for the counting. The software was then used to evaluate these quantities: for BNCT irradiated samples at different timepoints after irradiation (0.5h, 2h, 3h, 5h, 24h) and for X-rays only at the first and the last timepoint mentioned. The results show an opposite kinetics of BNCT samples to the one expected regarding the number of foci, while the kinetics of X-rays irradiated samples reproduces literature data [25]. This potentially controversial result needs more analysis; the most plausible explanations comprise both biological mechanisms, such as delayed activity of DDR caused by high-LET radiation [26] or chromatin remodelling [62], and intrinsic limits in the resolving foci clustering caused by the optical resolution: to overcome this problem a super resolution microscope would be required [58, 61]. On the other hand, the areas of BNCT foci follow the expected (little) increasing trend because multiple DSBs undergo clustering when repair is delayed [62].
Structural chromosomal rearrangements reflect both the amount and the pattern of energy deposition events by ionizing radiation on the nanometric scale [47]. Therefore, their frequency is correlated with overall radiation-induced DNA damage and an increased proportion of complex aberration types reflects exposure to higher LET radiation. The

interpretation of CAs data was very unequivocal: BNCT produces an increased yield of CAs, detected by both mFISH and WCP, compared to X ray-irradiated samples, particularly of those highly complex in nature, deriving from misrepaired clustered DNA lesions. This confirms the rationale behind the BNCT. mFISH, in particular, was used because it allows a detailed quantification of the number of chromosomes and breaks involved in each complex-type chromosomal rearrangement, thereby providing an accurate estimate of the degree of complexity compared to those detected by WCP [54]. BNCT irradiated samples show a very high degree of complexity compared to X-rays irradiated ones.

In addition, simulations using the Clustering application of Geant4-DNA, after the appropriate modelling of the cell and the source, were performed as a means to compare theoretical predictions to the experimentally obtained biological data as well as to investigate which component of BNCT mixed field (i.e., scattering protons, protons from nitrogen capture, gammas and $^{10}B(n,\alpha)^{7}Li$ reactions), induces more complex injuries. As expected, boron capture reactions represent the most damaging component followed by protons from nitrogen capture, while scattering protons and gammas give very low contribute in terms of number of damage and complexity. Lastly, although the comparison with biological data for the lowest dose is not fully satisfying, the in silico data provide a reasonable first approximate value of the DSBs. To our knowledge, this is the first time that such a comparison was done not only with foci in normal cells but also and more importantly with chromosome aberrations, a more reliable indicator of damage complexity. Indeed, this work is original because it applied FISH techniques to BNCT-irradiated samples.

There are clear prospects for developing more advanced computational tools that could be used in multidisciplinary studies. The limitations vary from the lack of experimental information on the processes involved up to the broad uncertainty of used parameters or the large fluctuations of parameters that are exploited to describe cell sensitivity [67]. Still, a significant effort is needed to evolve simulation tools for applying them on studies of cell population (tissues) or even (in the far future) on human organs.

From these results, it emerges that BNCT is a promising option to treat radioresistant tumour due to the high level of poorly reparable damage induced at DNA level that will probably lead to cell death. Since controlled intracellular targeting is of great importance in inducing the cell-killing activity only in cancer cell, such targeting should be further assessed, together with carrying out adequate research and clinical trials to determine the most profitable and promising routes in drug delivery systems.

To summarize, all the data here presented showed the effectiveness of BNCT compared to conventional low-LET radiation-based radiotherapy and enlighten the clinical potential of this treatment. Thus, these results may help understand potentiality and risk of this type of treatment providing interesting insights for further studies. Importantly, this kind of studies provide valuable information on the dose-effect relation in BNCT, ultimately leading to a better dose prescription in patient and an improved prediction of the clinical outcomes. Next studies will need to clarify the basic mechanisms of DDR, for example in terms of modulation of signalling pathways, in order to enhance BNCT therapeutic effectiveness and reduce associated toxicity. To conclude, the key factor to push BNCT in new clinical and research era, is a close collaboration between different disciplines, ranging from physics to surgery, from chemistry to radiation oncology, and from computer sciences to radiation biology, promoting a more comprehensive understanding of the irradiation effect and a

more strategic application in clinical settings. Such a diverse collection of intellect requires coordination to develop the synergies necessary to move forward.

Appendix

1. *Biological protocols:*

1.1. *Foci Assay protocol*

Fixation:
1) Remove the medium from the petri dish
2) Wash the cells twice with PBS (1.5 ml)
3) Add 1 ml of 4 % paraformaldehyde and leave for 15 min at room temperature (RT)
4) Wash the cells three times with PBS (1.5 ml) – at this point the cells can be stored in PBS at 4°C

Permeabilization:
5) Remove the PBS and add 1 ml of permeabilization buffer to the petri dish and incubate for 15 min at RT
6) Remove the permeabilization buffer and wash the cells with PBS

Blocking:
7) Remove the PBS and add 1 ml of blocking buffer (BB)
8) Incubate for 1 h at 37 °C in humidified atmosphere

Antibody:
All the stock antibodies have to be centrifuged briefly before use (and kept for couple of minutes (~ 10) before centrifugation at RT)

9) Add 100 µL of 1 µg/ml primary antibodies mixture (1:1000) in BB on a petri dish covered with parafilm
10) Incubate for 1 h at 37 °C the glass coverslip (previously drained on paper) "faced down" on a 100 µl drop of primary antibodies mixture in BB (or overnight at 4 °C in fridge)
11) Remove the blocking buffer BB from the petri dishes
12) Remove the glass coverslips from the parafilm and place them back in each petri dish
13) Wash the petri dishes 4 times with 1.5 ml of washing buffer (WB) – 5 min each wash

From now on work in dark (not under direct light)

14) Add 100 µL drop of 1 µg/ml secondary antibodies mixture (1:1000) in BB on a petri dish covered with parafilm (2 µg/ml Anti-mouse (γH2AX) and 4 µg/ml Anti-rabbit (53BP1))
15) Incubate for 1 h at 37°C in dark the glass coverslips (previously drained on paper) "faced down" on a 100 µl drop of primary antibodies mixture in BB
16) Remove the WB from the petri dishes
17) Remove the glass coverslips from the parafilm and place them back in each petri dish
18) Wash the petri dishes 4 times with 1.5 ml of WB – 5 min each wash

Posthybridization:
19) Remove the WB and add 1.5 ml of PBS to each petri dish
20) Place the glass coverslip (previously washed in dH20 to remove PBS salts prior to slide mounting, and drained on paper) "faced down" on a drop of Prolong Gold antifade with DAPI on the slide (previously cleaned with ethanol).
21) Leave the slides (lying flat) in the dark overnight at RT
22) Slides can be viewed (and acquired/scored) or stored in -20 °C in freezer

1.2. *mFISH protocol*

Preparation of slides for mFISH-PCC (Calyculin A) adherent cell cultures (e.g. MCF10A)

1) Prepare stock of Calyculin A (e.g. Sigma-Aldrich C5552; M = 1009,17 g/mol) – dissolve the content of the purchased vial (10 µg) in 100 µl pure ethanol (→ 100 µg/ml; 0,1 mM)
   - Work in laminar hood, but without the ventilation (not to evaporate the ethanol)
2) Add 2 µl of Calyculin A solution to 4 ml of medium (aspirate all the medium and return just 4 ml; final concentration = 0,05 µg/ml; ~50 nM) around 30 minutes before cell harvest – again, without ventilation in laminar hood
3) Prepare fresh Carnoy's solution (methanol:glacial acetic acid - 3:1) and place it on ice (~ 20 ml per sample, if stored in the freezer afterwards)
4) Prewarm the hypotonic KCl solution (0,075 M) in waterbath at 37°C (~ 8 ml per sample)
5) Harvest the cells as usual (keep the trypsin volume and time to minimum, cell will detach easily), BUT transfer all the media and PBS used for washing into the falcon tube (together with cells)
6) Centrifuge at 1750 RPM (~ 300 g) for 8 min
7) Discard the supernatant
8) Add 1-2 ml of prewarmed (37°C) KCl solution (0,075 M) and break gently the pellet with a plastic Pasteur pipette, start the timer set to 25 min
9) Add additional 6 ml of hypotonic solution and put tubes into water bath at 37°C for the rest of the 25 min
10) Add 1 ml of ice-cold fixative solution and put the tubes on ice for 10 min
11) Centrifuge at 2000 RPM for 5min
12) Discard the supernatant
13) Add 1-2 ml of Carnoy's solution and break the pellet very well with Pasteur pipette
14) Add additional 8 ml of Carnoy's solution and put the tubes on ice for at least 30 min
15) Centrifuge at 2000 RPM for 5 min
16) Discard the supernatant
17) Add 1-2 ml of fixative, depending on the number of cells (i.e., the size of the pellet), and break the pellet with Pasteur pipette
18) Drop the cell suspension on prewarmed (~ 40-42 °C) and clean^{X} microscopic slide – shake the water off first – (held approximately under 45° angle) from some height (15 – 20 cm) – 1-2 drops are sufficient
19) Let it air dry vertically for couple of hours (after, it can be used for the next procedures, e.g. mFISH hybridization (after 24 h aging at 37°C in HYBrite, etc.)

20) Not used cells - add at least 5 ml of Carnoy's solution to the cell suspension
21) Centrifuge at 2000 RPM for 5 min
22) Store the tubes in the freezer (cells in the form of pellet)

Hybridization protocol (cell line: MCF-10A)

1) After the slide preparation (fixation with 3:1 methanol/glacial acetic acid mixture), let slides air dry for couple of hours and then age them at 37 °C (e.g. in HYBrite) for about 24 h
2) Start the ice machine
3) Turn on the water bath set to 70 °C and place a Coplin jar with 2x SSC into it
4) Place Coplin jars with 0.1x and 2x SSC into the fridge

<u>Slide denaturation (and probe denaturation):</u>

5) Place slides into 2x SSC prewarmed to 70 °C and incubate for 30 min

   a. After about 5 min "shake" the slides inside of the Coplin to get rid of the air bubbles on them
   b. Take the probes out of the freezer and keep them in dark at room temperature for cca 20 min
   c. Aliquot the needed amount of probes (e.g. 10 µl for 24x24 or 14 µl for 24x32 mm cover slip)
6) Remove the Coplin jar from water bath and let to cool down to room temperature (about 40 min)
   a. Set the water bath to 75 °C and turn on other water bath set to 37 °C
   b. Prepare the Ethanol series (70, 95, and 100 %)
   c. About 5 min before the end of cool down, start the probe denaturation
      I. Incubate the probes at 75 °C for 5 min
      II. Put on ice briefly (30 s – 1 min) while moving to 37 °C water bath
      III. Incubate at 37 °C for 30 min
7) Before each transfer of the slides – shake well off the previous solution/liquid
8) Place slides into 0.1x SSC at room temperature for 1 min
9) Place slides into 0.07 M NaOH at room temperature for 1 min
10) Place slides into 0.1x SSC at 4 °C for 1 min (keep the Coplin jar with samples in fridge)
11) Place slides into 2x SSC at 4 °C for 1 min (keep the Coplin jar with samples in fridge)
12) Place slides into 70 % EtOH at room temperature for 1 min
13) Place slides into 95 % EtOH at room temperature for 1 min
14) Place slides into 100 % EtOH at room temperature for 1 min
15) Let the slides air dry in vertical position for about 20 min

Slide hybridization:

16) Spin the probe cocktail briefly
17) Pipette denatured probes onto denatured slide (e.g. 10 µl for 24x24 or 14 µl for 24x32 mm cover slip)
18) Cover with appropriate cover slip and let the probes to spread for couple of seconds (~ 30 s)
19) Carefully push out the bubbles from underneath the cover slip
20) Seal the cover slip around the edges with rubber cement
21) Place the slides to humidified (paper with distilled water at the sides) HYBrite chamber and incubate at 37 °C for 48 hours

Posthybridization washing and counterstain:

22) About 30-40 min before start, turn on the waterbath set to 72 °C and place a Coplin jar with 0.4x SSC into it
23) Take the DAPI/antifade solution from the fridge and let it to warm up at room temperature in dark for cca 20 min
24) Carefully remove all the rubber cement and the cover slips
25) Place slides into 0.4x SSC prewarmed to 72 °C for 2 min
26) Place slides in 2x SSCT for 30 s, at room temperature
27) Wash the slides briefly in dH_2O to avoid crystal formation and let air dry for about 20 min
28) Spin the DAPI/antifade solution briefly
29) Pipette 17 µl of DAPI/antifade solution onto the slides and cover with 24x50 mm cover slip
30) Let the DAPI/antifade to spread for couple of seconds (~ 30 s)
31) Carefully push out the bubbles from underneath the cover slip
32) Let incubate for about 30 min at room temperature in dark
33) If the slides are not analyzed immediately store them at -20 °C (before using them again, let them rest at the room temperature for 20 – 30 min)

Karyotype reconstruction

1) Open acquired images
2) Region: select the area to be analyzed on DAPI staining
3) Register Color: improve overlapping of color channels
4) Enter Caryo Mode
5) Object threshold: choose the object threshold deleting background noise
6) Separate: separate near chromosomes from each other
7) Separate cluster: divide overlapping chromosomes from clusters
8) Open color labelling scheme
9) Select "False color Mode"
10) Magnify: do a magnification of the objects
11) Sort chromosomes in appropriate position
12) Annotate aberrations eventually using "Single color gallery" to visualize the intensity of each color channel

1.3. *Whole Chromosome Painting protocol*

Preparation of slides for Whole Chromosome Painting with Calyculin A is the same as for mFISH.

Cell line: MCF-10A

Slide denaturation and probe denaturation:

1) After the slide preparation (fixation with 3:1 methanol/glacial acetic acid mixture), let slides air dry for couple of hours and then age them at 37 °C (e.g. in HYBrite) for at least 48 h

Slide hybridization:

2) Spin the probe cocktail briefly (this consists of chromosome 1-labelling probe emitting in FITC and chromosome 2-labelling probe emitting in the orange channel)
3) Pipette denatured probes onto denatured slide (e.g. 10 µl for 24x24 or 14 µl for 24x32 mm cover slip)
4) Cover with appropriate cover slip and let the probes to spread for couple of seconds (~ 30 s)
5) Carefully push out the bubbles from underneath the cover slip
6) Seal the cover slip around the edges with rubber cement
7) Place the slides to humidified (paper with distilled water at the sides) HYBrite chamber and denature sample and probe simultaneously by heating slides on a hotplate at 72 °C for 3 min and then incubate at 37 °C for at least 4 h

Posthybridization washing and counterstain:

8) About 30-40 min before start, turn on the waterbath set to 72 °C and place a Coplin jar with 0.4x SSC into it
9) Take the DAPI/antifade solution from the fridge and let it to warm up at room temperature in dark for cca 20 min
10) Carefully remove all the rubber cement and the cover slips
11) Place slides into 0.4x SSC prewarmed to 72 °C for 2 min
12) Place slides in 2x SSCT for 30 s, at room temperature
13) Wash the slides briefly in dH_2O to avoid crystal formation and let air dry for about 20 min
14) Spin the DAPI/antifade solution briefly
15) Pipette 17 µl of DAPI/antifade solution onto the slides and cover with 24x50 mm cover slip
16) Let the DAPI/antifade to spread for couple of seconds (~ 30 s)

17) Carefully push out the bubbles from underneath the cover slip
18) Let incubate for about 30 min at room temperature in dark
19) If the slides are not analyzed immediately store them at -20 °C (before using them again, let them rest at the room temperature for 20 – 30 min)

1.4. *BPA preparation protocol*

^{10}BPA is a substance that is poorly soluble in water. To make it usable it is necessary that it is complexed with fructose: in this way a solution of f^{10}BPA is obtained, here always referred as BPA. The protocol provides for:

1) weigh ^{10}BPA and fructose powder by means of a precision balance;
2) mix the two powders and add the culture medium;
3) add NaOH 5 mol/L until a clear solution is obtained with a pH between 9.5 and 10;
4) bring the pH back to values around 7.4 using HCl 5 mol / L and keep stirring for about 10 minutes;
5) add culture medium to the desired final volume, considering how much solution enriched with BPA at 80 ppm is required.

2. Counting code

<u>This is only a part of the entire code.</u>

```
rgbImage = imcrop(originalImage,[15 24 263 245]);
parameter_WS = 1000;
parameter_pixel = 5;
% Extract color channels.
redChannel = rgbImage(:,:,1); % Red channel
greenChannel = rgbImage(:,:,2); % Green channel
blueChannel = rgbImage(:,:,3); % Blue channel
% Create an all black channel.
allBlack = zeros(size(rgbImage, 1), size(rgbImage, 2), 'uint8');
% Create color versions of the individual color channels.
just_red = cat(3, redChannel, allBlack, allBlack);
just_green = cat(3, allBlack, greenChannel, allBlack);
just_blue = cat(3, allBlack, allBlack, blueChannel);
% Recombine the individual color channels to create the original RGB image again.
recombinedRGBImage = cat(3, redChannel, greenChannel, blueChannel);
recombinedRGImage = cat(3,redChannel,greenChannel,allBlack);
T_red_sm = imboxfilt(redChannel,sm_index);
T_green_sm = imboxfilt(greenChannel,sm_index);
T_blue_sm = imboxfilt(blueChannel,sm_index);
soglia_intensita_red = max(T_red_sm(:))*perc_soglia_intensita;
soglia_intensita_green = max(T_green_sm(:))*perc_soglia_intensita;
if strcmp('Otsu_method',method) == 1 || strcmp('third',method) == 1
for i=1:size(T_red_sm,1)
   for j=1:size(T_red_sm,2)
    if T_red_sm(i,j) < soglia_intensita_red
      T_red_sm(i,j) = 0;

    end
    if T_green_sm(i,j) < soglia_intensita_green
     T_green_sm(i,j) = 0;
    end
```

```
   end
end
end
   se = strel('disk',disk_radius);
   %% RED
   T_red_TH = imtophat(T_red_sm,se);
   T_red_adj = imadjust(T_red_sm);
   T_red_HM = imhmax(T_red_sm,soglia_intensita_red);
   T_red_HM2 = imhmax(T_red_adj,soglia_intensita_red);
   BW_red = imbinarize(T_red_adj);
   bw2_red = bwareaopen(BW_red,parameter_pixel);
   D1_red = -bwdist(~bw2_red);
   mask_red = imextendedmin(D1_red,parameter_WS); %2nd parameter is important
   D2_red = imimposemin(D1_red,mask_red);
   Ld2_red = watershed(D2_red);
   bw3_red = bw2_red;
   bw3_red(Ld2_red == 0) = 0;
   BN_WS_red = bw3_red;
   %% GREEN
   T_green_TH = imtophat(T_green_sm,se);
   T_green_adj = imadjust(T_green_sm);
   T_green_HM = imhmax(T_green_sm,soglia_intensita_green);
   T_green_HM2 = imhmax(T_green_TH,soglia_intensita_green);
   BW_green = imbinarize(T_green_adj);
   bw2_green = bwareaopen(BW_green,parameter_pixel);
   D1_green = -bwdist(~bw2_green);
   mask_green = imextendedmin(D1_green,parameter_WS); %2nd parameter is important
   D2_green = imimposemin(D1_green,mask_green);
   Ld2_green = watershed(D2_green);
   bw3_green = bw2_green;
   bw3_green(Ld2_green == 0) = 0;
   BN_WS_green = bw3_green;
   %% BLUE
   T_blue_ts = adaptthresh(T_blue_sm,1);
soglia_intensita_blue = max(T_blue_sm(:))*perc_soglia_intensita_blue;
for i=1:size(T_blue_sm,1)
   for j=1:size(T_blue_sm,2)
    if T_blue_sm(i,j) < soglia_intensita_blue
      T_blue_sm(i,j) = 0;
    end
   end
end

BW_blue = imbinarize(T_blue_sm,T_blue_ts);
BW_blue = imfill(BW_blue,'holes');
bw2_blue = bwareaopen(BW_blue,parameter_pixel);
D1_blue = -bwdist(~bw2_blue);
mask_blue = imextendedmin(D1_blue,parameter_WS_blue); %2nd parameter is important
D2_blue = imimposemin(D1_blue,mask_blue);
Ld2_blue = watershed(D2_blue);
bw3_blue = bw2_blue;
bw3_blue(Ld2_blue == 0) = 0;
BW_blue = bw3_blue;
nuc_mask = bwareafilt(BW_blue,1);
nuc_data = bwconncomp(BW_blue);
nuc_area =  regionprops('table',nuc_data,'Area'); %% this line is used to count the size of the nucleus area
nuc_mask = BW_blue.*nuc_mask;
nuc_Edge = edge(nuc_mask);
nuc_data = bwconncomp(nuc_mask);
nuc_area =  regionprops('table',nuc_data,'Area'); %% this line is used to count the size of the nucleus area
```

```
%% Colocalized FOCI
BW_red = imclearborder(BN_WS_red,8);
BW_green = imclearborder(BN_WS_green,8);
BW_red_mask = BW_red.*nuc_mask;
BW_green_mask = BW_green.*nuc_mask;
BW_redXgreen = BW_red_mask.*BW_green_mask;
%% Measure RED+GREEN
BW_data_comb = bwconncomp(BW_redXgreen);
BW_area_comb =  regionprops('table',BW_data_comb,'Area'); %% this line is used to count the foci and
their area
Foci_comb_0Gy30min_setI(1,k) = BW_data_comb.NumObjects;
if length(nuc_area.Area) > 1
nuc_Area_comb_0Gy30min_setI(1,k) = max(nuc_area.Area);
else
nuc_Area_comb_0Gy30min_setI(1,k) = nuc_area.Area;
end
if BW_data_comb.NumObjects < 1
Total_Area_comb_0Gy30min_setI(1,k) = 0;
Mean_Area_comb_0Gy30min_setI(1,k) = 0;
Perc_Area_comb_0Gy30min_setI(1,k) = 0;
else
Total_Area_comb_0Gy30min_setI(1,k) = sum(BW_area_comb.Area);
Mean_Area_comb_0Gy30min_setI(1,k) =
Total_Area_comb_0Gy30min_setI(1,k)/Foci_comb_0Gy30min_setI(1,k);
Perc_Area_comb_0Gy30min_setI(1,k) =
(Total_Area_comb_0Gy30min_setI(1,k)/nuc_Area_comb_0Gy30min_setI(1,k))*100;
end
if BW_data_comb.NumObjects > 0
kk_comb = BW_data_comb.NumObjects;
for i_comb=1:kk_comb
 Sample_full_comb_0Gy30min_setI(1,index_comb_0Gy30min_setI+i_comb) = k;
if length(nuc_area.Area) > 1
 nuc_full_Area_comb_0Gy30min_setI(1,index_comb_0Gy30min_setI+i_comb) = max(nuc_area.Area);
 else
 nuc_full_Area_comb_0Gy30min_setI(1,index_comb_0Gy30min_setI+i_comb) = nuc_area.Area;
 end
Foci_Area_comb_0Gy30min_setI(1,index_comb_0Gy30min_setI+i_comb) =
BW_area_comb.Area(i_comb);
 Perc_Area_full_comb_0Gy30min_setI(1,index_comb_0Gy30min_setI+i_comb) =
(BW_area_comb.Area(i_comb)/nuc_full_Area_comb_0Gy30min_setI(1,index_comb_0Gy30min_setI+i_c
omb))*100;
end
index_comb_0Gy30min_setI = index_comb_0Gy30min_setI+kk_comb;
end
%% DATI RED+GREEN 1
dati_comb_0Gy30min_setI =
table(Sample_comb_0Gy30min_setI',Foci_comb_0Gy30min_setI',nuc_Area_comb_0Gy30min_setI',Total
_Area_comb_0Gy30min_setI',Mean_Area_comb_0Gy30min_setI',Perc_Area_comb_0Gy30min_setI');
dati_comb_0Gy30min_setI.Properties.VariableNames = {'Image' 'Foci' 'Nuc_Area' 'Total_Area'
'Mean_Area' 'Perc_Area'};
index_area_comb_0Gy30min_setI = dati_comb_0Gy30min_setI.Foci>0;
% with = cells with foci
dati_with_comb_0Gy30min_setI =
table(Sample_comb_0Gy30min_setI(index_area_comb_0Gy30min_setI)',Foci_comb_0Gy30min_setI(ind
ex_area_comb_0Gy30min_setI)',nuc_Area_comb_0Gy30min_setI(index_area_comb_0Gy30min_setI)',
Total_Area_comb_0Gy30min_setI(index_area_comb_0Gy30min_setI)',Mean_Area_comb_0Gy30min_se
tI(index_area_comb_0Gy30min_setI)',Perc_Area_comb_0Gy30min_setI(index_area_comb_0Gy30min_s
etI)');
dati_with_comb_0Gy30min_setI.Properties.VariableNames = {'Image' 'Foci' 'Nuc_Area' 'Total_Area'
'Mean_Area' 'Perc_Area'};
```

```
if strcmp('Otsu_method',method) == 1
   writetable(dati_comb_0Gy30min_setI,'dati_comb_0Gy30min_setI_Otsu_method.txt');
elseif strcmp('disk_method',method) == 1
   writetable(dati_comb_0Gy30min_setI,'dati_comb_0Gy30min_setI_disk_method.txt');
elseif strcmp('third',method) == 1
   writetable(dati_comb_0Gy30min_setI,'dati_comb_0Gy30min_setI_third_method.txt');
end
%% DATI RED+GREEN 2
dati_full_comb_0Gy30min_setI =
table(Sample_full_comb_0Gy30min_setI(1,1:index_comb_0Gy30min_setI)',nuc_full_Area_comb_0Gy30
min_setI(1,1:index_comb_0Gy30min_setI)',Foci_Area_comb_0Gy30min_setI(1,1:index_comb_0Gy30min
_setI)',Perc_Area_full_comb_0Gy30min_setI(1,1:index_comb_0Gy30min_setI)');
dati_full_comb_0Gy30min_setI.Properties.VariableNames = {'Image' 'Nuc_Area' 'Foci_Area' 'Perc_Area'};
if strcmp('Otsu_method',method) == 1
   writetable(dati_full_comb_0Gy30min_setI,'dati_full_comb_0Gy30min_setI_Otsu_method.txt');
elseif strcmp('disk_method',method) == 1
   writetable(dati_full_comb_0Gy30min_setI,'dati_full_comb_0Gy30min_setI_disk_method.txt');
elseif strcmp('third',method) == 1
   writetable(dati_full_comb_0Gy30min_setI,'dati_full_comb_0Gy30min_setI_third_method.txt');
end
```

3. Table of experimental results

Foci assay results: weighted average between the two experiments

Colocalized foci BNCT

Sample	***Avg_foci***	***σ_foci***	***Avg_area (pixels)***	***σ_area***
0 Gy 0.5h	4.7	0.2	18	1
0.5 Gy 0.5h	9.2	0.5	15	1
2 Gy 0.5h	2.7	0.1	11	1
0 Gy 2h	3.5	0.2	21	2
0.5 Gy 2h	9.1	0.5	15.3	0.9
2 Gy 2h	8.9	0.6	12.3	0.8
0 Gy 3h	5.4	0.2	19	1
0.5 Gy 3h	15.1	0.8	18	1
2 Gy 3h	11.2	0.6	12	1
0 Gy 5h	1.56	0.08	15	2
0.5 Gy 5h	17	1	20	1
2 Gy 5h	20	2	15	1
0 Gy 24 h	1.81	0.08	23	2
0.5 Gy 24 h	19	1	24	1
2 Gy 24 h	26.2	0.7	21	1

γH2AX foci BNCT

Sample	***Avg_foci***	***σ_foci***	***Avg_area (pixels)***	***σ_foci***
0 Gy 0.5h	25.3	0.7	25	1
0.5 Gy 0.5h	27	2	32	2
2 Gy 0.5h	31	2	27	1
0 Gy 2h	13.0	0.9	23	2
0.5 Gy 2h	21	1	27	2
2 Gy 2h	43	3	29	2
0 Gy 3h	16.5	0.8	26	1
0.5 Gy 3h	32	2	30	2
2 Gy 3h	42	2	30	2
0 Gy 5h	8.9	0.7	21	2
0.5 Gy 5h	33	2	30	2
2 Gy 5h	48	4	27	2
0 Gy 24 h	7.9	0.5	24	2
0.5 Gy 24 h	27	2	34	2
2 Gy 24 h	43	3	31	2

53BP1 foci BNCT

Sample	***Avg_foci***	***σ_foci***	***Avg_area (pixels)***	***σ_foci***
0 Gy 0.5h	9.1	0.7	27	1
0.5 Gy 0.5h	16	1	26	2
2 Gy 0.5h	10.2	0.6	24	1
0 Gy 2h	7.4	0.5	27	2
0.5 Gy 2h	17	1	25	1
2 Gy 2h	20	1	24	2
0 Gy 3h	8.9	0.6	30	1
0.5 Gy 3h	21	1	30	2
2 Gy 3h	25	1	24	1
0 Gy 5h	7.7	0.6	23	2
0.5 Gy 5h	22	2	31	2
2 Gy 5h	33	3	25	2
0 Gy 24 h	3.6	0.2	32	2
0.5 Gy 24 h	23	1	35	2
2 Gy 24 h	31	2	31	2

Colocalized foci X-rays

Sample	***Avg_foci***	***σ_foci***	***Avg_area (pixels)***	***σ_foci***
0 Gy XR 0.5h	3.2	0.2	18	1
0.5 Gy XR 0.5h	9.1	0.6	19	1
2 Gy XR 0.5h	19	1	18	1
0 Gy XR 24 h	1.37	0.05	22	2
0.5 Gy XR 24 h	1.42	0.05	25	2
2 Gy XR 24 h	1.5	0.2	32	3

mFISH results

Sample	*Total aberrations frequency*	*σ*
0Gy BNCT	0.06	0.02
0.5Gy BNCT	2.0	0.1
2Gy BNCT	8.0	0.8
0Gy XR	0.09	0.03
0.5Gy XR	0.37	0.05
2Gy XR	0.79	0.04

Sample	*Complex aberrations frequency*	*σ*
0Gy BNCT	0	0
0.5Gy BNCT	0.25	0.04
2Gy BNCT	1.9	0.1
0Gy XR	0	0
0.5Gy XR	0.01	0.01
2Gy XR	0.08	0.03

Sample	*Ring aberrations frequency*	*σ*
0Gy BNCT	0	0
0.5Gy BNCT	0.02	0.01
2Gy BNCT	0.20	0.04
0Gy XR	0	0
0.5Gy XR	0	0
2Gy XR	0	0

Sample	*Frequency of chromosomes in complex per cell*	*σ*
0Gy BNCT	0	0
0.5Gy BNCT	0.66	0.05
2Gy BNCT	5.9	0.5
0Gy XR	0	0
0.5Gy XR	0.02	0.01
2Gy XR	0.19	0.04

Sample	*Frequency of breaks in complex per cell*	*σ*
0Gy BNCT	0	0
0.5Gy BNCT	0.84	0.04
2Gy BNCT	7.9	0.7
0Gy XR	0	0
0.5Gy XR	0.03	0.02
2Gy XR	0.24	0.04

Whole chromosome painting results

Sample	*Total aberrations frequency*	*σ*
0.5Gy BNCT	0.32	0.02
2Gy BNCT	1.87	0.08
0.5Gy XR	0.076	0.007
2Gy XR	0.25	0.02

Sample	*Complex aberrations frequency*	*σ*
0.5Gy BNCT	0.08	0.01
2Gy BNCT	0.75	0.03
0.5Gy XR	0.01	0.01
2Gy XR	0.01	0.01

Bibliography

[1] W. H. Jin et al., 'A Review of Boron Neutron Capture Therapy: Its History and Current Challenges', *Int J Part Ther*, vol. 9, no. 1, p. 82, Jun. 2022 [Online]. Available: 10.14338/ijpt-22-00002.1.

[2] S. Wang et al., 'Boron Neutron Capture Therapy: Current Status and Challenges', *Frontiers in Oncology*, vol. 12. Frontiers Media S.A., Mar. 31, 2022 [Online]. Available: 10.3389/fonc.2022.788770.

[3] W. A. G. Sauerwein et al., *Neutron capture therapy: Principles and applications*, vol. 9783642313349. Springer-Verlag Berlin Heidelberg, 2012 [Online]. Available: 10.1007/978-3-642-31334-9.

[4] J. A. Coderre et al., 'Boron Neutron Capture Therapy: Cellular Targeting of High Linear Energy Transfer Radiation', *Technol Cancer Res Treat*, vol. 2, no. 5, Oct. 2003[Online]. Availablewww.tcrt.org.

[5] Claretta Guidi, 'Master thesis in Physics: Irradiation of reconstructed human skin cultivated in-vitro: computational dosimetry and preliminary radiobiological evaluations for BNCT studies', University of Pavia, Pavia, 2018.

[6] P. G. Kruger, 'Some Biological Effects of Nuclear Disintegration Products on Neoplastic Tissue.', *Proc Natl Acad Sci U S A*, vol. 26, no. 3, pp. 181–92, Mar. 1940[Online]. Availablehttp://www.ncbi.nlm.nih.gov/pubmed/16588335.

[7] A. Monti Hughes, 'Importance of radiobiological studies for the advancement of boron neutron capture therapy (BNCT)', *Expert reviews in molecular medicine*, vol. 24. NLM (Medline), p. e14, Mar. 31, 2022 [Online]. Available: 10.1017/erm.2022.7.

[8] V. A. Trivillin et al., 'Translational boron neutron capture therapy (BNCT) studies for the treatment of tumors in lung', *Int J Radiat Biol*, vol. 95, no. 5, pp. 646–654, May 2019 [Online]. Available: 10.1080/09553002.2019.1564080.

[9] TAE Life Science, 'Developing targeted drugs for boron neutron'[Online]. Availablewww.taelifesciences.com[Accessed: 12June2023].

[10] J. A. Nickoloff et al., 'Clustered DNA double-strand breaks: Biological effects and relevance to cancer radiotherapy', *Genes*, vol. 11, no. 1. MDPI AG, Jan. 01, 2020 [Online]. Available: 10.3390/genes11010099.

[11] E. J. Hall and A. J. Giaccia, *Radiobiology for the Radiologist. Lippincott Williams & Wilkins*. 2006 [Online]. Available: https://doi.org/10.1007/s00259-007-0383-8.

[12] Z. Nikitaki et al., 'Key biological mechanisms involved in high-LET radiation therapies with a focus on DNA damage and repair', *Expert Reviews in Molecular Medicine*, vol. 24. Cambridge University Press, Mar. 31, 2022 [Online]. Available: 10.1017/erm.2022.6.

[13] J. M. Danforth et al., 'Chromatin and the Cellular Response to Particle Radiation-Induced Oxidative and Clustered DNA Damage', *Frontiers in Cell and Developmental Biology*, vol. 10. Frontiers Media S.A., Jul. 13, 2022 [Online]. Available: 10.3389/fcell.2022.910440.

[14] D. A. Gewirtz et al., *Apoptosis, Senescence, and Cancer*, vol. 1. 2007.

[15] V. Mladenova et al., 'DNA Damage Clustering after Ionizing Radiation and Consequences in the Processing of Chromatin Breaks', *Molecules*, vol. 27, no. 5. MDPI, Mar. 01, 2022 [Online]. Available: 10.3390/molecules27051540.

[16] R. Scully et al., 'DNA double-strand break repair-pathway choice in somatic mammalian cells', *Nature Reviews Molecular Cell Biology*, vol. 20, no. 11. Nature Publishing Group, pp. 698–714, Nov. 01, 2019 [Online]. Available: 10.1038/s41580-019-0152-0.

[17] C.-Y. Huang et al., 'Boron Neutron Capture Therapy Eliminates Radioresistant Liver Cancer Cells by Targeting DNA Damage and Repair Responses', *J Hepatocell Carcinoma*, vol. Volume 9, pp. 1385–1401, Dec. 2022 [Online]. Available: 10.2147/jhc.s383959.

[18] Sridharan DM et al., 'Understanding cancer development processes after HZE-particle exposure: roles of ROS, DNA damage repair and inflammation.', *Radiation Research* , vol. 183, no. 1–26, 2015 [Online]. Available: https://doi.org/10.1667/RR13804.1.

[19] Z. Nikitaki et al., 'Measurement of complex DNA damage induction and repair in human cellular systems after exposure to ionizing radiations of varying linear energy transfer (LET)', *Free Radic Res*, vol. 50, pp. S64–S78, Nov. 2016 [Online]. Available: 10.1080/10715762.2016.1232484.

[20] J. A. Nickoloff et al., 'Clustered DNA double-strand breaks: Biological effects and relevance to cancer radiotherapy', *Genes*, vol. 11, no. 1. MDPI AG, Jan. 01, 2020 [Online]. Available: 10.3390/genes11010099.

[21] K. Maliszewska-Olejniczak et al., 'Molecular Mechanisms of Specific Cellular DNA Damage Response and Repair Induced by the Mixed Radiation Field During Boron Neutron Capture Therapy', *Front Oncol*, vol. 11, May 2021 [Online]. Available: 10.3389/fonc.2021.676575.

[22] F. Zhang and Z. Gong, 'Regulation of DNA double-strand break repair pathway choice: a new focus on 53BP1', *Journal of Zhejiang University: Science B*, vol. 22, no. 1. Zhejiang University Press, pp. 38–46, Jan. 01, 2021 [Online]. Available: 10.1631/jzus.B2000306.

[23] J. Moquet et al., 'Gamma-H2AX biodosimetry for use in large scale radiation incidents: Comparison of a rapid "96 well lyse/fix" protocol with a routine method', *PeerJ*, vol. 2014, no. 1, pp. 1–11, 2014 [Online]. Available: 10.7717/peerj.282.

[24] T. Groesser et al., 'Persistence of γH2AX and 53BP1 foci in proliferating and non-proliferating human mammary epithelial cells after exposure to γrays or iron ions'.

[25] N. Hamada et al., 'Histone H2AX Phosphorylation in Normal Human Cells Irradiated with Focused Ultrasoft X Rays: Evidence for Chromatin Movement during Repair', 2006[Online]. Availablehttps://www.jstor.org/stable/4098779?seq=1&cid=pdf-reference#references_tab_contents.

[26] I. Y. Belyaev, 'Radiation-induced DNA repair foci: Spatio-temporal aspects of formation, application for assessment of radiosensitivity and biological dosimetry', *Mutation Research - Reviews in Mutation Research*, vol. 704, no. 1–3. pp. 132–141, Apr. 2010 [Online]. Available: 10.1016/j.mrrev.2010.01.011.

[27] R. M. Anderson et al., 'M-FISH analysis shows that complex chromosome aberrations induced by-particle tracks are cumulative products of localized rearrangements'[Online]. Availablewww.pnas.orgcgidoi10.1073pnas.182426799.

[28] B. Alberts et al., 'The Molecular Biology of the Cell'[Online]. Availablehttp://www.geocities.com/zrnet76/.

[29] T. Miura and W. F. Blakely, 'Optimization of calyculin A-induced premature chromosome condensation assay for chromosome aberration studies', *Cytometry Part A*, vol. 79A, no. 12, pp. 1016–1022, Dec. 2011 [Online]. Available: 10.1002/cyto.a.21154.

[30] M. N. Cornforth, 'Analyzing Radiation-Induced Complex Chromosome Rearrangements by Combinatorial Painting', 2001 [Online]. Available: 10.1667/0033-7587(2001)155[0643:ariccr]2.0.co;2.

[31] V. Mladenova et al., 'The high toxicity of DSB-clusters modelling high-LET-DNA damage derives from inhibition of c-NHEJ and promotion of alt-EJ and SSA despite increases in HR', *Front Cell Dev Biol*, vol. 10, Oct. 2022 [Online]. Available: 10.3389/fcell.2022.1016951.

[32] G. Petringa et al., 'Radiobiological Outcomes, Microdosimetric Evaluations and Monte Carlo Predictions in Eye Proton Therapy', *Applied Sciences*, vol. 11, no. 19, p. 8822, Sep. 2021 [Online]. Available: 10.3390/app11198822.

[33] P. Andreo, 'Monte Carlo simulations in radiotherapy dosimetry', *Radiation Oncology*, vol. 13, no. 1, p. 121, Dec. 2018 [Online]. Available: 10.1186/s13014-018-1065-3.

[34] S. S. Incerti et al., ' The Geant4-DNA project', *Int. J. Model. Simul. Sci. Comput.*, vol. 1, pp. 157–178, 2010.

[35] *https://indico.cern.ch/event/775870/contributions/3228301/attachments/1824890/2986189/LGR-OMA2019_MC-FINAL_Shared.pdf*. .

[36] D. Sakata et al., 'Evaluation of early radiation DNA damage in a fractal cell nucleus model using Geant4-DNA', *Physica Medica*, vol. 62, pp. 152–157, Jun. 2019 [Online]. Available: 10.1016/j.ejmp.2019.04.010.

[37] S. Incerti et al., 'Geant4-DNA example applications for track structure simulations in liquid water: A report from the Geant4-DNA Project', *Med Phys*, vol. 45, no. 8, pp. e722–e739, Aug. 2018 [Online]. Available: 10.1002/mp.13048.

[38] W. Friedland and P. Kundrát, 'Track structure based modelling of chromosome aberrations after photon and alpha-particle irradiation', *Mutation Research/Genetic Toxicology and Environmental Mutagenesis*, vol. 756, no. 1–2, pp. 213–223, Aug. 2013 [Online]. Available: 10.1016/j.mrgentox.2013.06.013.

[39] V. N. Ivanchenko et al., 'Combination of electromagnetic physics processes for microdosimetry in liquid water with the Geant4 Monte Carlo simulation toolkit', *Nucl Instrum Methods Phys Res B*, vol. 273, pp. 95–97, 212AD [Online]. Available: https://doi.org/10.1016/j.nimb.2011.07.048.

[40] I. Kyriakou et al., 'Review of the geant4-dna simulation toolkit for radiobiological applications at the cellular and dna level', *Cancers (Basel)*, vol. 14, no. 1, Jan. 2022 [Online]. Available: 10.3390/cancers14010035.

[41] S. Incerti et al., 'The Geant4-DNA project The Geant4-DNA collaboration'.

[42] 'http://geant4-dna.in2p3.fr/styled-5/index.html'.

[43] *http://geant4-dna.in2p3.fr/styled-5/index.html*. .

[44] K. P. Chatzipapas et al., 'Ionizing Radiation and Complex DNA Damage: Quantifying the Radiobiological Damage Using Monte Carlo Simulations', *Cancers (Basel)*, vol. 12, no. 4, p. 799, Mar. 2020 [Online]. Available: 10.3390/cancers12040799.

[45] S. Incerti et al., 'Comparison of <scp>GEANT4</scp> very low energy cross section models with experimental data in water', *Med Phys*, vol. 37, no. 9, pp. 4692–4708, Aug. 2010 [Online]. Available: 10.1118/1.3476457.

[46] Z. Francis et al., 'Simulation of DNA damage clustering after proton irradiation using an adapted DBSCAN algorithm', *Comput Methods Programs Biomed*, vol. 101, no. 3, pp. 265–270, Mar. 2011 [Online]. Available: 10.1016/j.cmpb.2010.12.012.

[47] P. Bláha et al., 'The Proton-Boron Reaction Increases the Radiobiological Effectiveness of Clinical Low- and High-Energy Proton Beams: Novel Experimental Evidence and Perspectives', *Front Oncol*, vol. 11, Jun. 2021 [Online]. Available: 10.3389/fonc.2021.682647.

[48] Debnath J et al., ' Morphogenesis and oncogenesis of MCF-10A mammary epithelial acini grown in three-dimensional basement membrane cultures. ', *Methods*, vol. 30, no. 3, pp. 256–268, Jul. 2003 [Online]. Available: 10.1016/s1046-2023(03)00032-x.

[49] C. Ferrari et al., 'In vitro and in vivo studies of boron neutron capture therapy: Boron uptake/washout and cell death', *Radiat Res*, vol. 175, no. 4, pp. 452–462, Apr. 2011 [Online]. Available: 10.1667/RR2156.1.

[50] I. Postuma et al., 'An improved neutron autoradiography set-up for 10B concentration measurements in biological samples', *Reports of Practical Oncology and Radiotherapy*, vol. 21, no. 2, pp. 123–128, Mar. 2016 [Online]. Available: 10.1016/j.rpor.2015.10.006.

[51] A. Geltmeier et al., 'Characterization of Dynamic Behaviour of MCF7 and MCF10A Cells in Ultrasonic Field Using Modal and Harmonic Analyses', *PLoS One*, vol. 10, no. 8, p. e0134999, Aug. 2015 [Online]. Available: 10.1371/journal.pone.0134999.

[52] A. M. D. Viegas et al., 'Detailed dosimetry calculation for in-vitro experiments and its impact on clinical BNCT', *Physica Medica*, vol. 89, pp. 282–292, Sep. 2021 [Online]. Available: 10.1016/j.ejmp.2021.08.010.

[53] M. Durante et al., 'Single-charged particle damage to living cells: a new method to detect traversals based on track-etch detectors.', *Nucl. Instr. Meth. B*, vol. 94, no. 1, pp. 251–258, 1994 [Online]. Available: https://doi.org/10.1016/0168-583X(94)95363-5.

[54] R. Anderson, 'Multiplex fluorescence in situ hybridization (M-FISH).', *Methods Mol Biol*, vol. 659, pp. 83–97, 2010 [Online]. Available: 10.1007/978-1-60761-789-1_6.

[55] *https://metasystems-probes.com/en/probes/mfish/d-0125-060-di/*. .

[56] A. Geltmeier et al., 'Characterization of Dynamic Behaviour of MCF7 and MCF10A Cells in Ultrasonic Field Using Modal and Harmonic Analyses', *PLoS One*, vol. 10, no. 8, p. e0134999, Aug. 2015 [Online]. Available: 10.1371/journal.pone.0134999.

[57] S. Bortolussi et al., 'Neutron flux and gamma dose measurement in the BNCT irradiation facility at the TRIGA reactor of the University of Pavia', *Nucl Instrum Methods Phys Res B*, vol. 414, pp. 113–120, Jan. 2018 [Online]. Available: 10.1016/j.nimb.2017.10.023.

[58] E. Bobkova et al., 'Recruitment of 53BP1 proteins for DNA repair and persistence of repair clusters differ for cell types as detected by single molecule localization microscopy', *Int J Mol Sci*, vol. 19, no. 12, Dec. 2018 [Online]. Available: 10.3390/ijms19123713.

[59] G. V. Mechetin and D. O. Zharkov, 'DNA Damage Response and Repair in Boron Neutron Capture Therapy', *Genes*, vol. 14, no. 1. MDPI, Jan. 01, 2023 [Online]. Available: 10.3390/genes14010127.

[60] S. J. Roobol et al., 'Comparison of high-and low-let radiation-induced dna double-strand break processing in living cells', *Int J Mol Sci*, vol. 21, no. 18, pp. 1–19, Sep. 2020 [Online]. Available: 10.3390/ijms21186602.

[61] L. Jezkova et al., 'Particles with similar LET values generate DNA breaks of different complexity and reparability: A high-resolution microscopy analysis of γh2AX/53BP1 foci',

Nanoscale, vol. 10, no. 3, pp. 1162–1179, Jan. 2018 [Online]. Available: 10.1039/c7nr06829h.

[62] T. Yasuhara and L. Zou, 'Impacts of chromatin dynamics and compartmentalization on DNA repair', *DNA repair*, vol. 105. NLM (Medline), p. 103162, Sep. 01, 2021 [Online]. Available: 10.1016/j.dnarep.2021.103162.

[63] K. E. van Holde, *Chromatin*. New York, NY: Springer New York, 1989 [Online]. Available: 10.1007/978-1-4612-3490-6.

[64] J. R. K. Savage and P. J. Simpson, 'FISH "painting" patterns resulting from complex exchanges ', *Mutation Research*, vol. 474, pp. 139–146, 2001 [Online]. Available: https://doi.org/10.1016/0165-1161(94)90008-6.

[65] T. E. Schmid et al., 'The effectiveness of the high-LET radiations from the boron neutron capture [10B(n,α)7Li] reaction determined for induction of chromosome aberrations and apoptosis in lymphocytes of human blood samples', *Radiat Environ Biophys*, vol. 54, no. 1, pp. 91–102, Mar. 2015 [Online]. Available: 10.1007/s00411-014-0577-y.

[66] L. Manti et al., 'Measurements of metaphase and interphase chromosome aberrations transmitted through early cell replication rounds in human lymphocytes exposed to low-LET protons and high-LET 12C ions.', *Mutat Res*, vol. 596, no. 1–2, pp. 151–65, Apr. 2006 [Online]. Available: 10.1016/j.mrfmmm.2005.12.010.

[67] K. P. Chatzipapas et al., 'Ionizing Radiation and Complex DNA Damage: Quantifying the Radiobiological Damage Using Monte Carlo Simulations', *Cancers (Basel)*, vol. 12, no. 4, p. 799, Mar. 2020 [Online]. Available: 10.3390/cancers12040799.

[68] *https://www.javatpoint.com/density-based-clustering-in-data-mining*. .

Ringraziamenti